


國立交通大學

機械工程學系

博士論文

以脈衝式電源驅動的軸對稱均勻氙氣電漿產生真空紫外光輻射之數值模擬研究



**Numerical Investigation of VUV Emission
from a Homogeneous Coaxial Xenon
Excimer Discharge Driven by Distorted
Bipolar Square Voltages**

研究生：周欣芸

指導教授：吳宗信 博士

西元 2011 年 1 月

以脈衝式電源驅動的軸對稱均勻氙氣電漿產生
真空紫外光輻射之數值模擬研究

Numerical Investigation of VUV Emission from a
Homogeneous Coaxial Xenon Excimer Discharge Driven
by Distorted Bipolar Square Voltages

研究生：周欣芸

Student：Shin-Yun Jou

指導教授：吳宗信

Advisor：Dr. Jong-Shinn Wu



Submitted to Department of Mechanical Engineering College of Engineering
National Chiao Tung University
in partial Fulfillment of the Requirements
for the Degree of Doctor of Philosophy
in
Mechanical Engineering
2011
Hsinchu, Taiwan

西元 2011 年 1 月

以脈衝式電源的軸對稱均勻氬氣電漿產生真空紫外光輻射之數值模

擬研究

學生：周欣芸

指導教授：吳宗信 博士

國立交通大學機械工程學系博士班

中文摘要

近年來，準分子紫外光(Excimer UV; EUV)燈管放光技術在工業方面有著廣泛的應用，例如臭氧的生成及半導體矽晶圓的表面清潔等。準分子的產生是透過電漿內部複雜的化學反應機制例如解離、激發等碰撞過程，而真空紫外光的發生則是在準分子由受激態掉回基態時所釋放出的能量所致。由於此類電漿反應機制相當複雜，以致於燈管的設計通常靠試誤法，需付出高額的時間及成本。因此本論文的主要目的是藉由流體模式模擬工具了解 EUV 燈管的氣體放電機制。如此，在使用不同的參數時，我們可以先預測難以在實驗下量測到的電漿特性。這樣不但可以縮短 EUV 燈管的設計時程而且可能得到更好的燈管設計。

本論文使用一維軸對稱流體模式進行 kHz 等級電源驅動的氬氣準分子燈管電漿模擬。此程式以有限差分法進行數值離散，考慮 local mean energy approximation (LMEA)及簡化氬氣化學反應機制。由於電子質量很輕，可立即反應電場變化，以電子在一個週期內隨時間的變化量可分為三個主要階段：pre-breakdown(前放電區)、breakdown(放電區；172 nm 真空紫外光放光最強烈階段)及 post-breakdown(後放電區)階段。結果顯示真空紫外光放射效率在使用 distorted bipolar 方形波形的表現比使用正弦波波形為佳。主要歸因於以下兩種主要的機制：第一、在 distorted bipolar 方形波形下外加電壓迅速抬升，電子在沒有彈性碰撞損失下可以吸收更多能量進行解離、激發等碰撞反應產生更高濃度的激發態原子進而增加 172 nm 紫外光所放出的量。第二、在正弦波形下，外加電壓的緩慢下降促進離子透過歐姆加熱方式吸收外加電場能量，而離子所吸收的能

量並不會用於解離、激發等碰撞反應，對整個放電系統而言是一種能量的浪費。

為了瞭解控制準分子紫外光燈放電的真空紫外光輻射效率，我們在 distorted bipolar 方形波形電源驅動下變化四種參數包括外加電壓頻率、背景氣體壓力、燈管的寬度及介電層的數量。結果顯示強烈的 172 nm 紫外光放射均在放電區前期發生，這與電子吸收能量的階段相當吻合；另外離子的能量吸收主要發生在放電區的後期。令人驚訝的是，當調高頻率時，燈管的效率只有些微的增加；而隨著燈管電極間寬度的增加，燈管的效率也大幅的增加。此外，172 nm 紫外光的放射效率在 600 torr 下有最大值。而只放置一個介電層的燈管效率的表現比兩端都放置介電層的燈管為佳。

最後，在本論文中也進行背景氣體的加熱影響的研究。加入氣體加熱影響的模擬結果可合理解釋電漿產生的真空紫外光輻射與背景氣體壓力的關連而在超過某各臨界壓力電漿無法被點燃的現象的實驗結果。這主要歸因於兩個主要機制，第一、在高壓 ($P = 510 \text{ torr}$) 下，由於氣體加熱引起背景氣體不均勻分佈導致離子轉換反應($2\text{Xe} + \text{Xe}^+ \rightarrow \text{Xe}_2^+$)更為活躍進而增進 Xe_2^+ 與電子的合併反應，最終使得電子數量無法維持電漿生成；第二、隨背景氣壓增加，電子彈性碰撞的能量損失亦隨著增加，造成整體電子能量(溫度)下降，進而使得電漿強度減弱，這反應機制在高氣壓下對電漿造成的影響更為顯著。

Numerical Investigation of VUV Emission from a Homogeneous Coaxial Xenon Excimer Discharge Driven by Distorted Bipolar Square Voltages

Student : Shin-Yun Jou

Advisor : Dr. Jong-Shinn Wu

Department of Mechanical Engineering
National Chiao Tung University

Abstract

Recently, the excimer UV (EUV) lamp has found a wide range of applications in industry, for example, in ozone generation and surface cleaning for Si wafer in semiconductor fabrication process. The generation of EUV results from the reaction mechanism like ionization or excitation and other collision processes in the plasma. The occurrence of VUV is due to the process that excimer falls from various excited states to a ground state. However, its design was mostly based on the trial-and-error method, which is time-consuming and cost ineffective. Thus, the goal of this thesis is to predict and understand the plasma physics and chemistry inside an homogeneous EUV discharge through fluid modeling technique.

In this thesis, a self-consistent radial one-dimensional fluid model, considering local mean energy approximation (LMEA), along with a set of simplified xenon plasma chemistry is employed to simulate the discharge physics and chemistry. The discharge is divided into three-period regions; these include: the pre-breakdown, the breakdown (most intense at 172 nm VUV emission) and the post-breakdown periods. The results show that the efficiency of VUV emission using the distorted bipolar square voltages is

much greater than that using sinusoidal voltages, which is attributed to two major mechanisms. The first is the much larger rate of change of the voltage in bipolar square voltages, in which only the electrons can efficiently absorb the power from the applied electric field in a very short period of time. Energetic electrons then generate a higher concentration of metastable (and also excited dimer) xenon that is distributed more uniformly across the gap, for a longer period of time during the breakdown process. The second is the comparably smaller amount of “wasted” power deposition by Xe_2^+ in the post-breakdown period, as driven by distorted bipolar square voltages, because of the nearly vanishing gap voltage caused by the shielding effect resulting from accumulated charges on both dielectric surfaces.

Emitted powers of EUV light and deposited powers to the charged species of a homogeneous coaxial xenon discharge driven by the distorted bipolar square voltages are simulated by varying the test conditions of four key parameters, which include the driving frequency, gas pressure, gap distance and number of dielectric layers. Results show that there are three distinct periods that include pre-breakdown, breakdown and post-breakdown ones. It is found that intensive EUV (172 nm) emission occurs during the early part of the breakdown period, which correlates very well in time with the power deposition through electrons. In addition, power deposition through Xe^+ and Xe_2^+ occurs mainly in the breakdown period and later part of breakdown period, respectively. Surprisingly, the emission efficiency of 172 nm increases only slightly with increasing driving frequency of power source, while it increases dramatically with increasing gap distance. In addition, the maximum emission efficiency is found

to take place at gas pressure of 600 torr. The emission efficiency of one-dielectric case is found to be better than that of two-dielectric one. The underlying mechanisms in the above observations are discussed in detail in the paper.

Finally, gas heating is included in the fluid modeling by a heat conduction equation for xenon. With this consideration, one can explain reasonably well the experimentally observed VUV emission at various background pressures, especially the extinguishment of the discharge as pressure exceeds some threshold value. The major mechanisms of the above phenomena are described as follows: 1) Increasing pressure leads to higher gas heating because of increasing electron energy loss through the elastic collision with xenon atoms in the bulk region; and 2) The above leads to higher gas density at outer region of the gap ($r \approx 1.1 \sim 1.16$ cm), because of heat conduction and assumed uniform pressure distribution, as compared to the case without gas heating which promotes the three-body Xe^+ -to- Xe_2^+ ion conversion and $e\text{-Xe}_2^+$ recombination that greatly reduces the plasma density as pressure exceeds some threshold.

Acknowledgements

首先，感謝我的論文指導教授吳宗信老師，無論是學業上的指導或是生活上的言教與身教都讓我獲益良多。

也感謝本次口試指導委員陳彥升博士、徐振哲助理教授、魏大欽副教授及劉耀先助理教授所提供的寶貴意見，因為你們的意見，使的本篇論文的內容更為充實。

再來，感謝研究室的電漿模擬團隊夥伴們，捷祭、孟樺、沅明、凱文、必任、昆模和穎志，沒有你們的幫助，就沒有這篇論文的產生，這也讓我體驗到團隊合作無間的精神。

而本篇論文的產生，須感謝工研院材化所的學研合作計畫，謝謝魏碧玉博士讓我們機會接觸到 Excimer UV 燈管的領域。沒有這合作計畫，就沒有本篇論文的產生。

更感謝我的家人與小國的一路相伴，尤其是父母親的支持，是我完成學業地一大助力。爸、媽，你女兒拿到學位了！

研究室的單車夥伴們，允民、哲維、凱文與沅明，與你們一起騎單車穿梭於新竹的鄉間山路及 17 公里海岸線那段時光真的很快樂，也為研究室的生活增添幾許色彩，謝謝你們給的美好回憶，也希望日後還有機會一起騎車。

這段旅程雖然漫長，但終究還是抵達終點，面對下一段旅程，我會以謙卑及踏實的心態，從容的面對。

Table of Contents

| | |
|-------------------------|-----|
| 中文摘要 | I |
| Abstract | III |
| Acknowledgements | VI |
| Table of Contents | VII |
| List of Tables | X |
| List of Figures | XI |
| Nomenclature | XV |

Chapter 1

| | |
|--|---|
| Introduction..... | 1 |
| 1.1 Background and Motivation | 1 |
| 1.1.1 History and Applications | 1 |
| 1.1.2 Dielectric Barrier Discharges..... | 2 |
| 1.1.3 Breakdown Mechanism | 3 |
| 1.1.4 Overview of Excimers..... | 4 |
| 1.2 Discharge Control | 5 |
| 1.3 Literature Survey | 6 |
| 1.3.1 Xenon Excimer Discharges Driven by the Sinusoidal Voltages | 6 |
| 1.3.3 Gas Heating in Gas Discharges..... | 7 |
| 1.4 Objectives and Organization of the Thesis..... | 8 |
| 1.4.1 Specific Objectives | 8 |
| 1.4.2 Organization of the Thesis | 9 |

Chapter 2

| | |
|--|----|
| Fluid Modeling..... | 11 |
| 2.1 Basic Equations of Fluid Modeling | 11 |
| 2.1.1 Continuity Equations..... | 11 |
| 2.1.2 Electron Energy Density Equation..... | 13 |
| 2.1.3 Field Equation | 14 |
| 2.1.4 General Boundary Conditions | 15 |
| 2.1.5 VUV Emission Efficiency | 16 |
| 2.1.6 Discharge Current, Dielectric Voltage and Gap Voltage..... | 17 |
| 2.2 Numerical Method and Algorithms..... | 17 |
| 2.2.1 Numerical Discretization..... | 17 |

| | |
|---|----|
| 2.2.2 Parallel Fully Implicit Newton-Krylov-Swartz-Algorithm..... | 18 |
|---|----|

Chapter 3

Validation of the Fluid Modeling in Xenon Discharge Simulation..... 19

| | |
|--|----|
| 3.1 Xenon Plasma Chemistry | 19 |
| 3.2 Case-1: 1-D Homogenous Planar Xenon discharge..... | 20 |
| 3.2.1 Simulation Conditions | 20 |
| 3.2.2 Results and Discussion..... | 20 |
| 3.3 Case-2: 1-D Homogenous Cylindrical Xenon discharge | 21 |
| 3.3.1 Simulation Condition..... | 21 |
| 3.3.2 Results and Discussion..... | 21 |
| 3.4 Brief Summary of This Chapter..... | 22 |

Chapter 4

Enhancement of VUV Emission from a Homogeneous Coaxial Xenon Excimer Ultraviolet Lamp Driven by Distorted Bipolar Square Voltages 24

| | |
|---|----|
| 4.1 Discharge Properties by Sinusoidal Voltages | 24 |
| 4.1.1 Phase Diagrams of Key Discharge Properties..... | 24 |
| 4.1.2 Temporal Variation of Discharge Properties..... | 28 |
| 4.2 Discharge Properties by Bipolar Distorted Square Voltages | 30 |
| 4.2.2 Phase Diagrams of Key Discharge Properties..... | 31 |
| 4.2.3 Snapshots of Key Discharge Properties..... | 35 |
| 4.2.1 Temporal Variation of Discharge Properties..... | 39 |
| 4.3 General VUV Emission Power and Efficiency | 41 |
| 4.3.1 Characteristics of Power Deposition and VUV Emission..... | 41 |
| 4.3.2 Comparison of VUV Emission Efficiency between Sinusoidal and Distorted Bipolar Square Voltages..... | 42 |
| 4.4 Brief Summary of This Chapter..... | 45 |

Chapter 5

Parametric Study of VUV Emission from a Homogeneous Coaxial Xenon Excimer Ultraviolet Lamp Driven by Distorted Bipolar Square Voltages 47

| | |
|---|-----------|
| 5.1 Typical Characteristics of Power Deposition and VUV Emission | 47 |
| 5.2 Simulation Conditions | 52 |
| 5.3 Effect of Frequency Variation..... | 52 |
| 5.4 Effect of Background Gas Pressure Variation | 54 |
| 5.5 Effect of Gap Distance Variation..... | 56 |
| 5.6 Effect of Varying the Number of Dielectric Layers | 58 |
| 5.4 Brief Summary of This Chapter..... | 59 |

Chapter 6

Effect of Gas Heating on VUV Emission from a Homogeneous Coaxial Xenon Excimer Ultraviolet Lamp Driven by Distorted Bipolar Square Voltages

| | |
|---|-----------|
| 6.1 Heat Conduction Equation | 61 |
| 6.3 Results and Discussion..... | 63 |
| 6.4 Brief Summary of This Chapter..... | 68 |

Chapter 7

Conclusion and Recommendations of Future Work.....

| | |
|--|-----------|
| 7.1 Conclusion..... | 70 |
| 7.1.1 Enhancement of VUV Emission from a Coaxial Xenon Excimer Ultraviolet Lamp Driven by Distorted Bipolar Square Voltages | 70 |
| 7.1.2 A Parametric Study of VUV Emission from a Coaxial Xenon Excimer Ultraviolet Lamp Driven by Distorted Bipolar Square Voltages | 71 |
| 7.1.3 Effect of Gas Heating on VUV Emission from a Coaxial Xenon Excimer Ultraviolet Lamp Driven by Distorted Bipolar Square Voltages | 72 |

References.....

127

List of Tables

Table 3-1 Reaction channels of the xenon discharge 75

Table 4-1 Power transfer efficiency between sinusoidal and bipolar square voltages..... 76

Table 5-1 Test conditions for the parametric study..... 77



List of Figures

Figure 1-1 Common planar and cylindrical dielectric-barrier discharge configurations. [Kogelschatz *et al*, 1999]..... 78

Figure 1-2 Evolution of electron avalanche in discharge gap, showing avalanche development, avalanche-to-streamer transition, and streamer propagation. [Chirokov *et al*, 2005]...... 79

Figure 3-1 Reaction processes in a Xe discharge. 80

Figure 3-2 The comparison of simulated result with Beleznai *et al*. and ours. 81

Figure 3-3(a) A sketch of the coaxial xenon excimer lamp and (b) The configuration of the coaxial xenon excimer lamp. 82

Figure 3-4 The comparison with simulated result and experimental data. 83'

Figure 4-1 Spatiotemporal diagram of the number densities of charged species: electron (upper), atomic xenon ion (middle) and molecular xenon ion (bottom). 84

Figure 4-2 Spatiotemporal diagram of the number densities of excited species: Xe^* (met) (upper), $Xe_2^*(^3\Sigma_u^+)$ (middle) and electron temperature (bottom)..... 85

Figure 4-3 The temporal variations of (a) applied voltage (V_a), dielectric voltage (V_d), gap voltage (V_g), discharge current density at inner side ($r=0.8$ cm) and accumulated charge (Q_a) and (b) the number density of electron, the ion species Xe^+ and Xe_2^+ , the main excited species Xe^* (met), the main excimer species $Xe_2^*(^3\Sigma_u^+)$ and Te utilizing sinusoidal waveform over a cycle. 86

Figure 4-4 Spatiotemporal diagram of the number densities of charged species: electron (upper), atomic xenon ion (middle) and molecular xenon ion (bottom). 87

Figure 4-5 Spatiotemporal diagram of the number densities of excited species: $Xe^*(met)$ (upper), $Xe_2^*(^3\Sigma_u^+)$ (middle) and electron temperature (bottom)..... 88

Figure 4-6 Two snapshots of total species of (a) and (b) in the period I, (c) and (d) in the period II-1, (e) and (f) in the period II-2, (g) and (h) in the period III..... 92

Figure 4-7 The temporal variations of (a) applied voltage (V_a), dielectric voltage (V_d) and gap voltage (V_g) in upper figure (b) discharge current density at inner side ($r=0.8$ cm) and accumulated charge (Q_a) in bottom figure utilizing distorted square voltages over a cycle..... 93

Figure 4-8 The temporal variations of number density of electron, the ion species Xe^+ and Xe_2^+ , the main excited species $Xe^*(met)$, the main excimer species $Xe_2^*(^3\Sigma_u^+)$ and Te during the period $t=0 \sim 2$ (μs)..... 94

Figure 4-9 The power emission in the upper figure and power deposition utilizing distorted square voltages over a cycle..... 95

Figure 4-10(a) The efficiency and P_{172} under different power source. (b) The deposition power and power partition under different power source..... 96

Figure 4-11 The comparison of light power emission (P_{172}) between sinusoidal voltages (the upper figure) and distorted square voltages (the bottom figure)..... 97

Figure 4-12 The comparison of power deposition between sinusoidal voltages (the upper figure) and distorted square voltages (the bottom figure). 98

Figure 4-13 A snapshot of distributions of electron energy consumption components using distorted square voltages. 99

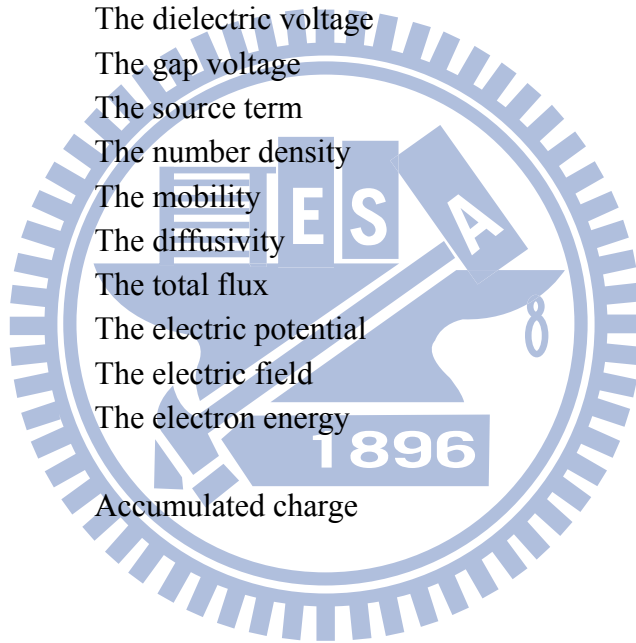
Figure 5-1 Spatial distribution of cycle averaged discharge properties: a) VUV light emissions across the gap b) power depositions of charged species across the gap..... 100

| | |
|---|------------|
| Figure 5-2 Spatiotemporal diagram of: a) 172 nm line UVU light emission and b) electron power deposition..... | 101 |
| Figure 5-3 Spatiotemporal diagram of power depositions: a) atomic xenon ion and b) molecular xenon ion..... | 102 |
| Figure 5-4 Effect of frequency on: a) η_{172}, P_{tot} and P_{172}, b) power deposition of various charged species, and c) fraction of power deposition for different charged species at 400 torr of gas pressure, 4.5 mm of gap distance and 2 dielectric layers. | 104 |
| Figure 5-5 Effect of gas pressure on: a) η_{172}, P_{tot} and P_{172}, b) power deposition of various charged species, and c) fraction of power deposition for different charged species at 50 kHz of power source, 4.5 mm of gap distance and 2 dielectric layers. | 106 |
| Figure 5-6 Spatial distribution of cycle-averaged power densities of various charged species at different gas pressus: a) electron, b) atomic xenon ion and c) molecular xenon ion. | 108 |
| Figure 5-7 Effect of gap distance on: a) η_{172}, P_{tot} and P_{172}, b) power deposition of various charged species, and c) fraction of power deposition for different charged species at 50 kHz of power source, 400 torr of gas pressure and 2 dielectric layers..... | 110 |
| Figure 5-8 Spatial distribution of cycle-averaged power densities at different gap distances: a) VUC emission and b) ions and electron..... | 111 |
| Figure 5-9 Effect of number of dielectric materials on: a) η_{172}, P_{tot} and P_{172}, b) power deposition of various charged species, and c) fraction of power deposition for different charged species at 50 kHz of power source, 400 torr of gas pressure and 4.5 mm of gap distance..... | 113 |
| Figure 5-10 Spatial distribution of cycle averaged properties for one and two dielectric cases: a) electric field and b) power densities of charged species at 50 kHz of power source, 400 torr of gas pressure and 4.5 mm of gap distance. | 114 |

| | |
|---|------------|
| Figure 6-1 Comparison of the experimental and simulated data with and without gas heating. | 115 |
| Figure 6-2 The spatial variations of background gas temperature (T_g) at different pressures across the discharge gap. | 116 |
| Figure 6-3 The spatial variation of ionic ohmic heating and electron energy loss due to elastic collision with xenon at different pressures with gas heating. | 117 |
| Figure 6-4 The spatial variations of background gas temperature (T_g) w/ $k = \text{const}$ at different pressures across the discharge gap. | 118 |
| Figure 6-5 The variation of thermal conductivity in the region of $T_g = 400 - 700$. | 119 |
| Figure 6-6 The distribution of T_g at $r = 1$ cm in the region of 100 – 513 torr. | 120 |
| Figure 6-7 The spatial distribution of background gas temperature (T_g) and number density (N_g) at 510 torr across the discharge gap. | 121 |
| Figure 6-8 The comparison of temporal variations of charge species and T_e at 510 torr between with gas heating and without gas heating. | 122 |
| Figure 6-9 The comparison of spatial variations of Xe^+-to-Xe_2^+ ion conversion and $e\text{-Xe}_2^+$ recombination at 510 torr between with and without gas heating. | 123 |
| Figure 6-10 The temporal variations of a) applied voltage (V_a) and electron number density (N_e) b) electron temperature (T_e) in the range of $p=100\text{-}510$ torr over a cycle. | 124 |
| Figure 6-11 Temporal distribution of electron power densities in period 0-2 (μs) at different gas pressures. | 125 |
| Figure 6-12 Temporal distributions of electron elastic collision loss power densities in period 0-2 (μs) at different gas pressures. | 126 |

Nomenclature

| | |
|--------------------|--|
| ε | The dielectric constant |
| f | The power source frequency |
| P | The gas pressure |
| P_{in} | The input power density |
| $P_{\text{out},k}$ | The light output power density generated from k th kind of excited species |
| T_e | The electron temperature |
| i_T | The discharge current |
| i_C | The conduction current |
| i_D | The displacement current |
| V_a | Applied voltage |
| V_d | The dielectric voltage |
| V_g | The gap voltage |
| S | The source term |
| n | The number density |
| μ | The mobility |
| D | The diffusivity |
| $\vec{\Gamma}$ | The total flux |
| ϕ | The electric potential |
| \vec{E} | The electric field |
| ε_e | The electron energy |
| Q_a | Accumulated charge |



Chapter 1

Introduction

1.1 Background and Motivation

1.1.1 History and Applications

Because of its relatively low cost and low pollution, the excimer ultraviolet (EUV) lamp has found wide applications since its debut in a form of dielectric barrier in xenon gas in 1988 [Eliasson and Kogelschatz, 1988]. These include, for example, surface cleaning [Kane *et al.*, 2004], plasma display [Park *et al.*, 2007], LCD backlighting [Shiga *et al.*, 2001], water quality purification [Safta, 2004], material deposition [Buck *et al.*, 1998] and material processing [Zhang and Boyd, 1996] in the semiconductor industry. EUV lamp emission is caused by the excimer falling from excited states to the ground state. An excimer (originally short for excited dimer) is an unstable dimeric with a lifetime of about 10 ns. The important features of an excimer include: emission with narrow wavelength bandwidth, high efficiency and free radiation direction. Two typical examples are the formation of Xe_2^* or XeCl^* excimer complexes. The EUV lamp has a dielectric barrier-type discharge which is a high-pressure non-equilibrium transient discharge. A primary function of the dielectric barrier is that it can suppress the occurrence of arc discharge, thereby preventing

damage to the metallic electrodes.

Because the plasma physics and chemistry inside the EUV lamp are very complex and difficult to measure, its design still heavily depends on the trial-and-error method that is both time-consuming and costly. Thus, detailed simulation of excimer discharge physics and chemistry could become a viable method for understanding the complicated plasma physics inside the lamp which, in turn, would lead to a better design.

1.1.2 Dielectric Barrier Discharges

The dielectric barrier discharge is a very high-pressure non-equilibrium transient discharge which usually consists of many tiny parallel current filaments showed in [Figure 1.1](#) [[Kogelschatz et al., 1999](#)]. The barrier plays a role in producing high-energy electrons and suppressing arc discharges if micro-filament discharge has started. A primary feature of the lamp is that the dielectric barrier suppresses the occurrence of arc discharges and damage to the metallic electrode. Dielectric barrier discharge excimer lamps were originally driven by an alternating voltage, usually a sine wave. Under special conditions also homogenous discharges can be obtained. Most of the applications are operated up to now with filamentary discharges; but homogeneous discharges are coming up and open new perspectives.

In the filamentary mode the four typical stages are shown in [Figure 1.2](#)

[Chirokov *et al.*, 2005]. If the electric field in the gas gap is sufficiently high to initiate avalanches, the breakdown starts with the Townsend phase. Next, a streamer occurs and a conducting channel-the filament-is formed. Charges are then transferred through the channel and accumulate at the dielectric surface. The voltage across the filament is finally suppressed and the discharge dies out. Group of local processes in the discharge gap initiated by avalanche and developed until electron current termination usually called microdischarge.

1.1.3 Breakdown Mechanism

The breakdown mechanism is based on the streamer theory, originally developed by Loeb [1960], Raether [1964] and Meek [1978]. A simplified conceptual development of a streamer begins with a single electron in an electric field. In the electric field the electron gains enough energy to ionize an atom or molecule, resulting in subsequent ionization and then an electron avalanche. This electron avalanche creates a strong positive field or streamer head within a small volume, which propagates across the gap, followed by a thin plasma channel (streamer). The streamer is a highly non-equilibrium plasma that is in a formative phase, with a small “head” that has a high space-charge limited field, and produces significant ionization through the presence of energetic electrons. The small head is followed by a “tail” with much lower electric field [Raizer, 1991]. Once the streamers bridge the gap

between the anode and the cathode, the plasma channel will become highly conductive and the discharge, an array of streamers, typically collapses to a single conducting channel.

1.1.4 Overview of Excimers

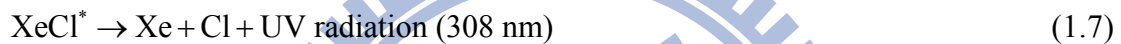
An excimer (originally short for excited dimer) is an unstable dimeric or heterodimeric molecule formed from two species, at least one of which is in an electronic excited state. The lifetime of an excimer is very short, on the order of nanoseconds. The feature of excimer include single wavelength, high efficiency and free radiation direction. The generation of excimer results from the reaction mechanism like ionization or excitation and collision process in the discharge. Emission of UV is due to the process that excimer falls from excited states to ground state. Excimer formation requires frequent three-body collisions and is therefore favored in a high-pressure discharge.

In general, excimer lamps utilize high-pressure rare-gas or rare-gas/halogen mixtures. Two typical examples are the formation of Xe_2^* or XeCl^* excimer complexes. Firstly, the formation of Xe_2^* is formed essentially from neutral excited atoms (which Xe is the working gas). This process takes place in microdischarge channels and consists of three consecutive stages:





Secondly, the formation of XeCl^* is formed mainly via recombination of ions with impurity in the working gas. A typical process consists of the following reaction steps:



Other examples of excimer complexes may include, but not limit to, the rare-gas dimmers Ar_2^* radiating at 126nm, Kr_2^* at 146 nm, the halogen dimmers Cl_2^* at 259 nm, Br_2^* at 289 nm, I_2^* at 324 nm and the rare gas/halogen complexes ArCl^* at 175 nm, KrBr^* at 207 nm, KrCl^* at 222 nm, XeI^* at 253 nm, XeBr^* at 238 nm, XeCl^* at 308 nm [Gellert and Kogelschatz, 1991; Zang and Boyd, 1998].

1.2 Discharge Control

There exist a variety of methods to control dielectric barrier discharge. Besides voltage waveform, voltage amplitude, frequency, the electrode configuration, the number of the dielectric barriers and the kind of gas in the gap determine the microdischarge distribution and intensity. Thus, understanding the physical mechanism is very important in designing higher-efficiency excimer UV lamp.

1.3 Literature Survey

1.3.1 Xenon Excimer Discharges Driven by the Sinusoidal Voltages

Traditional excimer UV xenon lamps are driven by sinusoidal voltage waveforms, with discharge efficiency typically in the range of 10-20 %, and the discharge consists of multiple narrow filamentary channels [Stockwald and Neiger, 1995]. Simulation of xenon DBD driven by sinusoidal voltage waveforms using the one-dimensional planar fluid modeling has been proposed with gas pressures and frequencies in the range of 10-400 torr and 50 kHz – 1 MHz, respectively, by Oda *et al.* [1999]. They found the efficiencies of spontaneous emission from excimers and resonance-state atoms increase with an increase in the input powers for gas pressures higher than 50 torr. They have applied pulse voltages with trapezoidal and sinusoidal waveforms at different gap lengths. They have found in both waveforms the light output power depends not only on the amplitude of voltage waveforms but also on the discharge gap length. At the narrower discharge gap, the light output efficiency is improved by increasing the rate of increase of the applied voltage when the trapezoidal pulse is applied and by decreasing the duty ratio in the sinusoidal case. However, these waveforms were not realistic.

1.3.2 Xenon Excimer Discharges Driven by the Pulsed Voltages

A dramatic increase in efficiencies of up to 40% has been demonstrated

experimentally (included transmission losses through the quartz and geometric loss) by using short (<750 ns) pulsed voltages interrupted by long idle periods (~ 40μs) [Vollkommer and Hitzschke, 1997]. Carman and Mildren [2003] found that VUV generation efficiency could reach 61% using very short voltage pulses through one-dimensional planar fluid modeling. Beleznai *et al.* [2006] compared the simulations results of a xenon EUV lamp (75 torr, driven by short voltage pulses) with the experimental data to validate their model using one-dimensional planar fluid modeling with very complex plasma chemistry in up to 99 reaction channels. Avtaeva and Kulumbaev [2008] have analyzed the difference of simulated results between two sets of different chemical reaction processes. However, there were no systematic simulations by varying all possible parameters for xenon excimer discharge driven by realistic pulsed voltages, which has been used in practical applications.

1.3.3 Gas Heating in Gas Discharges

Serikov and Nanbu [1997] have used 1-D particle-in-cell method to analyze gas heating effect in Argon gas. They analyzed the balance of power input into the gas due to the energetic neutrals, sputtered atoms and ions. Bogaerts *et al* [2000] extended the particle-in-cell method to 2D. It was found that the temperature can increase significantly at high voltages, pressures and currents. Revel *et al* [2000] have used a hybrid method to analyze gas heating effect in Argon gas. They found a large fraction

of the energy gained by the ions in the sheath. Benmoussa *et al* [2007] investigated the effect of gas heating near the electrode of an excimer lamp. However, the boundary conditions in predicting the gas temperature distribution are problematic. They have used temperature jump boundary conditions, which are not physical for a high-pressure discharge. Belostotskiy *et al* [2008] measured experimental I-V characteristics of dc microdischarges in helium at different operating pressures ($p = 300\text{-}800$ torr) and found the classical scaling law of the cathode layer (sheath) did not apply if neglecting the influence of the neutral gas heating. Recently, we have observed experimentally [Lu, 2008] a peak VUV emission illuminance at about 400 torr of background xenon and the discharge could not even sustain with a pressure larger than 440 torr. However, most simulation studies of the gas heating effect were focused on low-pressure discharges and lacking in high-pressure environment, although the type of operation condition is common in excimer lamp discharges.

1.4 Objectives and Organization of the Thesis

1.4.1 Specific Objectives

Based on previous reviews, the specific objectives of the thesis are summarized as follows:

1. To understand the detailed discharge physics and chemistry in a co-axial

homogeneous xenon excimer lamp driven by sinusoidal voltages via a self-consistent one-dimensional fluid modeling.

2. To understand the detailed discharge physics and chemistry in a co-axial homogeneous xenon excimer lamp driven by distorted bipolar square voltages and compare with those by sinusoidal voltages via a self-consistent one-dimensional fluid modeling.
3. To conduct a parametric study in a co-axial homogeneous xenon excimer lamp driven by distorted bipolar square voltage through a self-consistent one-dimensional fluid modeling and to understand the corresponding effects on the performance of the discharges.
4. To understand the gas heating effect on the performance of the co-axial homogeneous xenon excimer lamp driven by distorted bipolar square voltage through a self-consistent one-dimensional fluid modeling

1.4.2 Organization of the Thesis

According to the above objectives, this thesis is organized as follows:

Chapter 2 introduces the fluid modeling equations, numerical techniques we use to solve these equations for understanding the plasma physics and chemistry in the lamp.

Chapter 3 describes the validation of the fluid modeling in xenon discharge

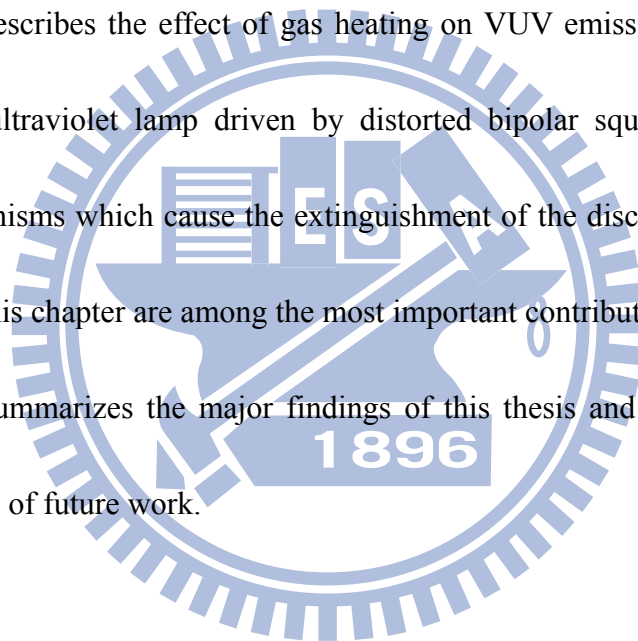
simulation, in which two cases are used for this purpose.

Chapter 4 describes the comparison of the VUV emission efficiency of a coaxial xenon excimer ultraviolet lamp between sinusoidal voltages and distorted bipolar square voltages.

Chapter 5 describes the results of a parametric study of VUV emission from a coaxial xenon excimer ultraviolet lamp driven by distorted bipolar square voltages.

Chapter 6 describes the effect of gas heating on VUV emission from a coaxial xenon excimer ultraviolet lamp driven by distorted bipolar square voltages. Two important mechanisms which cause the extinguishment of the discharge is presented. The findings in this chapter are among the most important contributions in this thesis.

Chapter 7 summarizes the major findings of this thesis and the outline of the recommendations of future work.



Chapter 2

Fluid Modeling

2.1 Basic Equations of Fluid Modeling

In the framework of fluid modeling, electron and ion number densities are calculated as functions of time and space resulting from the coupled solution of the species continuity equation, species momentum equation, species energy equation, and field equations. Since the fluid modeling equations are similar for most of the gas discharges, we have only summarized a typical set of equations as the model equations for the purpose of demonstration. Note that we have not included flow convection effects in the present study.

2.1.1 Continuity Equations

The general continuity equation for ion species can be written as,

$$\frac{\partial n_p}{\partial t} + \vec{\nabla} \cdot \vec{\Gamma}_p = \sum_{i=1}^{r_p} S_{p_i} \quad p=1, \dots, K \quad (2.1)$$

where n_p is the number density of ion species p , K the number of ion species, r_p the number of reaction channels that involve the creation and destruction of ion species p , and $\vec{\Gamma}_p$ the particle flux that is expressed, based on the drift-diffusion approximation, as:

$$\vec{\Gamma}_p = \text{sign}(q_p) \mu_p n_p \vec{E} - D_p \vec{\nabla} n_p \quad (2.2)$$

$$\vec{E} = -\nabla \phi \quad (2.3)$$

where q_p , \vec{E} , μ_p , D_p and α_{iz} are the: ion charge, electric field, electron mobility, electron diffusivity, and ionization rate, respectively. Note that the form of source term S_{p_i} can be modified according to the modeled reactions describing how ion species p is generated or destroyed in reaction channel i . Boundary conditions at the walls have been applied, taking into consideration thermal diffusion, drift and diffusion fluxes.

The continuity equation for electron species e can be written as,

$$\frac{\partial n_e}{\partial t} + \vec{\nabla} \cdot \vec{\Gamma}_e = \sum_{i=1}^{r_e} S_{e_i} \quad (2.4)$$

where n_e is the number density of ions, r_e the number of reaction channels that involve the creation and destruction of electrons, and $\vec{\Gamma}_e$ the corresponding particle flux that is expressed, based on the drift-diffusion approximation, as:

$$\vec{\Gamma}_e = -\mu_e n_e \vec{E} - D_e \vec{\nabla} n_e \quad (2.5)$$

where μ_e and D_e are the electron mobility and electron diffusivity, respectively.

These two transport coefficients can be readily obtained as a function of electron temperature from the solution of a publicly available computer code for the Boltzmann equation, named BOLSIG+ [16]. As with S_{p_i} , the form of S_{e_i} can also

be modified according to the modeled reactions which generate or destroy the ion in reaction channel i . Boundary conditions at the walls are applied, taking into consideration thermal diffusion, drift and the diffusion fluxes of electrons. Secondary electron emissions or photo-electron emissions from the solid walls can be readily added if necessary.

The continuity equation for neutral species can be written as,

$$\frac{\partial n_{uc}}{\partial t} + \vec{\nabla} \cdot \vec{\Gamma}_{uc} = \sum_{i=1}^{r_{uc}} S_{uc_i} \quad uc=1, \dots, L \quad (2.6)$$

where n_{uc} is the number density of uncharged species uc , L the number of neutral species, r_{uc} the number of reaction channels that involve the creation and destruction of uncharged species uc , and $\vec{\Gamma}_{uc}$ the corresponding particle flux, omitting convection effects, which can be expressed as:

$$\vec{\Gamma}_{uc} = -D_{uc} \vec{\nabla} n_{uc} \quad (2.7)$$

where D_{uc} is the diffusivity of neutral species. Similarly, the form of S_{uc_i} can also be modified according to the modeled reactions which generate or destroy the species in reaction channel i . Neumann boundary conditions at the walls are applied since surface reactions have not been considered in the present study.

2.1.2 Electron Energy Density Equation

The electron energy density equation can be expressed as,

$$\frac{\partial n_\varepsilon}{\partial t} + \nabla \cdot \bar{\Gamma}_{n_\varepsilon} = -e\bar{\Gamma}_e \cdot \bar{E} - \sum_{i=1}^{s_\varepsilon} \varepsilon_i S_i - 3 \frac{m_e}{M} n_e k_B \nu_m (T_e - T_g) \quad (2.8)$$

where $n_\varepsilon \left(= \frac{3}{2} n_e k_B T_e \right)$ is the electron energy density, T_e the electron temperature, ε_i the energy loss for the i^{th} inelastic electron collision, k_B the Boltzmann constant, ν_m the momentum exchange collision frequency between electron (mass m_e) and background neutral (mass M), T_g the background gas temperature, and $\bar{\Gamma}_{n_\varepsilon}$ the corresponding electron energy density flux, which can be written as:

$$\bar{\Gamma}_{n_\varepsilon} = \frac{5}{2} k_B T_e \bar{\Gamma}_e - \frac{5}{2} \frac{n_e k_B T_e}{m_e \nu_m} \nabla (k_B T_e) \quad (2.9)$$

The second term on the right-hand side of Eq. (2.8) represents the sum of the energy losses of electrons due to inelastic collision with other species. The last term on the right-hand side of Eq. (2.8) can be ignored for low-pressure gas discharges, although it is important for medium-to-atmospheric pressure discharges. Similarly, boundary conditions at the walls have been applied, taking into consideration thermal diffusion, drift and diffusion fluxes. Secondary electron emission and other boundary effects may be readily added if needed.

2.1.3 Field Equation

Poisson's equation for electrostatic potential distribution can be expressed as

$$\nabla \cdot (\varepsilon \nabla \varphi) = - \left(\sum_{i=1}^K q_i n_i - e n_e \right) \quad (2.10)$$

where φ is the potential and ε is a function of position, whose value is either the

vacuum or dielectric permittivity, depending upon the problem.

2.1.4 General Boundary Conditions

Boundary conditions for the charge species fluxes towards the dielectric are defined as follows [Meunier, 1995; Boeuf, 1995; Veerasingam, 1997; Punset, 1998; Ivanov, 1999]:

$$\vec{\Gamma}_i \cdot \vec{n} = a \operatorname{sgn}(q) \mu_i n_i \vec{E} \cdot \vec{n} + \frac{1}{4} n_i v_{th,i} \quad (2.11)$$

where \vec{n} is the normal vector pointing toward the dielectric and v_{th} is the thermal velocity $v_{th,i} = \sqrt{\frac{8k_B T_i}{\pi m_i}}$ in which T is temperature (K), k_B is Boltzmann constant and m_i is the mass of charge species. The number a is set to be unity if the drift velocity is directed toward the dielectric and to be zero otherwise:

$$a = \begin{cases} 1 & \operatorname{sgn}(q) \mu \vec{E} \cdot \vec{n} > 0 \\ 0 & \operatorname{sgn}(q) \mu \vec{E} \cdot \vec{n} \leq 0 \end{cases} \quad (\operatorname{sgn}(q) \text{ presents species charge}) \quad (2.12)$$

In the case of electrons, a flux towards to the dielectric is defined as follows:

$$\vec{\Gamma}_e \cdot \vec{n} = -a_e \mu_e n_e \vec{E} \cdot \vec{n} + \frac{1}{4} n_e v_{th,e} \quad (2.13)$$

The boundary condition of continuity equation for neutral species uc is always set as the Neumann boundary, since no surface reactions are considered in this thesis. It is thus set as

$$\vec{\Gamma}_{uc} \cdot \vec{n} = 0 \quad (2.14)$$

The boundary condition of the electron energy density at dielectric surface is written

as

$$\vec{\Gamma}_e \cdot \vec{n} = 2k_B T_e \vec{\Gamma}_e \quad (2.15)$$

The evolution of surface charge density on the dielectric barrier is calculated by integrating fluxes of charged particles directed to the barrier surface:

$$\frac{\partial \sigma}{\partial t} = e(\sum \vec{\Gamma}_i - \vec{\Gamma}_e) \cdot \vec{n} \quad (2.16)$$

It is assumed that charges remain on the barrier surface until recombining with charges of opposite sign.

2.1.5 VUV Emission Efficiency

Since we only considered one-dimensional radial fluid modeling, the input power density, P_{in} (or dissipated power), to the discharge is thus defined as:

$$P_{in} = \frac{2}{T(r_2^2 - r_1^2)} \int_0^T \int_{r_1}^{r_2} j_c(r, t) E(r, t) r dr dt \quad (2.17)$$

where T is the period of the applied voltage and j_c is the conduction current density caused by the electrons and ions. Note that r_1 and r_2 are the inner and outer radii of the gas gap. The VUV (vacuum UV) light output power density, $P_{out,k}$, generated from the k th kind of excited species, is defined as:

$$P_{out,k} = \frac{2h\nu_k}{T(r_2^2 - r_1^2)} \int_0^T \int_{r_1}^{r_2} \frac{n_k(r, t)}{\tau_k} r dr dt \quad (2.18)$$

where $h\nu_k$, τ_k and n_k are the photon energy of the VUV light, lifetime and concentration of the excimer species, respectively. Thus, the VUV emission efficiency due to k^{th} excimer species is given as:

$$\eta_k = \frac{P_{out,k}}{P_{in}} \quad (2.19)$$

2.1.6 Discharge Current, Dielectric Voltage and Gap Voltage

The discharge current $i_T(t)$ in this thesis defined as the sum of conduction current $i_C(t)$ and displacement current $i_D(t)$ and is written as

$$i_T(t) = i_C(t) + i_D(t) \quad (2.20)$$

The voltage across the electrodes $V_s(t)$ is written as

$$V_s(t) = V_d(t) + V_g(t) \quad (2.21)$$

where $V_d(t)$ is the total dielectric voltage across dielectric material(s) and $V_g(t)$ is the gap voltage across the gap that is filled with discharge gas.

2.2 Numerical Method and Algorithms

The numerical scheme and algorithms of the fluid modeling code, which was developed previously in our group and applied to simulate the EUV emission of xenon lamp, was introduced briefly in the following. Details of implementation can be found in Hung [2010].

2.2.1 Numerical Discretization

In this study, the above equations were recast into a one-dimensional form and discretized using the finite-difference method. The resulting system of nonlinear algebraic equations was then solved using a fully implicit backward Euler's method in the temporal domain, with the Scharfetter-Gummel scheme for mass fluxes in the

spatial domain.

2.2.2 Parallel Fully Implicit Newton-Krylov-Swartz-Algorithm

At each time step, the resulting algebraic nonlinear system was solved by a parallel fully coupled Newton-Krylov-Swartz (NKS) algorithm [Cai *et al* 1998], in which the nonlinear discretized equations of a large sparse system was solved using an additive Schwarz preconditioned GMRES. The parallel code was implemented using physical domain decomposition method.

We have used an inexact or exact solution, such as incomplete LU (ILU) or LU factorizations, in each subdomain for the preconditioning. We evaluated the Jacobian matrix entries using a hybrid analytical-numerical method, in which the entries involving the derivative, with respect to number density (e.g. the source terms of species continuity equations), could be easily expressed analytically without resorting to numerical approximation. Other entries were evaluated using a standard finite-difference method. This strategy was especially useful for plasma simulations with a large number of species and reaction channels.

Chapter 3

Validation of the Fluid Modeling in Xenon Discharge Simulation

In this chapter, we will present the validations of the one-dimensional fluid modeling by comparing with previous simulations and measurements. We first describe the xenon plasma chemistry we have used and then followed by the two cases of validations we have conducted. Finally, this chapter is concluded by summarizing the major findings.

3.1 Xenon Plasma Chemistry

In the current study, we have selected the xenon plasma chemistry that is basically the same as that used in Oda *et al.* [1999], which consists of 9 species and 24 reaction channels, as listed in [Table 3-1](#) in order to save the computational time. These reaction channels included electron-neutral elastic collision (No. 1 in [Table 3-1](#)), direct electron impact ionization (No. 2 in [Table 3-1](#)), excitation (No. 3-5 in [Table 3-1](#)), stepwise ionization (No. 6 in [Table 3-1](#)), recombination (No. 7 in [Table 3-1](#)), heavy particle collision (No. 8-18 in [Table 3-1](#)) and radiation process among electrons, ions, associated excited atoms, excimer xenon and ground-state xenon atoms (No. 19-24 in [Table 3-1](#)). [Figure 3-1](#) shows schematically these reaction channels using the

energy diagram for a better overview of the inter-relation among the species.

3.2 Case-1: 1-D Homogenous Planar Xenon discharge

3.2.1 Simulation Conditions

The test conditions are the same as in [Beleznai *et al.*, 2006] and are briefly described as follows: pure xenon, a pressure of 75 torr, a frequency of 20kHz, a gap distance of 9.65 mm, dielectric thickness of 0.7 mm and applied voltage maximum of 3 kV. Simulation conditions we used are summarized as: 405 uniform grid points, a time step size in the range of $10^{-13} \sim 5 \times 10^{-11}$ s, and parallel computation on four cores.

3.2.2 Results and Discussion

Figure 3-2 shows the comparison of the simulated discharge currents between the Beleznai *et al.*'s and ours in a cycle, Two large spikes are both found from the discharge currents in the two simulated results when the applied voltage fast rises and drops. The magnitude of the simulated spikes in our result are in reasonable agreement with that of Beleznai *et al.*, although the simulation has not reproduced the multiple spikes. The reason could probably be attributed to that we have adopted a much simpler plasma chemistry than that of Beleznai *et a.* and also we have assumed a homogeneous discharge. Nevertheless, the trend of the discharge currents coincident with each other, which shows that the use of simple plasma chemistry can still capture most of the physics inside the xenon lamp.

3.3 Case-2: 1-D Homogenous Cylindrical Xenon discharge

3.3.1 Simulation Condition

Figure 3-3(a) depicts a sketch of the coaxial xenon excimer lamp simulated in the present study. For explaining the typical discharge physics and chemistry, we have selected the following simulation conditions for convenience (see Figure 3-3(b)). The tube length is 70 cm, the gap distance (d) in the radial direction is 3 mm, and both the inner and outer quartz tubes (d_i+d_o) are 1 mm thick. An inner-powered electrode with a radius of 7 mm is placed in direct contact with the inner quartz tube and an outer mesh grounded electrode (~92% in porosity) with a radius of 12 mm is placed outside the outer quartz tube. The complicated three-dimensional geometrical structure is simplified as a one-dimensional radial coordinate system in the current study as the first step in understanding the discharge physics and chemistry without the complications of geometry. The dielectric constant of the quartz tube was 4.0, and power supply frequency f and xenon gas pressure p are fixed at 50 KHz and 400 torr, respectively.

3.3.2 Results and Discussion

Figure 3-4 shows the comparison of the simulated and the experimental discharge currents in a cycle. Note the experimental data were provided by Industrial Technology Research Institute in Taiwan. Several fast oscillating current spikes are

found from the measured currents, while only a single major spike is found from the simulated data. The reason should be we have employed one-dimensional radial fluid modeling to simulate the discharge physics. However, the magnitude of the simulated spike is reasonably comparable to that of the measured data. Note that the actual EUV lamp has a very complex three-dimensional geometric structure with a highly porous (~91%) outer grounded electrode. Also, the measured voltages are slightly more positive at the inner electrode than at the outer electrode in the post-breakdown period, which should be attributed to the auto-DC-bias effect because of the unequal area of the inner and outer electrodes. Note that the slightly negative current is within the experimental uncertainties of the current probe. In the current study, we do not take this into account in the simulation. However, based on the comparison between the 1-D radial fluid modeling and the experiments, we could conclude that the use of the one-dimensional radial fluid model is able to reasonably capture the major discharge physics inside the real EUV lamp.

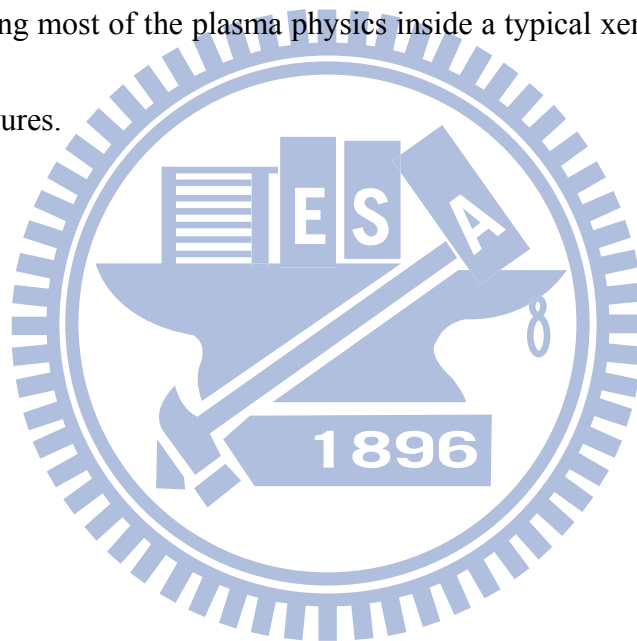
3.4 Brief Summary of This Chapter

Major findings of this chapter are summarized briefly as follows:

1. For Case-1 validation, the trend of the two simulation discharge currents agree well with previous simulation data. However, the magnitude of the simulated spike in our result is not in quantitative agreement with that of Beleznai *et al.*'s,

which should be due to the simplified plasma chemistry.

2. For Case-2, the results of simulated and the experimental discharge currents agree reasonably well, although the complexity of electrode geometry is greatly simplified in the present simulation.
3. Based on the two validation cases, we can conclude that the present one-dimensional fluid modeling with the simplified plasma chemistry is capable of reproducing most of the plasma physics inside a typical xenon lamp operating at high pressures.



Chapter 4

Enhancement of VUV Emission from a Homogeneous Coaxial Xenon Excimer Ultraviolet Lamp Driven by Distorted Bipolar Square Voltages

In this chapter, we present the enhancement of VUV emission from a coaxial xenon excimer ultraviolet lamp driven by distorted bipolar square voltages as compared to that driven by sinusoidal voltages. The simulation conditions are based on the Case-2 in Chapter 3. We first present the results of discharge properties by sinusoidal voltages in detail, which serves as the baseline for comparison. Then, the results of discharge properties by distorted bipolar square voltages are presented and compared to the sinusoidal case wherever is possible. Before concluding remarks, general VUV emission power and efficiency is presented. Finally, a brief summary is made at the end of this chapter.

4.1 Discharge Properties by Sinusoidal Voltages

4.1.1 Phase Diagrams of Key Discharge Properties

In this section, we present the simulation results of xenon discharge driven by sinusoidal voltage waveforms using phase diagrams of several important discharge

properties.

Figure 4-1 shows the phase diagrams of concentration of charged species (electron, atomic xenon ion and molecular xenon ion), while Figure 4-2 shows the phase diagrams of $\text{Xe}^*(\text{met})$ and $\text{Xe}_2^*(^3\Sigma_u^+)$ that are two important excited species for VUV emission (172 nm), and of the electron temperature. Note the red dashed and black solid curves in Figure 4-1 (top) represent the temporal variation of applied sinusoidal voltage and spatial-average number density of electrons in the gap. In general, the phase diagram can be divided into six periods according to the temporal variation of electron number density because the electrons can respond immediately to the variation of electric field. The periods I and IV are pre-breakdown regions, the periods II and V are breakdown regions and the periods III and VI are post-breakdown regions. In period II and V, it can be further divided into two sub-periods (II-1 and II-2; V-1 and V-2). The trend of species in the first half cycle (I, II and III) is similar to the second half cycle (IV, V and VI), except that the discharge current is opposite to each other and the species concentrations in the second half cycle is larger than those in the first half cycle because the electric field at inner side ($r=0.8\text{cm}$) is larger than at outer side ($r=1.25\text{cm}$) due to smaller radius of curvature. In the following, we only describe the discharge physics in the first half cycle for brevity.

Period I

In this pre-breakdown period, the total number of electrons decreases with time because the electrons are attracted to anode side and accumulated on the inner dielectric tube due to its rising voltage. Nearly no ionization occurs during this period as can be seen from the very concentration of the atomic xenon ions (middle of [Figure 4-1](#)) which originate from the direct electron impact ionization. Albeit the electron temperature is very high near the outer dielectric tube (cathode side) (bottom of [Figure 4-2](#)) due to the rising voltage at the inner electrode, the breakdown does not occur because of only very small number of electrons in that region. Similarly, both $Xe^*(met)$ and $Xe_2^*(^3\Sigma_u^+)$ are very few across the gap in this period. However, near the inner dielectric tube (0.8-1.0 cm) the quasi-neutrality holds with the plasma density of $\sim 5 \times 10^{16} \text{ (m}^{-3}\text{)}$, while the molecular xenon ions (Xe_2^+) prevails across the gap. At the end of Period I, the electric field near the outer dielectric tube (cathode side) increases to a value at which the breakdown occurs instantaneously at the start of Period II.

Period II

In Period II-1, the breakdown occurs at $r \approx 1.1 \text{ cm}$ and moves towards outer quartz tube in a speed of $\sim 2,000 \text{ m/s}$ (from anode towards cathode) (middle of [Figure 4-1](#)) by direct electron impact ionization, the number of electrons rapidly increases to the

maximal value within 1 μs at $r \approx 1.18$ cm and then decreases gradually afterwards (top of [Figure 4-1](#)). At the same time, number of molecular xenon ions increases rapidly in the same fashion through the three-body collision channel (No. 16 in [Table 3-1](#)), which also rapidly consumes the atomic xenon ions and the molecular xenon ions become the dominating ions in Period II-2 (bottom of [Figure 4-1](#)). In addition, both $\text{Xe}^*(\text{met})$ and $\text{Xe}_2^*(^3\Sigma_u^+)$ are very abundant because of the excitation of ground-state xenon by the energetic electrons (top and middle of [Figure 4-1](#)). Interestingly, the temporal location of where the maximal amount of $\text{Xe}_2^*(^3\Sigma_u^+)$ occurs is shifted slightly after that of the maximal amount of $\text{Xe}^*(\text{met})$ because the former is formed solely through the reaction between $\text{Xe}^*(\text{met})$ and ground-state xenon (No. 12 in [Table 3-1](#)). In Period II-2 that lasts less than 1 μs , the quasi-neutral region forms between the $r \approx 1.1$ -1.2 cm and moves from cathode side (grounded) to anode side (powered) slowly, in which the Xe_2^+ is the dominating ion species as described earlier. In addition, both $\text{Xe}^*(\text{met})$ and $\text{Xe}_2^*(^3\Sigma_u^+)$ disappear because of intense photon emission (172 nm) (No. 19 in [Table 3-1](#)) in this Period II-2. In the region of $r \approx 1.0$ -1.2 cm, beginning from the later period of Period II-1, the electron temperature decreases rapidly with time because of the shielding by the increasingly accumulated charges on both quartz tubes and the electrons lose energy in ionizing the ground-state xenon.

Period III

In this period, the quasi-neutral region expands slowly first from the cathode side (outer) towards the anode side (inner) with decreasing plasma density in the bulk (Figure 4-2). Later the electrons begin to move from the anode side (inner) towards the cathode side (outer) at $t=5-6 \mu\text{s}$, when the applied voltage decreases from the peak. In this period, both $\text{Xe}^*(\text{met})$ and $\text{Xe}_2^*(^3\Sigma_u^+)$ nearly do not exist because the electron temperatures are very low down to even 0.1 eV at the end of the Period III.

After Period III, the polarity of the applied voltage switches and the above described breakdown procedures repeat with opposite direction and location, however, with higher plasma density and more abundant excited species because of the stronger electric field near the inner electrode.

4.1.2 Temporal Variation of Discharge Properties

To further elucidate the discharge physics described in the above, we present temporal variation of several important discharge properties in Figure 4-3. Figure 4-3 shows the temporal variations of: a) the applied voltage (V_a), the dielectric voltage (V_d), the gap voltage (V_g), the discharge current density at inner side ($r=0.8 \text{ cm}$) and the accumulated charges (Q_a) and b) the spatial-average number density of electron, the ion species Xe^+ and Xe_2^+ , the metastable species $\text{Xe}^*(\text{met})$, the excimer species $\text{Xe}_2^*(^3\Sigma_u^+)$ and the electron temperature utilizing sinusoidal voltage waveform over a cycle. Note the dielectric voltage is defined as the sum of voltages across both quartz

tubes. Similarly, we divide the cycle into six periods as shown earlier in the description of [Figure 4-3](#) for the purpose of easier discussion.

Period I

In Period I (pre-breakdown region), the dielectric voltage, the gap voltage and the electron temperature increase with increasing applied voltage, while both the magnitudes of accumulated charges at inner (less positive) and outer (less negative) quartz tubes, and the number densities of electron and Xe_2^+ decrease with increasing applied voltage. The current density at inner quartz tube ($r=0.8$ cm) decreases slightly. The magnitudes of the accumulated charges at inner and outer quartz tubes decrease in this period because of incoming electrons and ions respectively as the applied voltage increases. In addition, all excited xenon species start increasing in this period because of rising electron energy,

Period II

Again, Period II (breakdown region) is divided into Periods II-1 and II-2. In Period II-1, the gap voltage has risen to some critical level that leads to very high electron energy, which makes the xenon breakdown. The abundant increase of charge species number density lead to a rapid increase of the current density at the inner dielectric surface, at which a large amount of electrons accumulate in a very short period of time.

In period II-2, Note the number density of Xe_2^+ keeps increasing through three-body ion conversion channel (No. 18 in Table 3-1), so ion accumulated on the outer anode dielectric surface (see Figure 4-3). The combined accumulated effect on the inner anode and outer cathode dielectric surface results in a much smaller gap voltage (see Figure 4-3) by shielding out the applied voltage. The reduced electric field can not offer energy to electrons and keep discharge anymore. The number density of all species and electron temperature keep reducing.

Period III:

In period III (post-breakdown region), a turning point of applied voltage at $t = 5 \times 10^{-6}$ (s) can be found. According to the turning point, period III can be divided two sub regions III-1 and III-2. In sub period III-1, gap voltage and current density keep reducing, dielectric voltage keeps rising, Q_a at inner side and outer side keep accumulating. In sub period III-2, electron no longer accumulates on the inner dielectric again and turns back to the bulk. The direction of current density turns into opposite direction. Gap voltage becomes negative from positive. The main species in the region are electron and molecular ion, but they keep reducing due to wall loss and recombination effect.

4.2 Discharge Properties by Bipolar Distorted Square

Voltages

4.2.2 Phase Diagrams of Key Discharge Properties

Figure 4-4 shows the phase diagrams of the concentrations of the charged species (electron, atomic xenon ion and molecular xenon ion), while Figure 4-5 shows the phase diagrams of $\text{Xe}^*(\text{met})$ and $\text{Xe}_2^*(^3\Sigma_u^+)$, two important excited species for VUV emission (172 nm) and electron temperature. Note that we have only shown $\text{Xe}_2^*(^3\Sigma_u^+)$, instead of $\text{Xe}_2^*(^1\Sigma_u^+)$, because the concentration of the former was much greater than the latter. We divided these phase diagrams into six periods in the temporal direction according to the temporal variation of electron number density, as only electrons can respond immediately to variations in the electric field. Periods I and IV were pre-breakdown regions, Periods II and V were breakdown regions and Periods III and VI were post-breakdown regions. Periods II and V were further divided into two sub-periods (II-1 and II-2; V-1 and V-2). The trend of discharge in the first half cycles (I, II and III) was very similar to that of the second half cycles (IV, V and VI), except that the discharge currents were opposite to each other and there were some slight differences in the properties because of the different areas of the inner and outer electrodes. Note that the blue dashed curve in the top of Figure 4-4 represents the temporal variation of the spatial-averaged number density of electrons in the gap. For brevity, we have only described the discharge physics and chemistry in the first half cycles (I, II and III) in detail, as those in the second half cycles were

fundamentally the same, with the exception as mentioned earlier.

Period I

In this pre-breakdown period, the spatial-averaged number of electrons decreased slightly with time because the electrons were attracted to the anode side (inner electrode) and accumulated on the inner dielectric tube due to its rising voltage. In the earlier part of Period I (negative applied voltage, 19.6-20 μs in both [Figures 4-4 and 4-5](#)), the concentrations of all species were low, especially the excited and metastable xenon, because the electron energy was still quite low.

In the later part of Period I (positive applied voltage, 0-0.37 μs in both [Figures 4-4 and 4-5](#)), in the central region of the gap ($r \approx 0.95$ -1.05 cm), the concentration of the atomic xenon ions (Xe^+) increased up to $\sim 10^6$ (cm^{-3}), as a result of direct impact ionization, as shown in the middle of [Figure 4-4](#). Although the electron temperatures were very high near the outer dielectric tube (cathode side) (see bottom of [Figure 4-5](#)) due to the rising voltage at the inner electrode, breakdown did not occur because of the very small number of electrons existing in that region (see top of [Figure 4-4](#)). At the same time, both the concentrations of Xe^* (met) and $\text{Xe}_2^*(^3\Sigma_u^+)$ increased to the order of $\sim 10^{10}$ (cm^{-3}) in the central region of the gap. In addition, molecular xenon ions (Xe_2^+) were abundant ($> 5 \times 10^{10}$ cm^{-3}) throughout the complete cycle; this result was due to the ion conversion, i.e., three-body collision (No. 18 in [Table 3-1](#)). Near

the inner dielectric tube ($r \approx 0.83\text{--}0.94$ cm), the quasi-neutrality was held with a plasma density of $\sim 5 \times 10^{10} \text{ cm}^{-3}$ ($n_e \gg n_{Xe_2^+} \approx n_{Xe^+}$), while the molecular xenon ions (Xe_2^+) prevailed across the gap. At the end of Period I, the electric field near the outer dielectric tube ($r \approx 1.2$ cm, cathode side) was gradually enhanced by the “cathode-directed streamer-like” ionization wave; this will be explained in a later section using snapshots of the discharge properties, at which point the breakdown occurred instantaneously at the start of Period II.

Period II

This breakdown period was further divided into two sub-periods, II-1 and II-2. In Period II-1, the breakdown occurred at $r \approx 1$ cm, where the number of electrons increased dramatically (see top of Figure 4-4), and moved towards the outer quartz tube at a speed of $\sim 7,000$ m/s (from anode towards cathode) by direct electron impact ionization. We termed this the “cathode-directed streamer-like” ionization wave; the details will be elucidated later. The number of electrons rapidly increased to the maximal value ($> 2 \times 10^{12} \text{ cm}^{-3}$) within $\sim 0.3 \mu\text{s}$ at $r \approx 1.22$ cm, and then decreased gradually afterwards (see top of Figure 4-4). At the same time, the number of molecular xenon ions increased rapidly in the same fashion through the three-body collision channel (No. 18 in Table 3-1), which indeed rapidly consumed the atomic xenon ions’, the molecular xenon ions thereby became the dominant ions in Period

II-2 (bottom of Figure 4-4). In addition, both $\text{Xe}^*(\text{met})$ and $\text{Xe}_2^*(^3\Sigma_u^+)$ were abundant across the gap because of the excitation of ground-state xenon by the still energetic electrons:

$T_e > 3$ eV (Nos. 3 and 5 in Table 3-1; top and middle of Figure 4-5). Interestingly, the temporal location where the maximal amount of $\text{Xe}_2^*(^3\Sigma_u^+)$ occurred, shifted slightly after that of the maximal amount of $\text{Xe}^*(\text{met})$ because the former was formed solely through the conversion-to-dimer reaction between $\text{Xe}^*(\text{met})$ and ground-state xenon (No. 13 in Table 3-1).

In Period II-2, which lasted less than 4 μs , the quasi-neutral region formed across the gap with a very high plasma density ($> 5 \times 10^{11} \text{ cm}^{-3}$) between the $r \approx 1.1$ -1.2 cm, and moved slowly from the cathode side (outer grounded) to the anode side (inner powered); Xe_2^+ was the dominating ion species formed through the three-body collision as described earlier. In addition, both $\text{Xe}^*(\text{met})$ and $\text{Xe}_2^*(^3\Sigma_u^+)$ began to disappear because of the conversion-to-dimer reaction (No. 13 in Table 3-1) and intense photon emission: 172 nm (No. 20 in Table 3-1) in Period II-2. In the region of $r \approx 1.05$ -1.2 cm, having begun in the later period of Period II-1, the electron temperature decreased rapidly with time because of the energy loss by ionization and excitation of the ground-state xenon. This will be made clear later using the snapshots of the discharge properties.

Period III

In this post-breakdown period, the quasi-neutral region expanded slowly from the cathode side (outer) towards the anode side (inner) with the temporally decreasing plasma density in the bulk and clear plasma sheath near both dielectric surfaces (top and bottom of [Figure 4-4](#)). This is attributed to the discharge extinguished through a vanishing electric field across the gap (nearly zero) by the shielding effect, although the applied voltage was still as high as 2 kV, as will be seen clearly later through the snapshots of discharge properties. In the latter part of Period III, the electrons began to move away from the anode side (inner) towards the cathode side (outer) at $t=5-6 \mu\text{s}$, when the applied voltage decreased from the peak (top of [Figure 4-4](#)). In Period III, both $\text{Xe}^*(\text{met})$ and $\text{Xe}_2^*(^3\Sigma_u^+)$ decreased to a very small amount ($<10^8 \text{ cm}^{-3}$), except in the early part near the cathode (outer), because the electron temperatures were very low, down to even 0.1 eV in most of the region in Period III.

4.2.3 Snapshots of Key Discharge Properties

To gain more insight into the discharge physics and chemistry, two sequential snapshots of the several key discharge properties in each period (I, II and II) are presented in [Figure 4-6](#) and described in detail in the following.

Period I

[Figures 4-6a](#) and [4-6b](#) show two typical snapshots of important discharge

properties in the earlier and later stages of Period I, respectively. They show that the peak plasma density ($\sim 8 \times 10^{10} \text{ cm}^{-3}$) was close to the anode (inner) at $r \approx 0.84 \text{ cm}$, and that it stayed nearly stationary in space, but with a very low density as compared to that of Period II, as will be shown later. However, the figures also clearly demonstrate that the electrons were attracted to the anode (inner), with the gap voltage increasing from 0.4 (Figure 4-6a) to 2 kV (Figure 4-6b). In the region around $r \approx 1 \text{ cm}$, the rapid growth of atomic ions, excited species ($\text{Xe}^*(\text{met})$) and excimer species ($\text{Xe}_2^*(\text{O}_u^+)$, $\text{Xe}_2^*(^1\Sigma_u^+)$ and $\text{Xe}_2^*(^3\Sigma_u^+)$) could be seen due to a series of collisions by energetic electrons ($\sim 4 \text{ eV}$) moving towards the anode side (inner). On the other hand, the amount of $\text{Xe}^*(\text{res})$ decreased through the reactions of conversion to metastable (No. 10 in Table 3-1) and conversion to dimers (No. 12 in Table 3-1). The main collision processes of generating excited and metastable species occurred through the excitation collision channels, such as Nos. 3 and 5 in Table 3-1. These in turn promoted the growth of excimers through the reaction channels, such as No. 13 in Table 3-1, with zero threshold energy. Interestingly, the atomic ions and electrons moved towards the cathode side (outer), which will be more clearly shown in the details of Period II. A peak value of $\sim 2 \times 10^9 \text{ cm}^{-3}$ of atomic ions (Figure 4-6b) occurred at $r \approx 1.08 \text{ cm}$ through the contribution of collision channels, such as Nos. 1, 6 and 16 in Table 3-1. Of these, the most productive channel was the electron impact

ionization (No. 1 in [Table 3-1](#)) due to the rapid increase in voltage. As the density of the metastable species grew to a certain level, the other two channels began to contribute more in generating atomic ions.

Period II

[Figures 4-6c](#) and [4-6d](#) present two typical snapshots of important discharge properties at earlier and later times in Period II-1, respectively. They show that the potential field was highly distorted near the cathode (outer) due to the shielding of the narrow quasi-neutral region (between $r \approx 1.1$ - 1.2 cm) close to the cathode side; this in turn accelerated the few electrons near the cathode side (outer) and reached a very high electron temperature (~ 5 - 6 eV) ([Figures 4-6c](#) and [4-6d](#)) at the edge of sudden change of the electric field ($r=1.16$ cm in [Figure 4-6c](#) and $r=1.18$ cm in [Figure 4-6d](#)). These energetic electrons thus ionized and excited the ground-state xenon according to the reaction channels, such as Nos. 2-5 in [Table 3-1](#), which could be seen clearly from the peaks of charged and excited species around $r \approx 1.16$ cm and $r \approx 1.18$ cm in [Figures 4-6c](#) and [4-6d](#), respectively. At the same time, the molecular xenon ions increasingly formed through the three-body ion conversion reaction channel (No. 18 in [Table 3-1](#)) which reduced the atomic ions behind the right-moving head, but still maintained strict quasi-neutrality. In general, the densities of $Xe^*(met)$ and $Xe^*(res)$ correlated very well with the density of electrons in Period II-1, which meant that they

were generated through direct electron impact reactions. An interesting phenomenon, the so-called “cathode-directed streamer-like” ionization wave, moving to the cathode was observed, in which the peak of atomic ions was ahead of that of the electrons with a speed of $\sim 7,000$ m/s, which was far less than that of a real streamer [Raizer, 1991].

Figures 4-6e and 4-6f present two typical snapshots of important discharge properties at earlier and later times, respectively, of Period II-2. In this period, the applied voltage almost reached its peak and the gap decreased slightly, but the stream-like ionization wave moved to a location very close to the cathode dielectric surface (outer) and stayed almost stationary in Period II-2. The peak value of electrons greatly increased to a level of $\sim 2.7 \times 10^{12} \text{ cm}^{-3}$ at the position of $r=1.22$ cm, while the dominating ion species became Xe_2^+ instead of Xe^+ through the increasingly important three-body ion conversion channel (No. 18 in Table 3-1). Accordingly, this rapidly consumed Xe^+ . In addition, the amount of $\text{Xe}^*(\text{met})$ and $\text{Xe}^*(\text{ex})$ were greatly reduced from values of $4 \times 10^{12} \text{ cm}^{-3}$ and $2.7 \times 10^{12} \text{ cm}^{-3}$, respectively, down to $1.5 \times 10^{12} \text{ cm}^{-3}$ and $5 \times 10^{11} \text{ cm}^{-3}$, respectively, due to the less energetic electrons; this was caused by the reduced electric field due to the shielding by the accumulated ions at the cathode dielectrics (outer); this led to the slight reduction of $\text{Xe}_2^*(^3\Sigma_u^+)$ from $2.5 \times 10^{12} \text{ cm}^{-3}$ to $2 \times 10^{12} \text{ cm}^{-3}$, which was the most

important species for VUV (172 nm) emission, across the gap. After Period II-2, the discharge became more diminished, as described next.

Period III

Figures 4-6g and 4-6h present two typical snapshots of important discharge properties at earlier and later times of Period III, respectively. In this period, the quasi-neutral region expanded slowly from the cathode side (outer) towards the anode side (inner) with greatly decreasing plasma density in the peak (from $8 \times 10^{11} \text{ cm}^{-3}$ to $1.1 \times 10^{11} \text{ cm}^{-3}$) close to the cathode (outer); this was attributed to the decreasing electron temperature caused by the reduced electric field in the sheath on both sides. Especially, the electron temperature in Figure 4-6h was reduced to nearly zero because of the very small electric field in the sheaths. The major species in Period III were electrons and Xe_2^+ , while the other species almost disappeared ($< 10^9 \text{ cm}^{-3}$) and came into a post-breakdown period (extinguished). After Period III, the polarity of the applied voltage changed and the above described pre-breakdown (Period I), breakdown (Period II) and post-breakdown (Period III) repeated temporally with opposite direction and location because of the higher plasma density and more abundant excited species due to the stronger electric field near the inner electrode caused by the small radius of curvature.

4.2.1 Temporal Variation of Discharge Properties

To further elucidate the discharge physics described above, we have presented the temporal variation of other discharge properties together in [Figure 4-7](#), which include: **a)** the applied voltage (V_a), the dielectric voltage (V_d) and the gap voltage (V_g); and **b)** the discharge current density at the inner side ($r=0.8$ cm) and the accumulated charges (Q_a) at both dielectric surfaces ($r=0.8$ and 1.25 cm). Note that the dielectric voltage is defined as the sum of voltages across both quartz tubes. Several important characteristics were drawn from [Figure 4-7](#), as follows. “Memory effects” were clearly seen throughout the cycle. For example, in Period I, the gap voltage led the applied voltage (see [Figure 4-7a](#)) because of the shielding caused by the positive accumulated charges at the anode dielectric surface (inner) remnant from the previous cycle (see [Figure 4-7b](#)). During the breakdown period (Period II), the electrons rapidly accumulated on the inner anode dielectric surface (see [Figure 4-7b](#)), which resulted in a much smaller gap voltage (see [Figure 4-7a](#)) by shielding out the applied voltage. Throughout Period III, the gap voltage was almost zero (see [Figure 4-7a](#)) as the surface charge density remained roughly the same on both dielectric surfaces (see [Figure 4-7b](#)), although the applied voltage was almost as high as 2 kV. In addition, the magnitude of the accumulated surface charge density and current density at the inner dielectric surface was always greater than that at the outer dielectric surface because of the smaller inner area.

Figure 4-8 provides a general view of the discharge across the gap and the exposure view of several important spatial-averaged discharge properties in the first 2 μs , in which the discharge occurred. During the discharge process (Period II), from 0.4 to 1.14 μs , the molecular xenon ions initially outnumbered the atomic xenon ions. The trend did not change until 0.46 μs and lasted through 0.6 μs , in which the discharge occurred. It was also clear that the molecular xenon ions were the dominant ion species at all times, except in the very initial period of the breakdown process, as mentioned above (0.46-0.6 μs). As for the trend of spatial-averaged electron temperature, it was raised to a value of ~ 4 eV prior to when the discharge occurred, and decreased to less than 1 eV right after the discharge process because of the loss of most of the energy via ionizations and excitations. In addition, the amount of Xe^* (met) and $\text{Xe}_2^*(^3\Sigma_u^+)$ both peaked in the early part of the breakdown period (Period II-1), although the latter lagged behind the former by ~ 1 μs .

4.3 General VUV Emission Power and Efficiency

4.3.1 Characteristics of Power Deposition and VUV Emission

Figure 4-9 presents the volumetric power densities of various VUV emission lines and absorption by charged species over a cycle. Figure 4-9a shows that the 172 nm line of VUV was the major source of VUV emission, as compared to the other two lines (147 and 152 nm). The VUV light emission originated from the process whereby

both the excimer species $\text{Xe}_2^*(^1\Sigma_u^+)$ (less dominating) and $\text{Xe}_2^*(^3\Sigma_u^+)$ (most dominating) from an excited state fall to ground state. In addition, the major periods of 172 nm VUV emission occurred in Period II-1 in the first half cycle and in Period V-1 in the second half cycle, which corresponded to when $\text{Xe}^*(\text{met})$ and $\text{Xe}_2^*(^3\Sigma_u^+)$ were most abundant, as shown in Figure 4-8. It was noted that the emitted power of 172 nm was greater in Period II-1 than in Period V-1 because of the “integration effect” of larger circumferential volume near the outer dielectric surface where the intense VUV emission occurred with a smaller value in Period II-1.

Figure 4-9b shows that the volumetric absorbed power was first deposited through the electrons for a very high power density (peak value of 45 Wcm^{-3}) in a very short period of time ($\sim 0.35 \mu\text{s}$) during breakdown Period II-1, then partly through Xe^+ for a low power density (peak value of 12 Wcm^{-3}) in a very short period of time ($\sim 0.35 \mu\text{s}$), and finally through Xe_2^+ for a medium power density (peak value of 18 Wcm^{-3}) for a longer period of time ($\sim 0.4 \mu\text{s}$). Again the electrons absorbed more volumetric power in the first half cycle (Period II) than in the second half cycle (Period V), for a similar reason as mentioned above.

4.3.2 Comparison of VUV Emission Efficiency between Sinusoidal and Distorted Bipolar Square Voltages

Figure 4-10 shows: a) P_{172} and corresponding efficiency of 172 nm VUV as

defined earlier in Eq. (2.19); and b) the power deposition and corresponding fraction in different charged species for the two types of power source (sinusoidal and distorted bipolar square) under the same test conditions ($p=400$ torr; $f=50$ kHz; $d=4.5$ mm). Note that P_{172} is defined as the total VUV emission power as referred in Eq.(2.18). Figure 4-10a shows that the emitted power density for 172 nm using distorted bipolar square voltages increased 2.5 times (from 49.2 to 124.8 W) more than when using idealistic sinusoidal voltages, while the corresponding efficiency increased from 13.4% to 28.9%. Figure 4-10b clearly shows that the fraction of power deposition through the electrons using distorted bipolar square voltages was nearly 2 times greater (22.7% to 43.5%) than when using idealistic sinusoidal voltages. In other words, the fraction of total power deposition through the two types of ions decreased from 76.9% (sinusoidal case) to 56.5% (distorted bipolar square case). Note that this dramatic increase of power deposition through the electrons was responsible for the large increase of the 172 nm VUV emission, as found in Figure 4-10a, in which the energetic electrons efficiently excited the ground-state xenon and generated much more abundant excimers to emit 172 nm VUV photons.

To further understand the reason for the increase in VUV emission using distorted bipolar square voltages as compared to idealistic sinusoidal voltages, phase diagrams of 172 nm VUV emission power distribution for both cases are shown in

Figure 4-11. The results show that VUV emission occurred much earlier, with greater intensity and more uniformity across the whole gap during the discharge process in the former case. This was attributed to the rapidly rising voltage of the distorted bipolar square voltages and thus, higher energy absorption efficiency by the electrons, which then generated abundant $\text{Xe}^*(\text{met})$ and, thus $\text{Xe}_2^*(^3\Sigma_u^+)$ for the 172 nm VUV photon emission.

Figure 4-12 shows the temporal variation of power deposition through the charged species along with the gap voltage of the sinusoidal case. It was found, for example, that in the first half cycle (Period II-1), the electron power deposition of distorted bipolar square voltages was much higher than that of the sinusoidal ones (see bottom of Figure 4-9) (45 Wcm^{-3} vs. 13 Wcm^{-3}) because of the much larger $|dV_g/dt|$ (~ 3.8 times) in the pre-breakdown period. The larger value of $|dV_g/dt|$ represented the shorter period prior to the breakdown gap voltage ($\sim 2.4 \text{ kV}$), during which only the electrons could respond instantly (almost without inertia) and gain energy from the field efficiently without much elastic collision loss. This is shown in Figure 4-13, in which the electrons gain energy through ohmic heating and lose energy mostly through inelastic collisions, especially the excitations of ground-state xenon (No. 4 and 5 in Table 3-1). In the case of distorted bipolar square voltages, the electron temperature in Period I increased up to $\sim 4 \text{ eV}$ (see Figure 4-8), while it only

reached 2-3 eV in the case of sinusoidal voltages (not shown here). This also explained why the atomic xenon ions absorbed the energy with some phase lag, as compared to the electrons, because of the inertia effects in both cases. As for the power deposition through Xe_2^+ , it was still quite appreciable and extended for a relatively long period, even in the post-breakdown period for the sinusoidal case; this was caused by non-vanishing gap voltages in this period which were beneficial for the power absorption of Xe_2^+ , unlike the nearly vanishing gap voltage in the same period for the case of distorted bipolar square voltages.

In addition, Table 4-1 shows the amount of power output from the sinusoidal voltages ($P_{p,\text{sin.}}$) and the distorted bipolar square voltages from power supply ($P_{p,\text{dis.}}$) is 1909.9 (W) and 1860.473 (W) respectively. From Table 4-1, the power conversion efficiency (P_{172}/P_p) of the distorted bipolar square voltages (6.7%) is much better than the sinusoidal voltages (2.57%).

4.4 Brief Summary of This Chapter

Major findings of this chapter are summarized briefly as follows:

1. The insight of plasma physics and chemistry of a homogeneous coaxial xenon excimer ultraviolet lamp driven by sinusoidal and distorted bipolar square voltages have been described. According to the temporal variation of electron number density, the cycle can be divided into six periods. The periods I and IV

are pre-breakdown regions, the periods II and V are breakdown regions and the periods III and VI are post-breakdown regions. In period II and V, it can be further divided into two sub-periods (II-1 and II-2; V-1 and V-2). We have described the phenomenon in each period in this chapter.

2. Comparison of VUV emission efficiency between sinusoidal and distorted sinusoidal voltages has been made in detail. The results show that the efficiency of VUV emission using distorted bipolar square voltages is much higher than that using sinusoidal voltages (28.9% vs. 13.4%). This is attributed to the two following mechanisms. The first is the greater rate of voltage increase in bipolar square voltages as compared to that of sinusoidal voltages, which allows only the electrons to efficiently absorb the power in a short period of time without much elastic collision loss. The second is the comparably smaller amount of “wasted” power deposition by Xe_2^+ in the post-breakdown period.

Chapter 5

Parametric Study of VUV Emission from a Homogeneous Coaxial Xenon Excimer Ultraviolet Lamp Driven by Distorted Bipolar Square Voltages

In this chapter, an extensive parametric study of VUV emission from a homogeneous coaxial xenon excimer ultraviolet lamp driven by distorted bipolar square voltages is described. First, we summarize a typical characteristic of power deposition and VUV emission based earlier results presented in Chapter 4. Second, a set of simulation conditions are described. Third, results by varying power frequency, background gas pressure, gap distance are number of dielectric layers are described one by one. Finally, major findings of the parametric study are summarized briefly at the end of this chapter.

5.1 Typical Characteristics of Power Deposition and VUV

Emission

Figure 5-1 shows the cycle averaged data of VUV emission (upper figure) and power deposition of charged species (bottom figure) across the discharge gap over a cycle. It can be found that 172 nm line of VUV is the major source of VUV emission

as compared to the other two lines (147 and 152 nm). It can also be noted that the strength of VUV power emission in the inner side is larger than that in the outer side because the electric field in the inner side is stronger than in the outer side. In the bottom figure, it can be found that electron power deposition occurs mainly across the discharge gap and ion power deposition occurs mainly in the sheath region. In addition, the amount of ion power deposition density in the inner side is nearly 1.67 times higher than in the outer side. The reason is the same as the variation of VUV power emission because of larger electric field in the inner side with the characteristic due to smaller radius of curvature. The trend of 172 nm line of VUV power emission (top) is similar to that of electron power emission (bottom) because, through the collision of energetic electrons, more species $\text{Xe}^*(\text{met})$ and $\text{Xe}_2^*(^3\Sigma_u^+)$ are generated, leading to 172 nm radiation.

Figure 5-2 shows the phase diagrams of VUV power emission ($\lambda=172\text{nm}$) (upper figure) and electron power deposition (bottom figure) over a cycle, while Figure 5-3 shows the phase diagrams of ion power deposition (Xe^+ in the upper and Xe_2^+ in the bottom figure). Again, we only describe the variations of power deposition and VUV radiation in the first half cycle (I, II and III) in detail. Besides, the slightly difference of the amount of the above properties results from the different areas of the inner and outer electrodes.

Period I

In the earlier part of Period I (negative applied voltage, 19.57-20 μs in both [Figures 5-2 and 5-3](#)), it can be found that electrons responded to the variations of electric field immediately, which leads to increasing electron power deposition in the region of $r=0.95\text{-}1.05$ cm. Accordingly, the concentrations of metastable and excimer species start to increase in the region of $r=0.95\text{-}1.05$ cm (see top and middle of [Figure 4-5](#)) due to electron impact collisions. Thus, power emission of 172 nm line also increases with the increasing of concentrations of metastable and excimer species. Generally, power deposition of Xe^+ is less than the order of 10^{-2} (Wcm^{-3}) although number density of Xe^+ increases up to 10^5 (cm^{-3}) (see [Figure 4-4](#)). At the same time, power deposition of Xe_2^+ mainly occurs in the outer sheath region.

In the later part of Period I (positive applied voltage, 0-0.25 μs in both [Figures 5-2 and 5-3](#)), energetic electrons, moving from the outer sheath into the bulk ($r\approx 0.95\text{-}1.05$ cm), generates many excited species such as Xe^* (met) and $\text{Xe}_2^*(^3\Sigma_u^+)$ in the bulk (see [Figure 4-5](#)). VUV emission thus rises to the order of 1 (Wcm^{-3}). The concentration of Xe^+ increases up to $\sim 10^6$ (cm^{-3}), as a result of direct impact ionization, as shown in the middle of [Figure 4-4](#). However, the power deposition of Xe^+ is still less than the order of 10^{-2} (Wcm^{-3}) because the number density of Xe^+ is too small in this period (see middle of [Figure 4-4](#)). In contrast, the power deposition

of Xe_2^+ is much higher than the order of $1 \text{ (Wcm}^{-3}\text{)}$ because very large amount of Xe_2^+ exists in this region and large electric field in the outer sheath. Near the outer dielectric tube (cathode side), although the electric field is very high due to the rising voltage at the inner electrode, both VUV power emission and electron power deposition are weak because of very few $\text{Xe}^*(\text{met})$, $\text{Xe}_2^*(^3\Sigma_u^+)$ and electrons (see [Figures 4-4 and 4-5](#)) in this region. Thus, it can be observed that the major power deposition of Xe_2^+ is in the region of $r \approx 0.83\text{-}0.94 \text{ cm}$ in the sheath where a large potential drop exists.

Period II

In Period II-1, electron power deposition increases dramatically and the peak moves towards outer quartz tube in a speed of $\sim 7,000 \text{ m/s}$ (from anode towards cathode, see bottom of [Figure 5](#)) due to the huge growth of electron number density by direct electron impact ionization (see top of [Figure 4-4](#)). The amount of electron power deposition rapidly increases to the maximal value ($> 1 \times 10^3 \text{ Wcm}^{-3}$) within $\sim 0.388 \mu\text{s}$ at $r \approx 1.06 \text{ cm}$ and then decreases gradually afterwards (see bottom of [Figure 5-2](#)). The moving direction of Xe^+ power deposition is the same as the electrons, with the maximal value of $7 \times 10^2 \text{ (Wcm}^{-3}\text{)}$ located at $r \approx 1.22 \text{ cm}$, which is smaller than that of the electrons due to its heavier mass. Afterwards, the power deposition Xe^+ decreases gradually in Period II-2 (see top of [Figure 5-3](#)). At the same time, number

of Xe_2^+ increases through the three-body ion conversion channel (No. 18 in [Table 3-1](#)), and thus Xe_2^+ power deposition increases towards the cathode (see bottom of [Figure 5-3](#)). However, the power deposition of Xe_2^+ is smaller than that of Xe^+ because the former is about two times heavier than the latter. In addition, both $\text{Xe}^*(\text{met})$ and $\text{Xe}_2^*(^3\Sigma_u^+)$ are both highly abundant across the gap (see [Figure 4-5](#)) because of the excitation of ground-state xenon (No. 3 and 5 in [Table 3-1](#)) by the collision of energetic electrons. During this period, the 172 nm VUV power emission (see top of [Figure 5-2](#)) originates from the process that both the excimer species $\text{Xe}_2^*(^1\Sigma_u^+)$ (less dominating) and $\text{Xe}_2^*(^3\Sigma_u^+)$ (most dominating) fall to the ground state (No. 19 and 20 in [Table 3-1](#)).

In Period II-2, both $\text{Xe}^*(\text{met})$ and $\text{Xe}_2^*(^3\Sigma_u^+)$ begin to disappear because of less energetic electrons existing in the bulk region ($r \approx 1.1\text{-}1.2$ cm; see bottom of [Figure 4-4](#)), which in turn reduces the VUV emission (P_{172}) dramatically (see top of [Figure 5-2](#)). In the cathode sheath region, highly depleted electrons (see top of [Figure 4-4](#)) can not absorb enough energy from the electric field which leads to much less power deposition of electrons (bottom of [Figure 5-2](#)). At the same time, Xe^+ is rapidly consumed by Xe_2^+ through the three-body collision as described earlier. Thus, the power deposition of Xe_2^+ is much larger than that of Xe^+ as can be clearly seen in the cathode sheath ([Figure 5-3](#)). Noticeably, the maximal value of Xe_2^+ power

deposition can reach a value of 4×10^2 (Wcm^{-3}) in the cathode sheath region.

Period III

In this post-breakdown period, the VUV emission decays with time in the bulk region, which strongly correlates with the variation of number densities of both Xe^* (met) and $\text{Xe}_2^*(^3\Sigma_u^+)$, as shown in [Figure 4-5](#) and top of [Figure 5-2](#). In addition, power deposition to charged particles mainly goes through the Xe_2^+ remaining in the cathode sheath throughout Period III (see bottom of [Figure 5-3](#)). Note the power deposition in the bulk region with much more Xe_2^+ is much smaller as compared to that in the cathode sheath mainly because of much smaller electric field in this region.

5.2 Simulation Conditions

Four parameters, which include driving frequency of the power source, background gas pressure, gap distance between electrodes and number of dielectric layers, are varied systematically to study their effects on the efficiency of 172 nm line (η_{172}), the total power deposition (P_{tot}) and the VUV emission from 172 line (P_{172}).

The test conditions are summarized in [Table 5-1](#).

5.3 Effect of Frequency Variation

[Figure 5-4a](#) shows that η_{172} , P_{tot} and P_{172} all increase with increasing frequency in the range of 10-100 kHz under the condition of 400 torr (pressure), 4.5 mm (gap distance) and 2 dielectric layers. Interestingly, the efficiency η_{172} increases only

slightly from 24.4% (10 kHz) to 31.4% (100 kHz), while total emission power increased dramatically from 102.9 W (10 kHz) to 781.4 W (100 kHz). Corresponding total absorption powers are plotted in [Figure 5-4b](#), which shows that the energy absorbed by the electrons increases almost 10 times with 10 times of frequency increase (37 to 370 W vs. 10 to 100 kHz), while the energy absorbed by the ions (especially the Xe_2^+) began to level off with increasing frequency. This means that only the very light electrons could efficiently absorb the energy from the oscillating electric field, while the much heavier ions could not because of very large inertia. Albeit the P_{Xe^+} (11.9 (W) to 182.1 (W)) and the $P_{\text{Xe}_2^+}$ (52.9 (W) to 213.1 (W)) increased with increasing frequency (10-100 kHz), the fraction of P_{Xe^+} (11.6% to 23.3%) increases and $P_{\text{Xe}_2^+}$ (51.2% to 29.57%) decreases with increasing frequency, as shown in [Figure 5-4c](#). In addition, the slight increase of VUV emission efficiency ([Figure 5-4a](#)) with increasing frequency is attributed to the increasing fraction of power deposition through the electrons as compared to the heavy Xe_2^+ ([Figure 5-4c](#)), in which the electrons are able to excite more VUV emission species such as Xe^* (met) and $\text{Xe}_2^*(^3\Sigma_u^+)$.

In [Figure 5-4b](#) and [Figure 5-4c](#), they show that most of the energy is absorbed by the heavier Xe_2^+ , while only a smaller fraction is absorbed by the electrons and even much smaller fraction by the Xe^+ at lower frequencies (<50 kHz). In contrast,

most of the energy is absorbed by the electrons at higher frequencies (>50 kHz), while the fraction of energy absorbed by the Xe_2^+ becomes much smaller. In addition, we can find that the fraction of energy absorbed by the electrons over a cycle increases slightly (37-47%) with increasing frequency, but that of the heavier ions (Xe_2^+) decreases quickly (52-30%) with increasing frequency. The larger the value of $|dV/dt|$ is (at higher frequency), the easier the electrons as compared to other ions could absorb energy per unit time since only they could respond instantly (almost without inertia) to gain energy from the oscillating electric field efficiently without much elastic and inelastic collision loss (No. 7 in Table 3-1).

Based on the above observation, we can simply conclude that more power deposited through the electrons benefits the absolute VUV emission power and corresponding efficiency.

5.4 Effect of Background Gas Pressure Variation

Figure 5-5a shows that η_{172} , P_{172} and P_{tot} at various gas pressures under the condition of 50 kHz (frequency), 4.5 mm (gap distance) and 2 dielectric layers. Results show that η_{172} increases from 7.9% to 39.4% as background gas pressure increases from 100 torr to 700 torr, while both P_{172} and P_{tot} have peak values of 320 W and 475 W, respectively, at 600 torr. Reason causing this observation will be explained later. Figure 5-5b shows the partition of power deposition through different

types of charged species at various gas pressures. Fraction of the power deposition for different charged species changes at different pressures, which can be also seen from [Figure 5-5c](#) (ratios of absorbed to total power for different charged species). Results show that power absorbed through the electrons increases with almost linearly with increasing pressure, but reaches a peak value of ~260 W at a pressure of 600 torr. Furthermore, power absorbed through the Xe_2^+ increases with gas pressure, but levels off very soon at ~160 W at pressures of 300-400 torr. In addition, power absorbed through Xe^+ decreases with increasing gas pressure and monotonically reaches a value as low as ~25 W at 700 torr. This is attributed to more intense three-body ion conversion reaction (No. 18 in [Table 3-1](#)) at higher pressures. Equivalently, at lower pressures, power is mostly absorbed through the Xe^+ in the cathode sheath, at which the very few Xe_2^+ exists. At higher pressures, the power deposition through the electrons becomes the dominant process, while that through Xe^+ becomes less important because most of them disappear through the intense three-body ion conversion reaction as mentioned earlier.

[Figures 5-6\(a\)-\(c\)](#) show the cycle averaged power distribution in the discharge space for electrons, Xe^+ and Xe_2^+ , respectively. [Figure 5-6a](#) (very similar to the P_e curve in the bottom of [Figure 5-1](#)) shows that P_e generally increases everywhere in the gap with increasing pressure, except near the pressures of 600-700 torr, as similarly

shown in [Figure 5-5b](#). The reason should be attributed to the increasingly frequent elastic collision loss near the pressures of 600-700 torr. On the contrary, [Figure 5-6b](#) shows that P_{Xe^+} in the sheaths generally decreases with increasing pressure monotonically, as similarly shown in [Figure 5-5b](#). However, [Figure 5-6c](#) shows that $P_{Xe_2^+}$ in the both sheaths increase with increasing pressure first (prior to 300-400 torr) and then become essentially the same or even decrease slightly afterwards. The latter is attributed to the smaller speed of the Xe_2^+ when accelerating in the sheaths due to increasing background gas pressure, although the Xe_2^+ becomes more abundant.

5.5 Effect of Gap Distance Variation

[Figure 5-7a](#) shows that η_{172} , P_{tot} and P_{172} are plotted as a function of gap distance under the condition of 50 kHz (frequency), 400 torr (pressure) and 2 dielectric layers. Results show that η_{172} increases from 6% to 30% as the gap distance increases from 0.5 mm to 5 mm. [Figure 5-7b](#) shows the partition of power deposition through different types of charged species at various gap distances. Fractions of the power deposition for different charged species change at different gap distances, which can be also seen from [Figure 5-7c](#) (ratios of absorbed to total power for different charged species). Results show that power absorbed through the electrons increases with increasing gap distance and can reach a value of ~240 W at $d=5$ mm. Furthermore, power absorbed through the Xe_2^+ increases with gas distance rapidly

initially ($d \leq 1$ mm), but reaches a peak value of ~ 175 W between $d=2$ and 3 mm and then decreases slightly with increasing gap distance. In addition, power absorbed through Xe^+ increased slightly with increasing gas pressure monotonically reaching a value of ~ 75 W at $d=5$ mm. In brief summary (see [Figure 5-7c](#)), the larger the gap distance is the larger the fraction of power is absorbed by the electrons (48% at $d=5$ mm), the less power absorbed by the Xe_2^+ (35% at $d=5$ mm) and approximately the same power absorbed by the Xe^+ (16% at $d=5$ mm). In other words, increasing gap distance is beneficial to VUV emission because of the increasing electron power absorption (12.5% to 47.7%) and the reduced ion power absorption (87.5% to 52.3%).

[Figure 5-8a](#) and [Figure 5-8b](#) show the spatial distributions of cycle averaged VUV emission and power deposition through electrons and ions across the gap, respectively. It can be found spatial distribution of power density P_{172} correlates very well with that of power density of P_e . Also, the peak value of power density of P_{172} in the bulk region (near the sheath edge) remains approximately the same for all different gap distances ([Figure 5-8a](#)). Similar trends are also observed for power density of P_e ([Figure 5-8b](#)). It is thus clear that the increase of P_{172} as well as P_e with increasing gap distance, as shown in [Figure 5-7](#), is attributed to the “volumetric integral” effect in the larger outer cathode and wider bulk region. Interestingly, [Figure 5-8b](#) shows that the power density absorbed through ions ($P_{\text{Xe}^+} + P_{\text{Xe}_2^+}$) in the

outer sheath decreases with increasing gap distance because of reduced applied electric field, while the power densities absorbed through ions in the inner sheath remains approximately the same. However, the total powers absorbed through ions remain approximately the same at different gap distances, as shown earlier in [Figure 5-7b](#), also because of the “volumetric integral” effect as mentioned in the above. One exception is the case with a gap distance of 0.5 mm, which the plasma is a typical Townsend-like discharge that there are much fewer electrons than the ions across the gap in general, in which the details of the discharge are not described here.

5.6 Effect of Varying the Number of Dielectric Layers

[Figure 5-9a](#) shows that the values of η_{172} , P_{tot} and P_{172} for the cases with one- and two-dielectric layers, while [Figure 5-9b](#) shows the corresponding power partitions among different charged species. It is clearly that all η_{172} , P_{tot} and P_{172} of the two-dielectric case are larger than those of one-dielectric one. P_e increases from a value of 188 W in the two-dielectric case is up to 637.3 W in the one-dielectric case, which results in the increase of P_{172} from 122.3 W to 453.3 W. However, the growth of $P_{\text{ion}} (= P_{\text{Xe}^+} + P_{\text{Xe}_2^+})$ from 244.2 W in the two-dielectric case to 719.3 W in one-dielectric case results in more wasted power in ion heating, although the increase of η_{172} can increase from 28.9% to 33.5%. Interestingly, [Figure 5-9c](#) shows the power partitioning in P_{tot} for the one- and two-dielectric cases remains approximately

the same.

Figure 5-10a and Figure 5-10b show the spatial distributions of cycle averaged electric field and power deposition through charged species across the gap, respectively, for the one- and two-dielectric cases. Figure 5-10a shows that electric field at the inner side for the one-dielectric case is 1.33 times larger than that for the two-dielectric one. This is caused by the fact that the applied voltage in the one-dielectric case can be directly applied to the discharge without the shielding of accumulated charged species at the dielectric surface if there is dielectric layer at the inner side. This is reflected in the ultra high value of power density absorbed through ions at the inner sheath, as shown in Figure 5-10b. However, use of one-dielectric in the xenon DBD may have other negative side effects. For example, inner electrode surface may be quickly eroded by the bombarding of highly energetic ions because of this very large electric field. Thus, two dielectric layers are generally used in practice.

5.7 Brief Summary of This Chapter

Major findings of this study in this chapter are summarized as follows:

1. The results show that electron power deposition occurs mainly in the early portion of breakdown period (period II-1 and V-1) in which the VUV emission is most intense, while Xe^+ and Xe_2^+ power depositions occur in the whole breakdown period (period II and V) and later part of breakdown period (period

II-2 and V-2), respectively, for both the cases of sinusoidal and distorted voltages.

2. An extensive parametric study of the VUV emission (172 nm) from the homogeneous coaxial excimer xenon lamp by varying the four key parameters (frequency, pressure, gap distance and number of dielectric) has been investigated. The results show that: 1) the VUV emission increases almost linearly with increasing driving frequency, but corresponding emission efficiency remains nearly unchanged; 2) a maximal value of VUV emission exists at 600 torr; 3) the magnitude of VUV emission increases with increasing gap distance and 4) the magnitude of VUV emission in the case of one-dielectric case is larger than two-dielectric, although the inner electrode surface may be quickly eroded by the bombarding of highly energetic ions because of the very large electric field.

Chapter 6

Effect of Gas Heating on VUV Emission from a Homogeneous Coaxial Xenon Excimer Ultraviolet Lamp Driven by Distorted Bipolar Square Voltages

As mentioned in the earlier Section 1.3.3, most studies of gas heating effect on gas discharges focused on low-pressure ones. Also recently we have observed experimentally [Lu, 2008] that VUV emission illuminance peaks at about 400 torr of background xenon gas and the discharge could not even sustain with a pressure larger than 440 torr. In this chapter, we intend to explain this experimental observation by including the gas effect into the one-dimensional fluid modeling as presented earlier. We first present the heat conduction equation which is included in the modeling, followed by the description of simulation conditions, and then the results are presented and discussed. Finally, major findings of the chapter are summarized at the end of this chapter.

6.1 Heat Conduction Equation

To model the gas heating effect without considering convective buoyancy effect, a heat conduction equation is added to couple with the fluid modeling equations. For

radial one-dimensional case, the heat conduction equation can be written as

$$\frac{\partial}{\partial r} \left(k \frac{\partial T_g}{\partial r} \right) + P(r) = 0 \quad (6.1)$$

where k is the thermal conductivity of background xenon gas, which is generally a function of gas temperature T_g [Hanley, 1973] and $P(r)$ is a summation of ion power absorption through ion Ohmic heating and the elastic collision energy loss of electrons with background gas. Note the electron energy loss due to elastic collision is often ignored in a low-pressure discharge; however, it is important in a nearly atmospheric-pressure discharge like the xenon excimer discharge.

To obtain the spatial distribution of ionization rate we need to know the spatial distribution of background gas density, which is not uniform because of gas heating. In the current study, we can obtain this important information through the coupling solution of the ideal gas law, uniform pressure distribution and conservation of mass in the radial direction. Firstly, uniform background gas pressure distribution is assumed since no convective flow along the radial direction, which leads to $n_g(r)T_g(r) = \text{constant}$ regardless of the radial position. Secondly, conservation of mass holds in the radial position since the lamp is a close system without any flow in and out during operation, which leads to $\iiint_{\text{lamp}} n_g(r) dV = 2\pi \int_{r_i}^{r_0} n_g(r) r dr = N_b$, where r_i (=8 mm) and r_0 (=12.5 mm) is the inner and outer radii of the lamp, respectively, and N_b is the total number of molecules of the background gas that be directly be obtained

from the initial condition before turning on the power supply of the lamp.

6.2 Simulation Conditions

Employed xenon plasma chemistry and lamp configuration are the same as those in Chapter 3 except the discharge gap ($=r_0-r_i$) is changed to be 4.5 mm ($r_i=0.8$ mm, $r_0=1.25$ mm) for the purpose of comparison with experimental data as described later.

Radial one-dimensional computational domain extends from $r=0$ through r_0 . The temperature at the outer electrode ($r=r_0$) is fixed ($=473$ °K) based on the measurements [Lu, 2008] and the Neumann type boundary condition is employed at the axis ($r=0$) because of symmetry. The frequency f of the pulsed-voltage power supply is fixed at 60 kHz and the xenon gas pressure p is in the range of 100-700 torr throughout the study.

6.3 Results and Discussion

Figure 6-1 shows the simulation data of P_{172} (power emission of 172 nm line) and the measured illuminance under the near atmospheric-pressure condition in the range of 100-800 torr. Note that the direct comparison is difficult because of the fast decay of 172 nm VUV in space under the near atmospheric-pressure condition in the measurement and the simplified geometry employed in the current simulation. Experimental results show that the discharge cannot even sustain if the gas pressure is larger than 440 torr. The simulations without consideration of gas heating show that

P_{172} levels off as the gas pressure exceeds 600 torr and the discharge extinguishes as the gas pressure is approximately 800 torr. The results also show that P_{172} are essentially the same as pressure is less than 500 torr for both the cases with and without consideration of gas heating in the simulations. However, the simulations show that, by including gas heating effect, P_{172} begins to decrease rapidly at $p=500$ torr and the discharge extinguishes as p^3 513 torr. These observations show that by considering gas heating effect in the fluid modeling we can explain reasonably the extinguishment of the xenon discharge as the pressure exceeds some threshold. Two mechanisms about the extinguishment of the xenon discharge are explained in detail next.

Figure 6-2 shows spatial distributions of xenon gas temperature across the discharge gap at various gas pressures. In the inner sheath region, the gas temperature is much higher than that in the bulk region and can reach up to 640°K at the inner dielectric tube surface. Dramatic increase of gas temperature in this region is mainly caused by the large ionic Ohmic heating due to large electric field in the sheath, in which the Ohmic heating contributes most to the gas heating that is clearly shown in Figure 6-3. In addition, distributions of gas temperature in this sheath region are essentially the same at various background pressures. In the inner pre-sheath region ($r \approx 0.854-0.91$ cm), the variation of gas temperature is slightly higher than that in the

bulk region. Although the influence of ionic Ohmic heating weakens in this region, the influence of energy loss of electron elastic collision with background natural gas becomes important in this region (see [Figure 6-3](#)). In the bulk region ($r \approx 0.86-1.22$ cm), the gas temperature increases with increasing pressure mostly through absorbing the energy loss of electron elastic collision with background natural gas, as can be clearly shown in [Figure 6-3](#). However, the increase rate of gas temperature with increasing background pressure jumps dramatically from 500 to 510 torr, which means that the gas heating is pronounced near this pressure.

Under the same gas heating source, [Figure 6-4](#) shows the spatial distributions of xenon gas temperature with constant thermal conductivity across the discharge gap at various gas pressures. Interestingly, we have found opposite gas temperature distribution in the bulk region at various pressures. T_g is maximum in the bulk region at 100 torr if $k=\text{const}$ due to the high variation of T_g in the sheath region. On the contrary, T_g is minimum in the bulk region at the case of 100 torr if $k=f(T_g)$. Thus, thermal conductivity plays an important role in determining the temperature distribution. [Figure 6-5](#) shows the variation of thermal conductivity in the region of $T_g = 400 - 700$ K as $k=f(T_g)$. The value of thermal conductivity increases from 0.007 to 0.012 (W/mK) with increasing gas temperature. When the value of thermal conductivity becomes larger, more heating source can be taken away from the outer

lamp tube to suppress the rise of gas temperature. Thus, at 100 torr as $k=f(T_g)$, the increase of T_g in the outer sheath is lower than that as $k=const$. The effect of gas heating with $k=f(T_g)$ in the bulk region increases with increasing background pressure.

Figure 6-6 shows the distribution of T_g at $r=1$ cm in the range of 100 – 513 torr. Gas temperature rises from 496 to 531 (K) with increasing pressure. After reaching $p=510$ torr, the bulk temperatures are almost the same. When the gas pressure exceeds 513 torr, discharge can not sustain, which the reason will be explained in the next few paragraphs.

Figure 6-7 shows spatial distributions of gas temperature and number density across the discharge gap at 510 torr along with a horizontal line showing the gas number density that is the case without considering gas heating effect. It shows that the gas number density increases from the inner to the outer side in the gap because of the assumption of constant pressure inside the gap. The increase of background gas number density at the outer portion ($> \sim 0.95$ cm) enhances the three-body ion conversion from Xe^+ to Xe_2^+ (No. 18 in Table 3-1), which further promotes the recombination reaction of Xe_2^+ and electrons that destroys electrons rapidly (No. 7 in Table 3-1). This can be further explained in more detail next.

Figure 6-8 shows the comparison of spatial averaged distributions of charged

species within the pre-breakdown and breakdown periods at 510 torr between the cases with gas heating and without gas heating. It clearly shows that both the number densities of electron and Xe_2^+ without gas heating are much larger than those with gas heating. Also there is almost no phase delay between the rising electron and Xe_2^+ number densities with gas heating during the breakdown period. Unlike the case without gas heating the abundant Xe_2^+ promotes the reaction of $e-\text{Xe}_2^+$ recombination, which eventually extinguishes the discharge. This can be demonstrated more clearly in [Figure 6-9](#), which shows the comparison of cycle-averaged distributions of the source terms of $e-\text{Xe}_2^+$ recombination and Xe^+ -to- Xe_2^+ ion conversion, respectively. It shows that the source terms of the above two reaction channels are more pronounced in the region of $r \approx 1-1.15$ cm where the gas breakdown occurs in the first half cycle.

[Figure 6-10](#) presents the spatial averaged distributions of electron temperature (T_e) and electron number density (n_e) over a cycle in the range of 100-510 torr. It shows that the averaged electron temperature decreases with increasing xenon gas pressure because of electron energy loss due to elastic collision with background gas. In the breakdown period where the electron number density rises up very rapidly, the averaged electron number density reach a maximum value at 500 torr and then becomes approximately the same with further increase of pressure. This leads to the existence of maximum electron power absorption at 500 torr as shown in [Figure 6-11](#),

mainly because of the increasing electron energy loss due to elastic collision with background xenon atoms (Figure 6-12). From Figure 6-11 and 6-12, we can find the proportion of electron energy loss due to elastic collision in electron power absorption increases with increasing pressure, especially at 510 torr. As the background pressure exceeds 510 torr, fewer electrons as well as less electron energy can be utilized for the ionization which leads to the extinguishment of the xenon discharge as found in the current study.

6.4 Brief Summary of This Chapter

Major findings of this study in this chapter are summarized briefly as follows:

1. The simulations show that by including gas heating P_{172} begins to decrease rapidly at $p= 500$ torr and extinguishes as $p> 513$ torr. These observations show that by considering gas heating in the fluid modeling one can explain reasonably the observed extinguishment of the xenon discharge as the pressure exceeds some threshold as found in the experiments.
2. The major mechanisms of the above phenomena are described as follows: 1) Increasing pressure leads to higher gas heating because of increasing electron energy loss through the elastic collision with xenon atoms in the bulk region; and 2) The above leads to higher gas density at outer region of the gap ($r\approx 1.1\sim 1.16$ cm), because of heat conduction and uniform pressure distribution, as compared

to the case without gas heating which promotes the three-body Xe^+ -to- Xe_2^+ ion conversion and $e-Xe_2^+$ recombination that greatly reduces the plasma density as pressure exceeds some threshold.



Chapter 7

Conclusion and Recommendations of Future Work

In this chapter, we first present the major findings in this thesis and then followed by the recommendations of future work in the research of xenon excimer discharges.

7.1 Conclusion

7.1.1 Enhancement of VUV Emission from a Coaxial Xenon Excimer Ultraviolet Lamp Driven by Distorted Bipolar Square Voltages

In this study, enhancement of vacuum UV emission from a coaxial xenon excimer UV lamp (EUV) driven by 50 kHz distorted bipolar square voltages has been investigated numerically. A self-consistent radial one-dimensional fluid model, taking into consideration non-local electron energy balance, was employed to simulate the complicated discharge physics and chemistry. The discharge was divided into two portions of three breakdown periods, which included the pre-breakdown, the breakdown (most intense 172 nm VUV emission) and the post-breakdown periods. An interesting “cathode-directed streamer-like” ionization wave, having atomic xenon ions at the head and the electrons at the tail, was found to move at a speed of $\sim 7,000$

m/s in the early part of the breakdown period (Period II-1).

The results show that the efficiency of VUV emission using distorted bipolar square voltages was much higher than that one using sinusoidal voltages (28.9% vs. 13.4%). This was attributed to the two following two mechanisms. The first was the greater rate of voltage increase in bipolar square voltages as compared to sinusoidal voltages, which allowed only electrons to efficiently absorb the power in a short period of time without much elastic collision loss. Energetic electrons then generated higher amounts of excimer (and also metastable) xenon with more uniform distribution across the gap for a longer period of time during the breakdown process. The second was the comparably smaller amount of “wasted” power deposition by Xe_2^+ in the post-breakdown period driven by distorted bipolar square voltages because of the nearly vanishing gap voltage, which was caused by the shielding effect due to the accumulated charges on both dielectric surfaces.

7.1.2 A Parametric Study of VUV Emission from a Coaxial Xenon Excimer Ultraviolet Lamp Driven by Distorted Bipolar Square Voltages

In this study, the detailed process of VUV emission and power deposition of charged species for a coaxial excimer xenon lamp driven by 50 kHz distorted bipolar square voltages has been investigated numerically. A self-consistent radial

one-dimensional fluid model considering local mean energy approximation is employed to simulate the complicated discharge physics and chemistry. The process is divided into two portions of three breakdown periods, which include the pre-breakdown, the breakdown (most intense 172 nm VUV emission) and the post-breakdown periods. The results show that electron power deposition occurs mainly in the early portion of breakdown period (period II-1 and V-1) in which the VUV emission is most intense, while Xe^+ and Xe_2^+ power depositions occur in the whole breakdown period (period II and V) and later part of breakdown period (period II-2 and V-2), respectively.

Extensive parametric study of the VUV emission (172 nm) from the same excimer xenon lamp by varying the four key parameters (frequency, pressure, gap distance and number of dielectric) has also been investigated. The results show that: 1) the effect of varying frequency is minimal; 2) a maximal value of VUV emission exists at 600 torr; 3) VUV emission increases with increasing gap distance and 4) the value of VUV emission in the case of one-dielectric case is better than two-dielectric, although inner electrode surface may be quickly eroded by the bombarding of highly energetic ions because of the very large electric field.

7.1.3 Effect of Gas Heating on VUV Emission from a Coaxial Xenon Excimer Ultraviolet Lamp Driven by Distorted Bipolar Square

Voltages

In this study, the gas heating effect in a homogeneous coaxial xenon excimer UV discharge (EUV) driven by 50 kHz distorted bipolar square voltages has been investigated numerically. A self-consistent radial one-dimensional fluid model, taking into consideration non-local electron energy balance, was employed to simulate the condition with and without gas heating effect. The results show that by including gas heating in the fluid modeling one can explain reasonably well the experimentally observed VUV emission at various background pressures, especially the extinguishment of the discharge as pressure exceeds some threshold value.

The major mechanisms of the above phenomena are described as follows: 1) Increasing pressure leads to higher gas heating because of increasing electron energy loss through the elastic collision with xenon atoms in the bulk region; and 2) The above leads to higher gas density at outer region of the gap ($r \approx 1.1 \sim 1.16$ cm), because of heat conduction and uniform pressure distribution, as compared to the case without gas heating which promotes the three-body Xe^+ -to- Xe_2^+ ion conversion and $e\text{-Xe}_2^+$ recombination that greatly reduces the plasma density as pressure exceeds some threshold.

7.2 Recommendation of Future Work

To further understand the plasma physics and chemistry inside a practical xenon

excimer lamp, recommendations of possible future work are summarized as follows:

1. The study of gas heating due to ion bombardment on the inner dielectric layer, in addition to the electron energy loss due to elastic collision in the bulk region and ionic ohmic heating in the inner sheath region.
2. It has been observed that by mixing some small amount of helium with xenon one can obtain 20-30% of increase of VUV emission without proper understanding [Lu, 2008]. Thus, the research along this direction using the fluid modeling is strongly encouraged.
3. More extensive parametric study such as: 1) power source (e.g., rate of voltage increase, voltage amplitude and duty cycle); 2) geometry (e.g., gap size, dielectric thickness) and material properties (e.g., conductivity and dielectric permittivity)
4. Multidimensional fluid modeling (e.g., 2D and 3D)

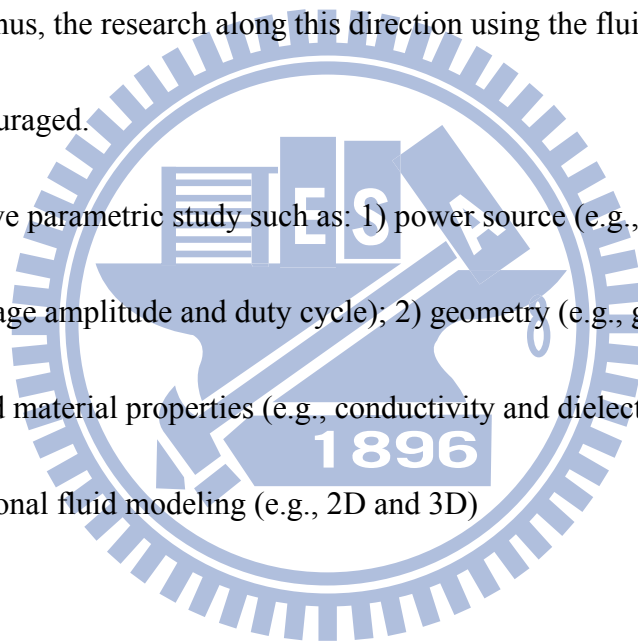


Table 3-1 Reaction channels of the xenon discharge

| No | Reaction | ε_e (eV) | Reaction rate |
|---|--|----------------------|--|
| Momentum transfer | | | |
| 1 | $e^- + Xe \rightarrow Xe + e^-$ | 0.0 | Bolsig [16] |
| Impact ionization | | | |
| 2 | $e^- + Xe \rightarrow Xe^+ + 2e^-$ | 12.1 | Bolsig [16] |
| Excitation | | | |
| 3 | $e^- + Xe \rightarrow Xe^*(ex) + e^-$ | 9.57 | Bolsig [16] |
| 4 | $e^- + Xe \rightarrow Xe^*(res) + e^-$ | 8.44 | Bolsig [16] |
| 5 | $e^- + Xe \rightarrow Xe^*(met) + e^-$ | 8.32 | Bolsig [16] |
| Stepwise ionization | | | |
| 6 | $e^- + Xe^*(met) \rightarrow Xe^+ + 2e^-$ | 3.44 | Bolsig [16] |
| Recombination | | | |
| 7 | $e^- + Xe_2^+ \rightarrow Xe^*(ex) + Xe$ | 11.1 | $2.0 \times 10^{-7} T_e^{-0.5} \text{ cm}^3 \text{ s}^{-1}$ [28] |
| Conversion to excited state | | | |
| 8 | $Xe^*(ex) + Xe \rightarrow Xe^*(res) + Xe$ | 0.0 | $2.0 \times 10^{-11} \text{ cm}^3 \text{ s}^{-1}$ [28] |
| 9 | $Xe^*(ex) + Xe \rightarrow Xe^*(met) + Xe$ | 0.0 | $2.0 \times 10^{-11} \text{ cm}^3 \text{ s}^{-1}$ [28] |
| 10 | $Xe^*(res) + Xe \rightarrow Xe^*(met) + Xe$ | 0.0 | $2.2 \times 10^{-14} \text{ cm}^3 \text{ s}^{-1}$ [28] |
| 11 | $Xe^*(met) + Xe \rightarrow Xe^*(res) + Xe$ | 0.0 | $1.5 \times 10^{-15} \text{ cm}^3 \text{ s}^{-1}$ [28] |
| Conversion to dimmers | | | |
| 12 | $Xe^*(res) + 2Xe \rightarrow Xe_2^*(O_u^+) + Xe$ | 0.0 | $1.55 \times 10^{-31} \text{ cm}^6 \text{ s}^{-1}$ [28] |
| 13 | $Xe^*(met) + 2Xe \rightarrow Xe_2^*(^3\Sigma_u^+) + Xe$ | 0.0 | $8.53 \times 10^{-32} \text{ cm}^6 \text{ s}^{-1}$ [28] |
| 14 | $Xe_2^*(O_u^+) + Xe \rightarrow Xe_2^*(^1\Sigma_u^+) + Xe$ | 0.0 | $8.7 \times 10^{-11} \text{ cm}^3 \text{ s}^{-1}$ [28] |
| Excited -excited collision induced ionization | | | |
| 15 | $Xe^*(res) + Xe^*(res) \rightarrow Xe^+ + Xe + e^-$ | 0.0 | $5.0 \times 10^{-10} \text{ cm}^3 \text{ s}^{-1}$ [28] |
| 16 | $Xe^*(met) + Xe^*(met) \rightarrow Xe^+ + Xe + e^-$ | 0.0 | $5.0 \times 10^{-10} \text{ cm}^3 \text{ s}^{-1}$ [28] |
| 17 | $Xe^*(res) + Xe^*(met) \rightarrow Xe^+ + Xe + e^-$ | 0.0 | $5.0 \times 10^{-10} \text{ cm}^3 \text{ s}^{-1}$ [28] |
| Ion conversion (three-body collision) | | | |
| 18 | $Xe^+ + Xe + Xe \rightarrow Xe_2^+ + Xe$ | 0.0 | $8.0 \times 10^{-32} \text{ cm}^6 \text{ s}^{-1}$ [28] |
| VUV emission | | | |
| 19 | $Xe_2^*(^1\Sigma_u^+) \rightarrow 2Xe + h\nu$ (172nm) | 0.0 | $1.82 \times 10^8 \text{ s}^{-1}$ [28] |
| 20 | $Xe_2^*(^3\Sigma_u^+) \rightarrow 2Xe + h\nu$ (172nm) | 0.0 | $1.0 \times 10^7 \text{ s}^{-1}$ [28] |
| 21 | $Xe_2^*(O_u^+) \rightarrow 2Xe + h\nu$ (152nm) | 0.0 | $9.0 \times 10^6 \text{ s}^{-1}$ [28] |
| 22 | $Xe^*(res) \rightarrow Xe + h\nu$ (147nm) | 0.0 | $4.3 \times 10^5 \text{ s}^{-1}$ [28] |
| Radiation to lower level (visible and infrared) | | | |
| 23 | $Xe^*(ex) \rightarrow Xe^*(res) + h\nu'$ | 0.0 | $2.7 \times 10^7 \text{ s}^{-1}$ [28] |
| 24 | $Xe^*(ex) \rightarrow Xe^*(res) + h\nu''$ | 0.0 | $2.53 \times 10^7 \text{ s}^{-1}$ [28] |

Table 4-1 Power transfer efficiency between sinusoidal and bipolar square voltages.

| | P_p (W) | P_{172} (W) | P_{172}/P_p (%) |
|-----------------------------------|-----------|---------------|-------------------|
| Sinusoidal voltages | 1909.9 | 49.2 | 2.6 |
| Distorted bipolar square voltages | 1860.5 | 124.8 | 6.7 |

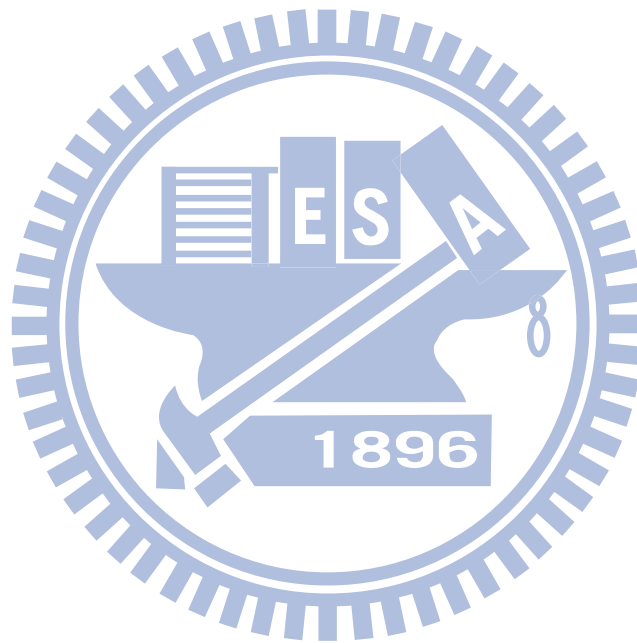


Table 5-1 Test conditions for the parametric study.

| Test parameters | | | |
|--|--|--|---|
| Frequency (f) (P:400torr, d:4.5mm, Nd:2) | Pressure (P) (f :50kHz, d:4.5mm, Nd:2) | Gap distance (d) (P:400torr, f :50kHz, Nd:2) | Num. of dielectric (Nd) (P:400torr, f:50kHz, d:4.5mm) |
| 10 - 100 (kHz) | 100 - 700 (torr) | 0.5 - 5 (mm) | One-dielectric & Two-dielectric |

* Dielectric thickness: 1 (mm)

* Permittivity of dielectric material: 4 (F/m)



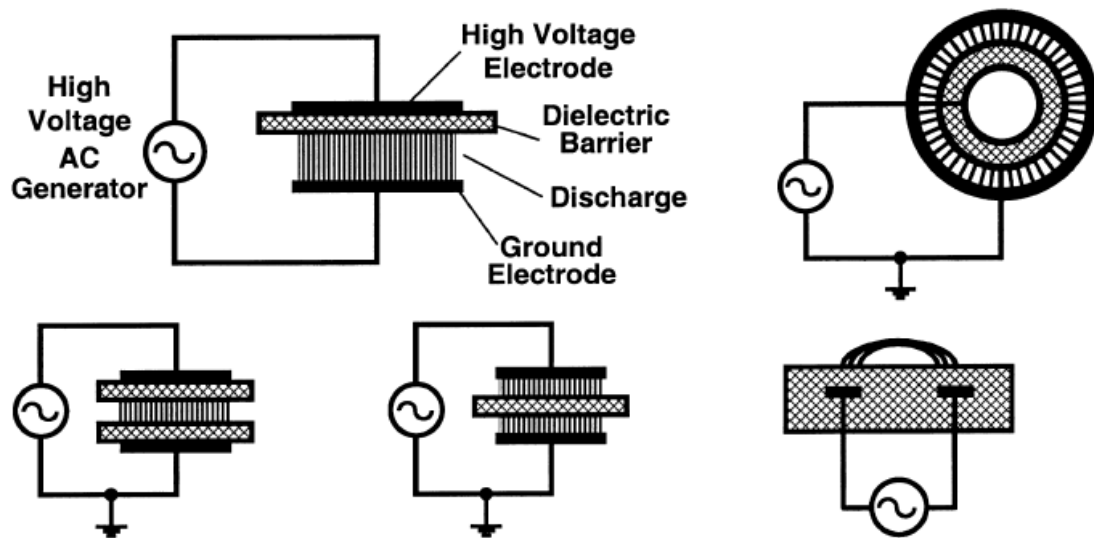
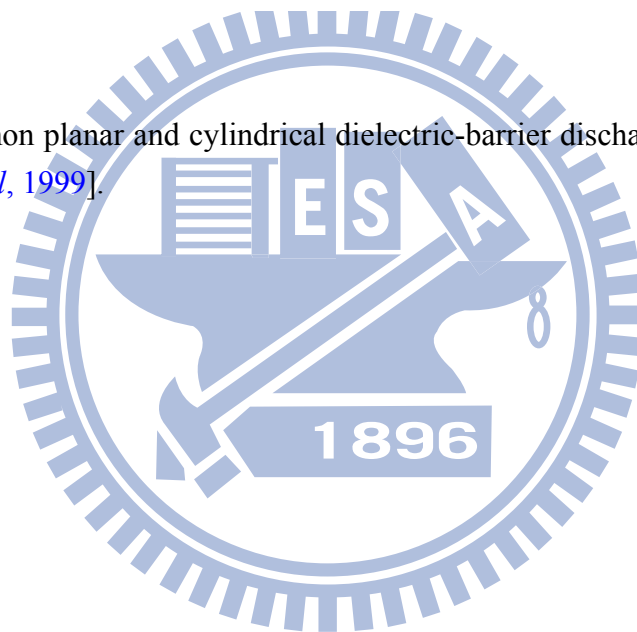


Figure 1-1 Common planar and cylindrical dielectric-barrier discharge configurations. [Kogelschatz *et al*, 1999].



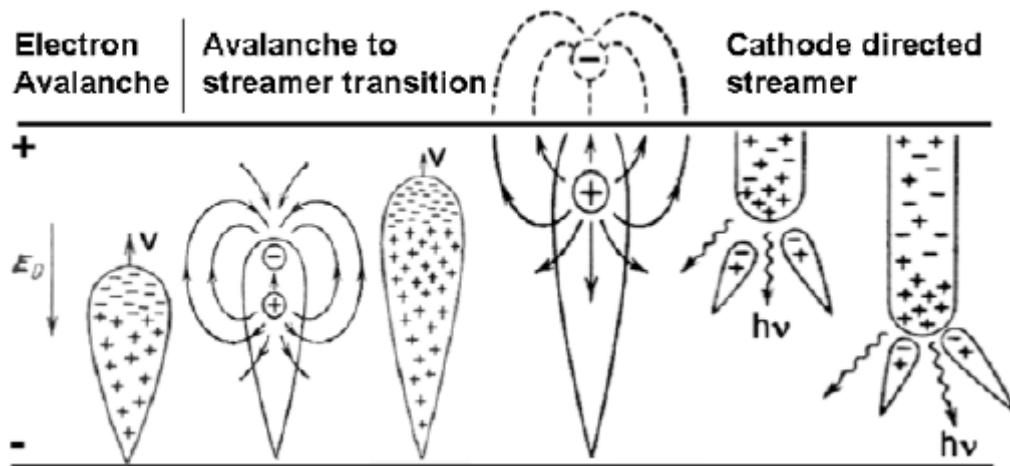
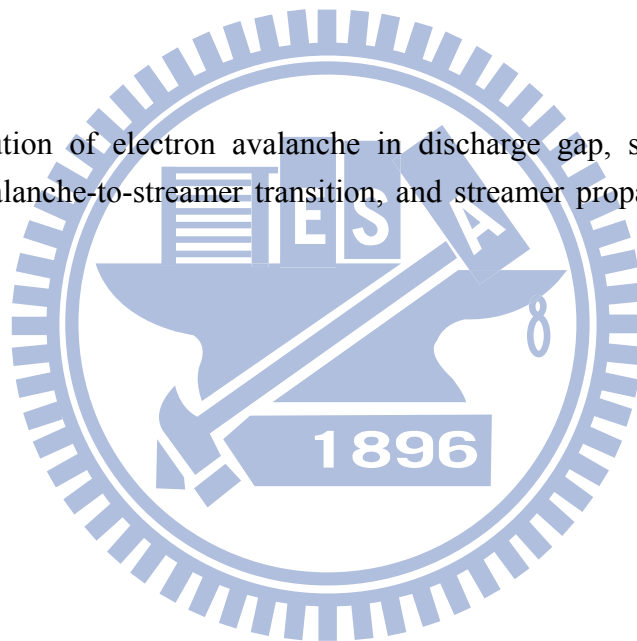


Figure 1-2 Evolution of electron avalanche in discharge gap, showing avalanche development, avalanche-to-streamer transition, and streamer propagation. [Chirokov *et al*, 2005].



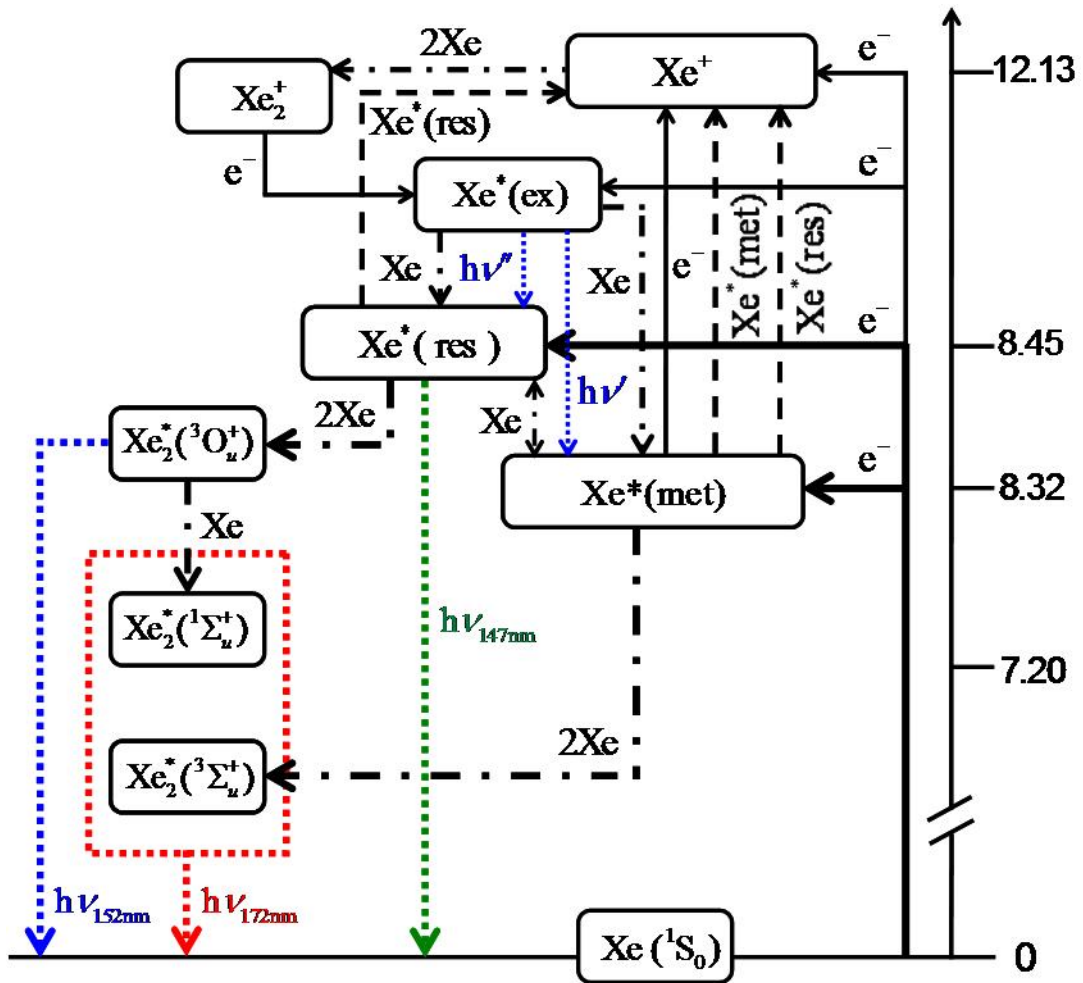


Figure 3-1 Reaction processes in a Xe discharge.

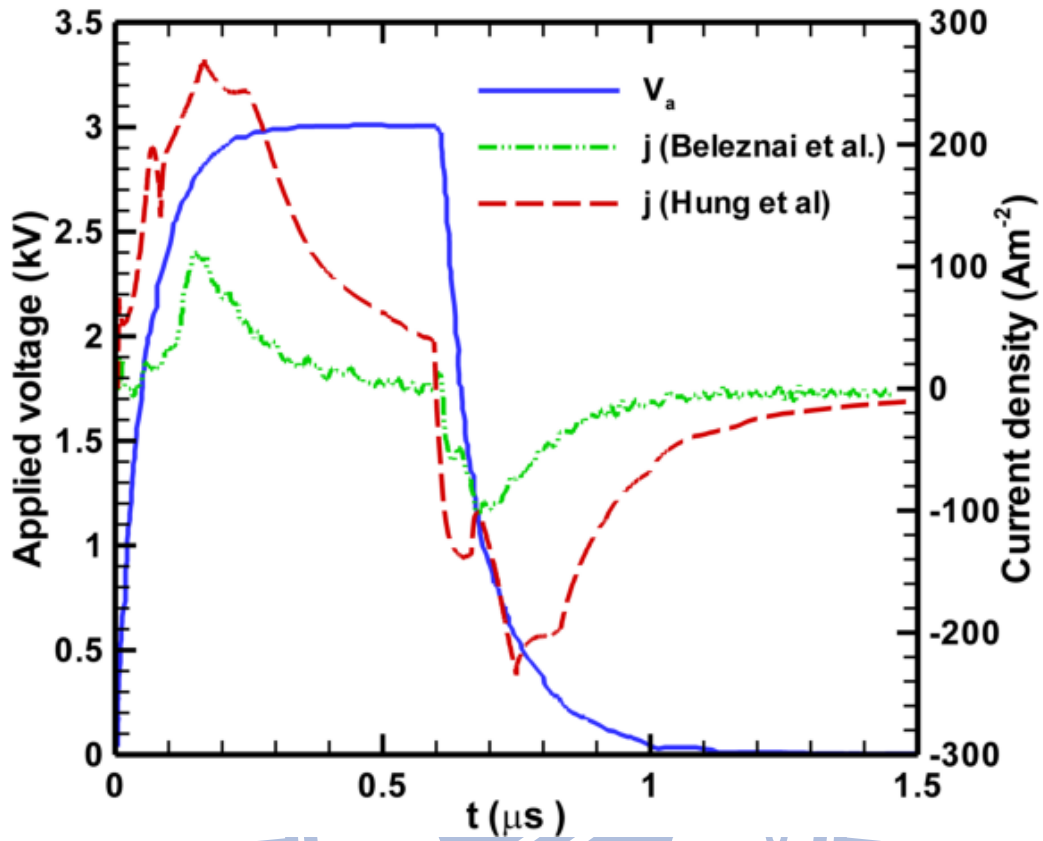


Figure 3-2 The comparison of simulated result with Beleznai *et al.* and ours.



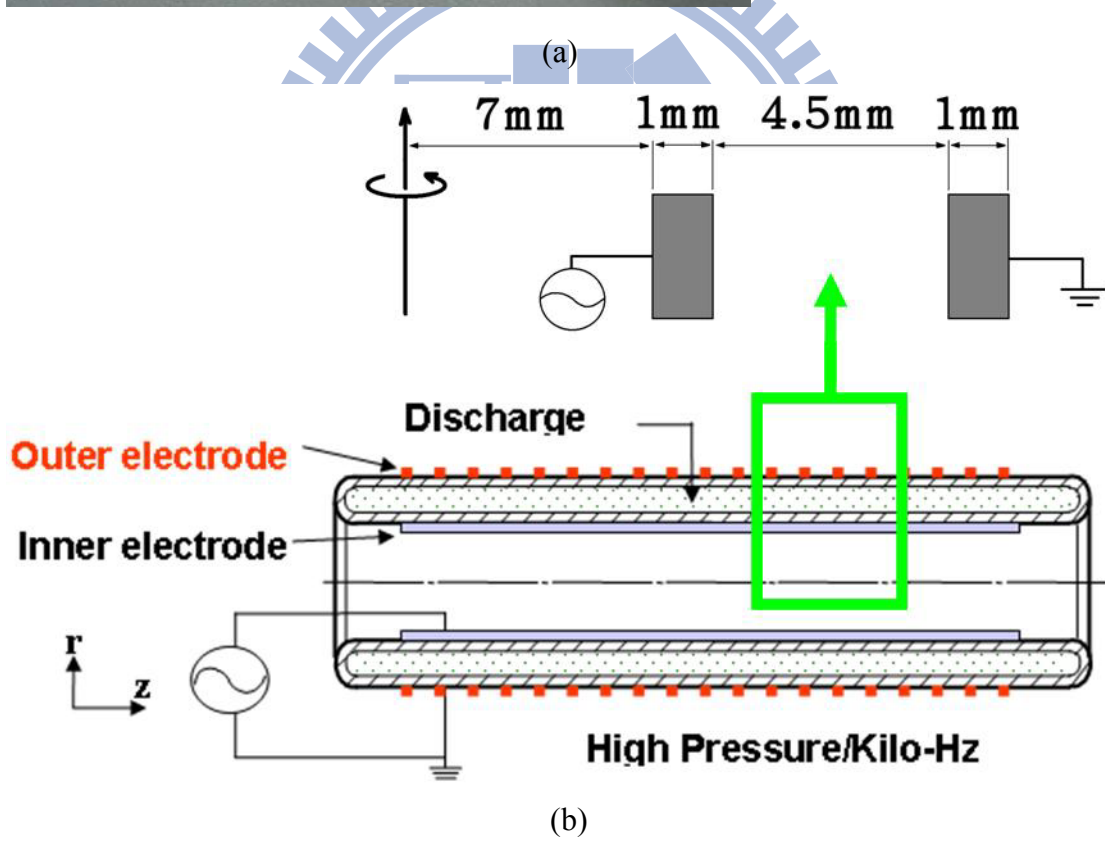


Figure 3-3(a) a sketch of the coaxial xenon excimer lamp and (b) the configuration of the coaxial xenon excimer lamp.

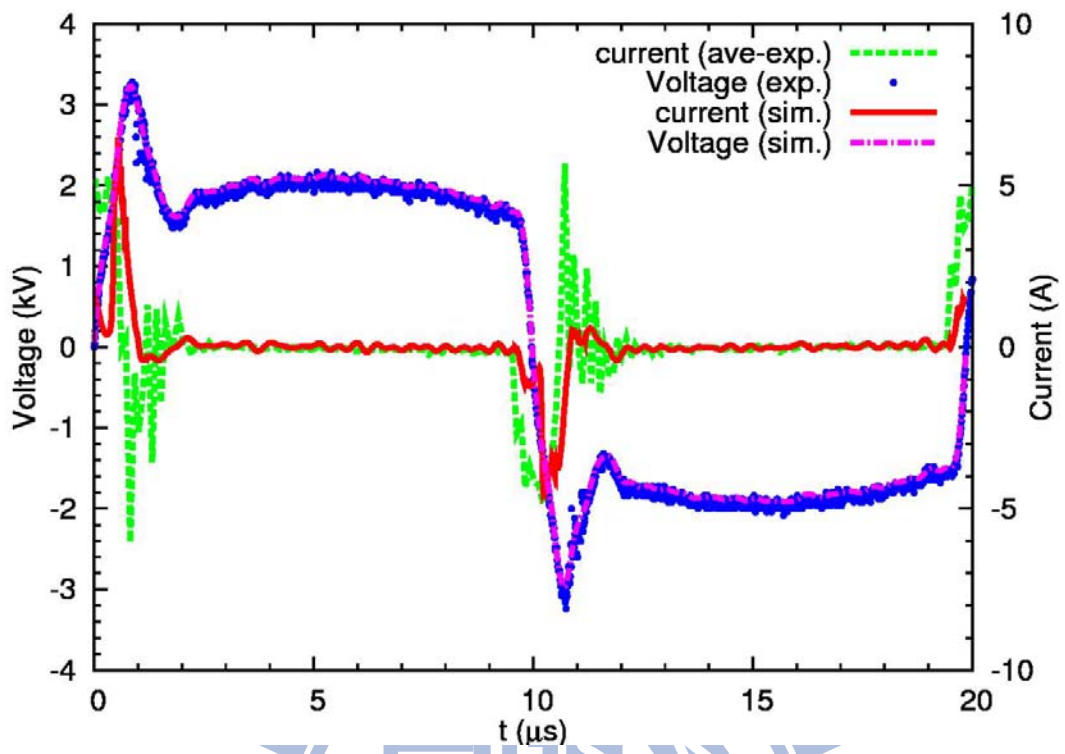
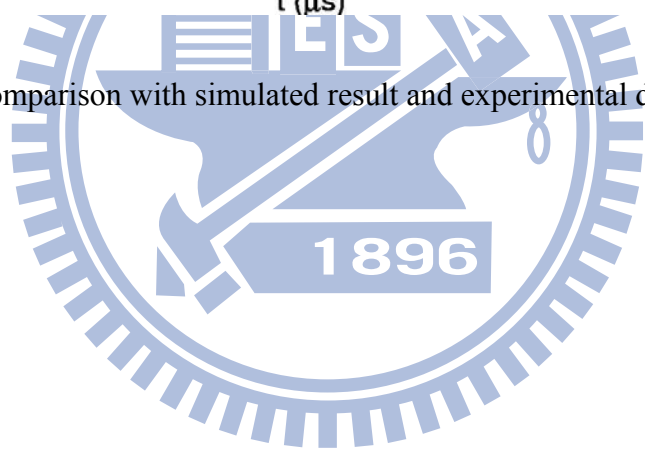


Figure 3-4 The comparison with simulated result and experimental data.



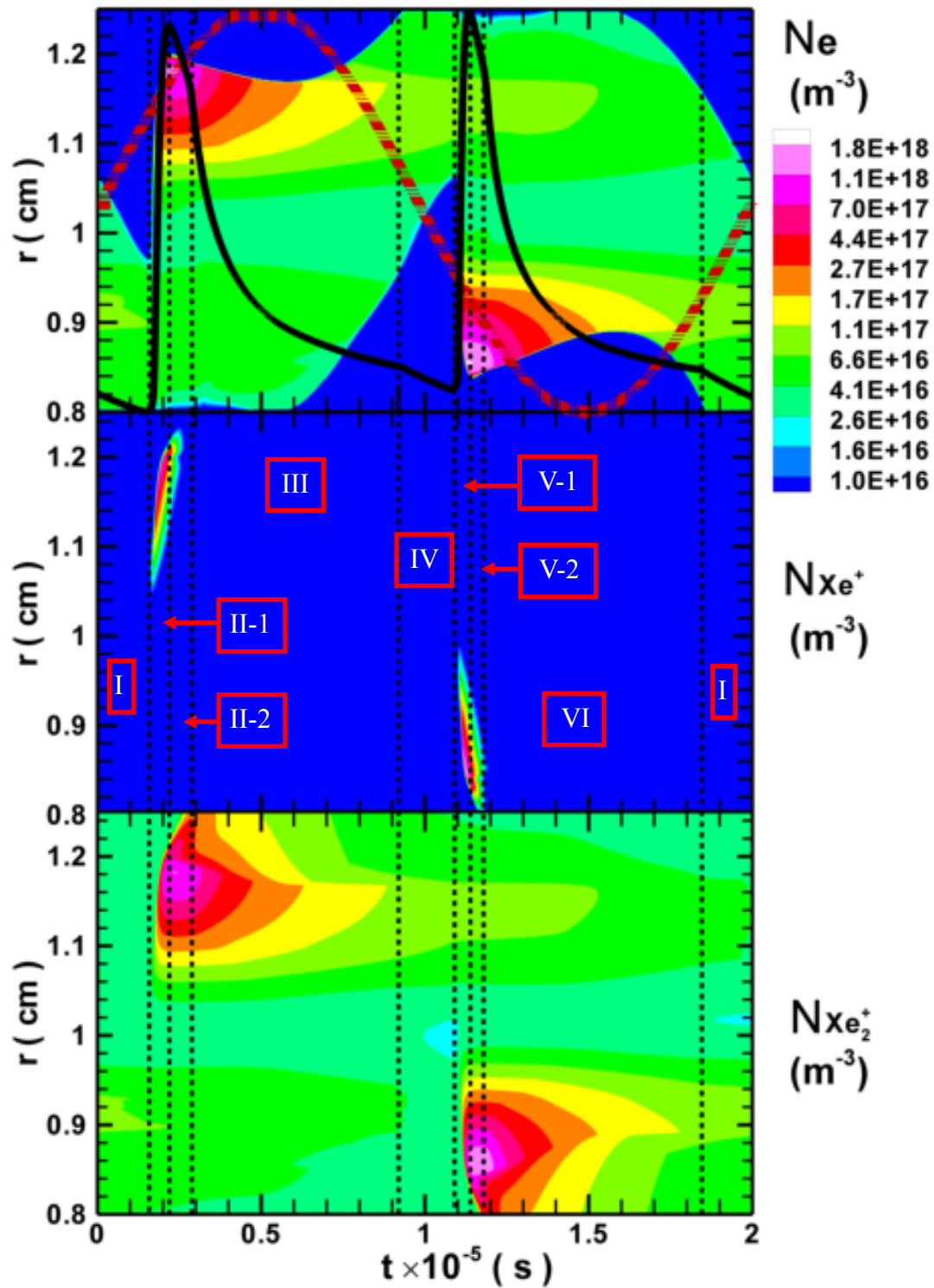


Figure 4-1 Spatiotemporal diagram of number densities of charged species: electron (upper), atomic xenon ion (middle) and molecular xenon ion (bottom).

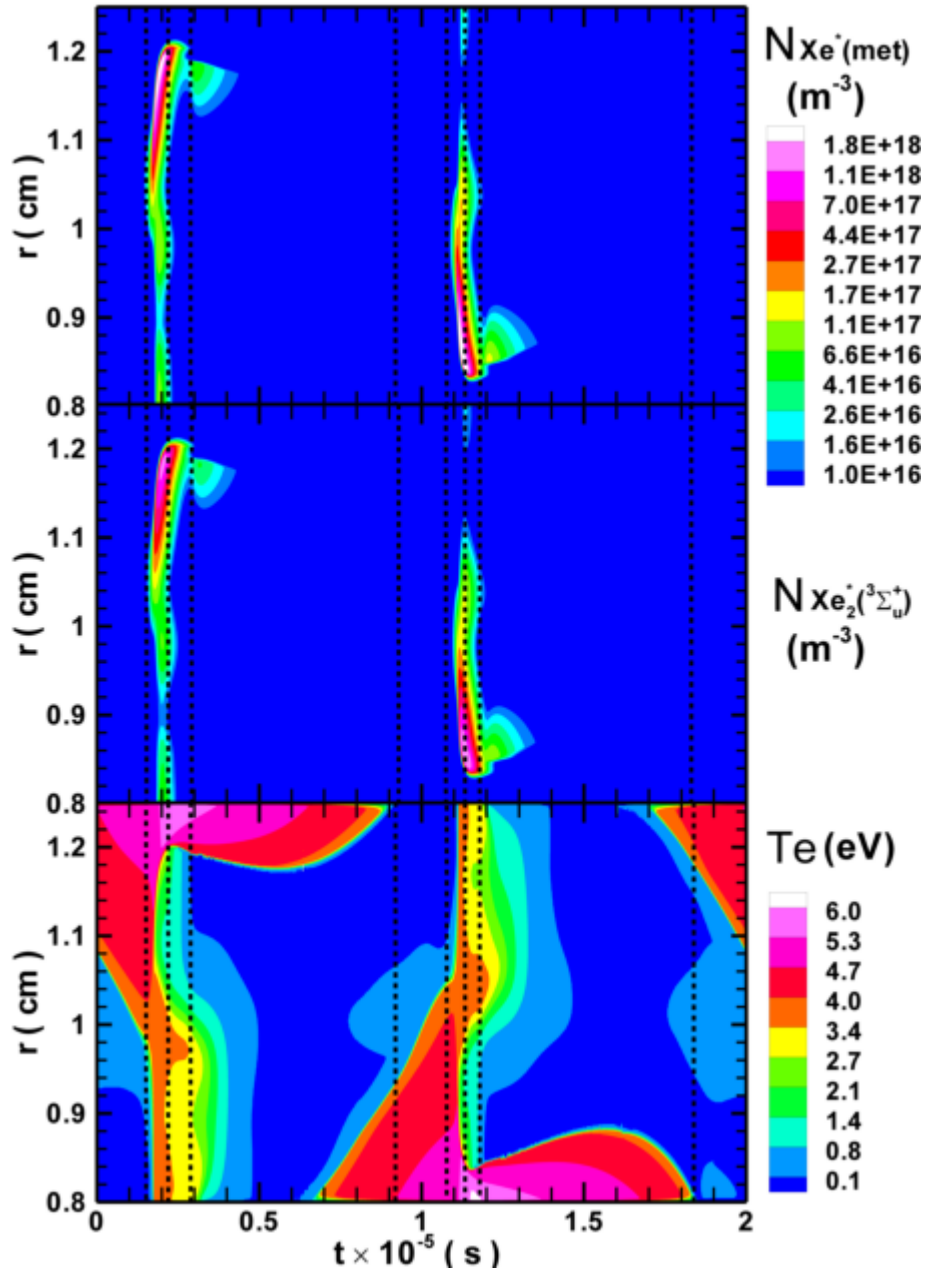


Figure 4-2 Spatiotemporal diagram of number densities of excited species: Xe^* (met) (upper), $Xe_2^*(^3\Sigma_u^+)$ (middle) and electron temperature (bottom).

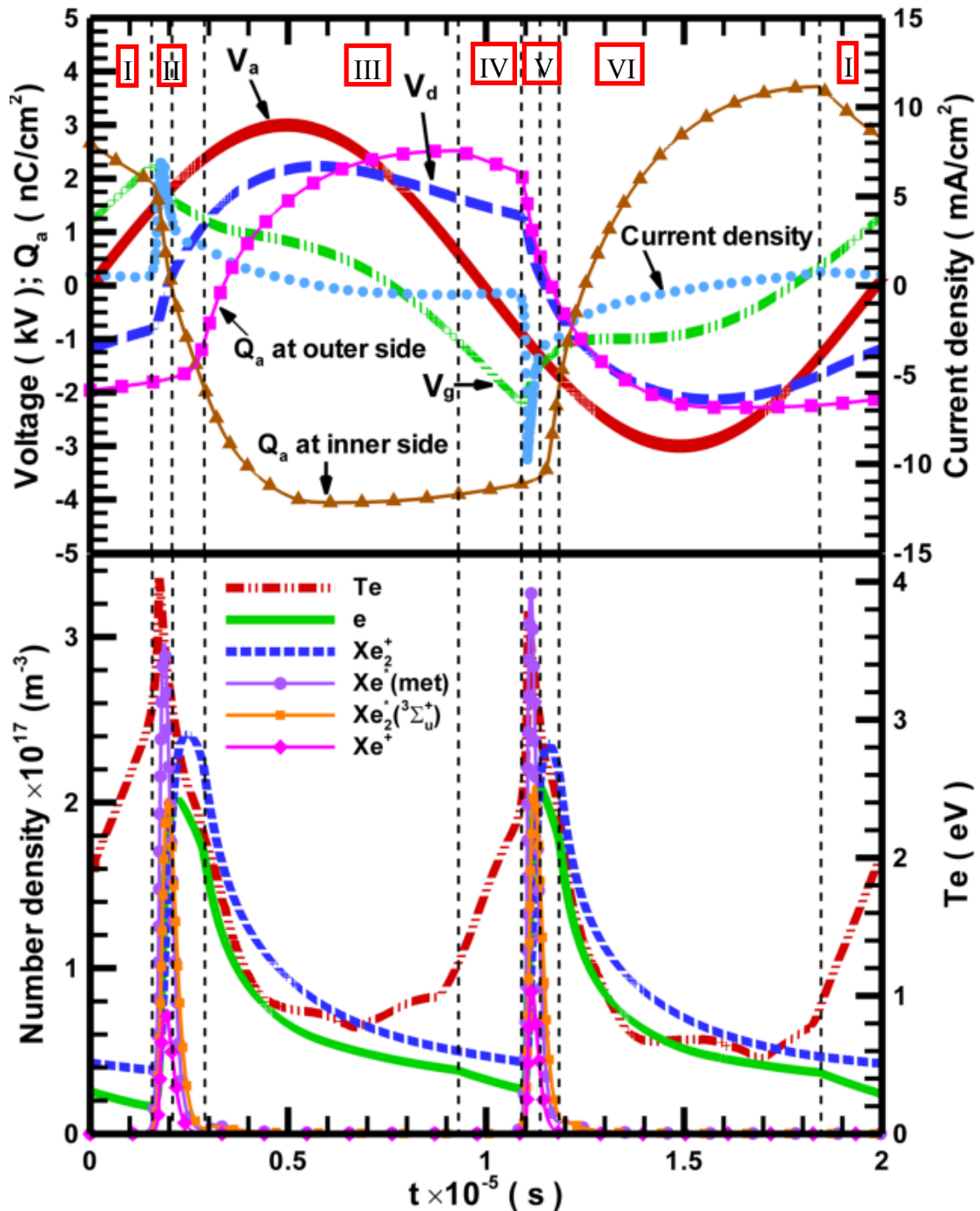


Figure 4-3 The temporal variations of (a) applied voltage (V_a), dielectric voltage (V_d), gap voltage (V_g), discharge current density at inner side ($r=0.8$ cm) and accumulated charge (Q_a) and (b) the number density of electron, the ion species Xe^+ and Xe_2^+ , the main excited species $Xe^*(met)$, the main excimer species $Xe_2^*(^3\Sigma_u^+)$ and Te utilizing sinusoidal waveform over a cycle.

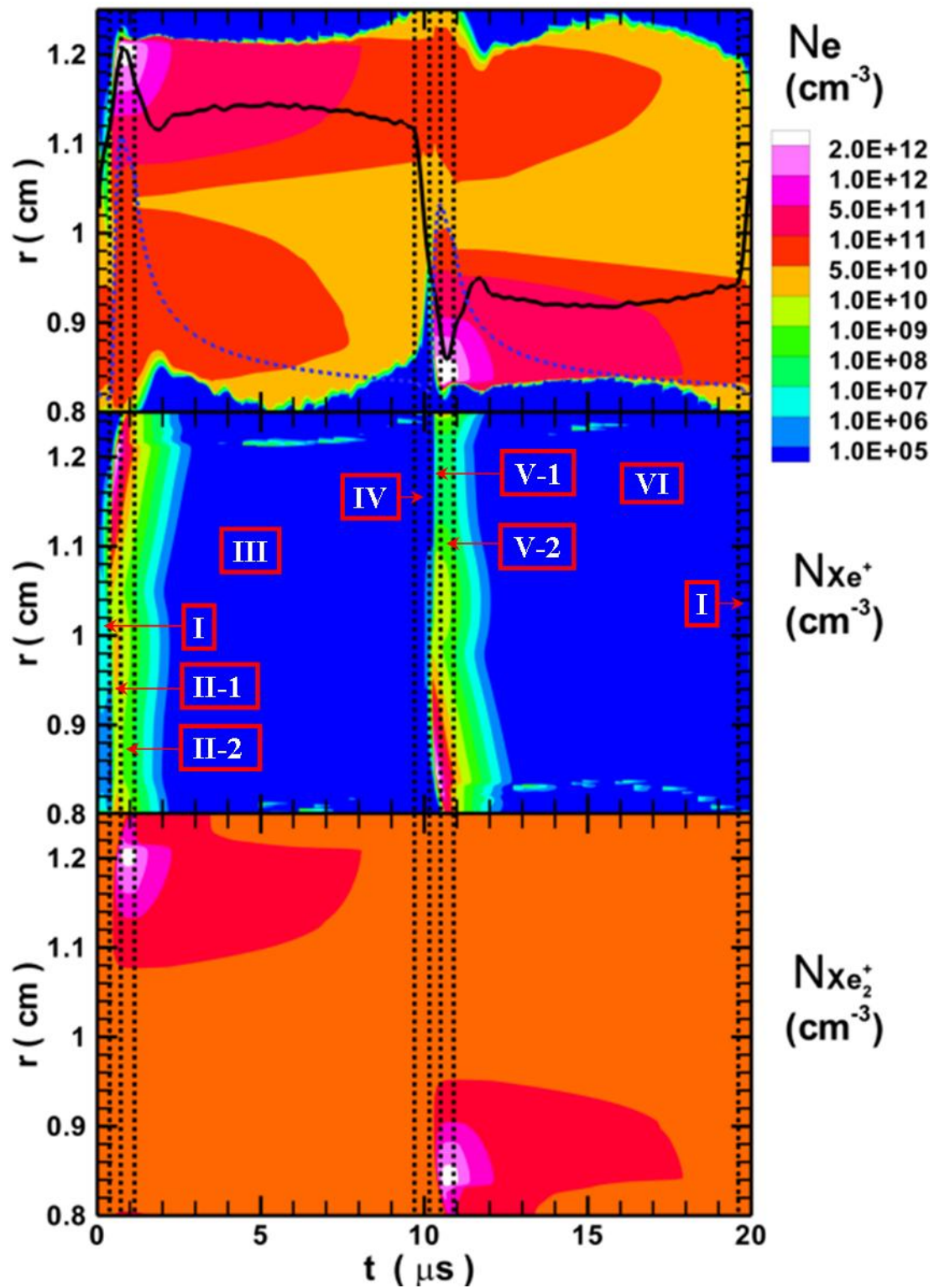


Figure 4-4 Spatiotemporal diagram of number densities of charged species: electron (upper), atomic xenon ion (middle) and molecular xenon ion (bottom).

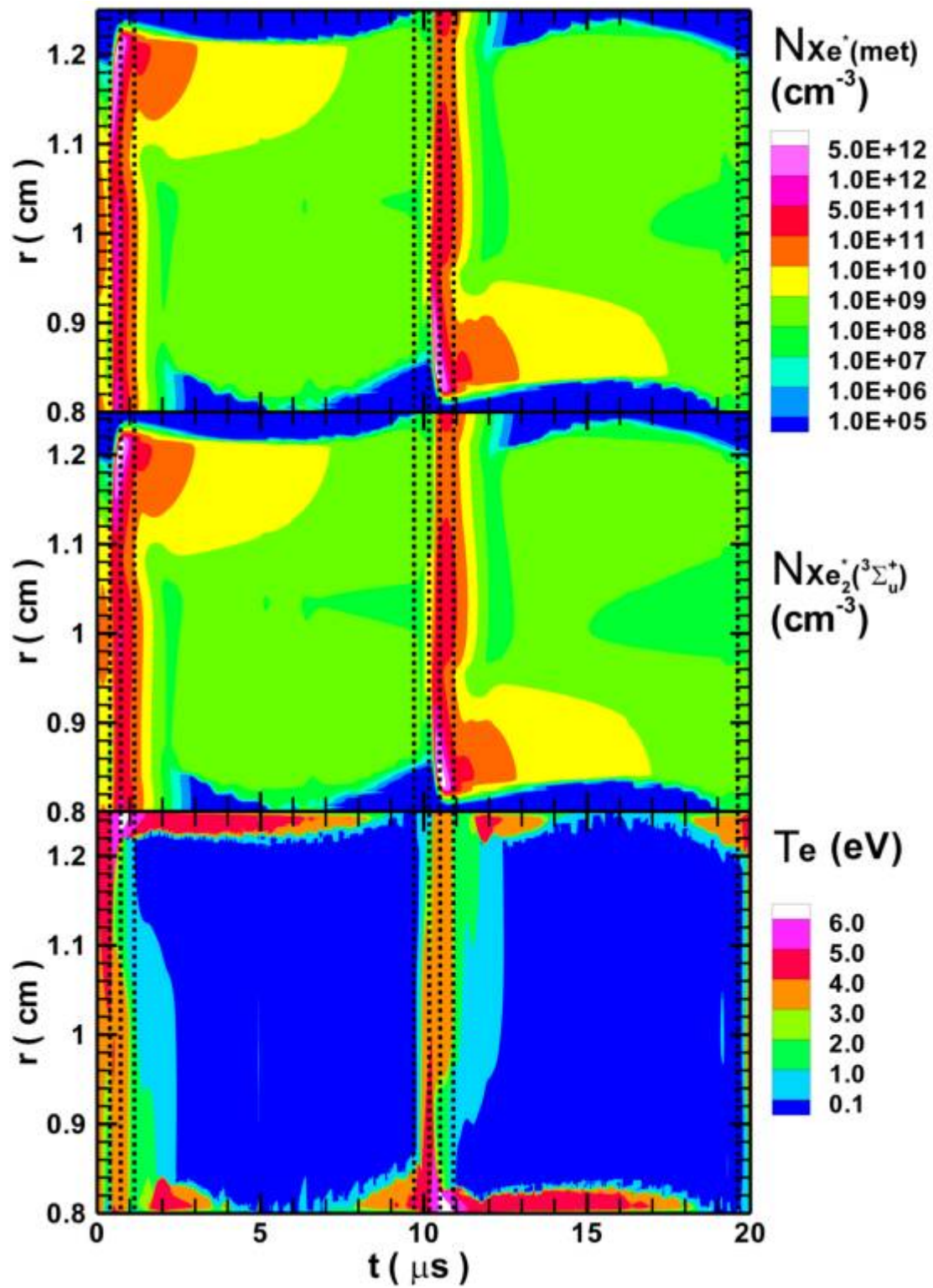
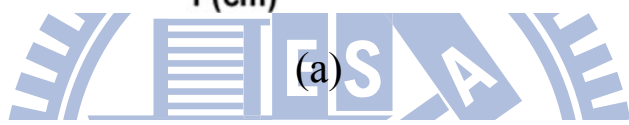
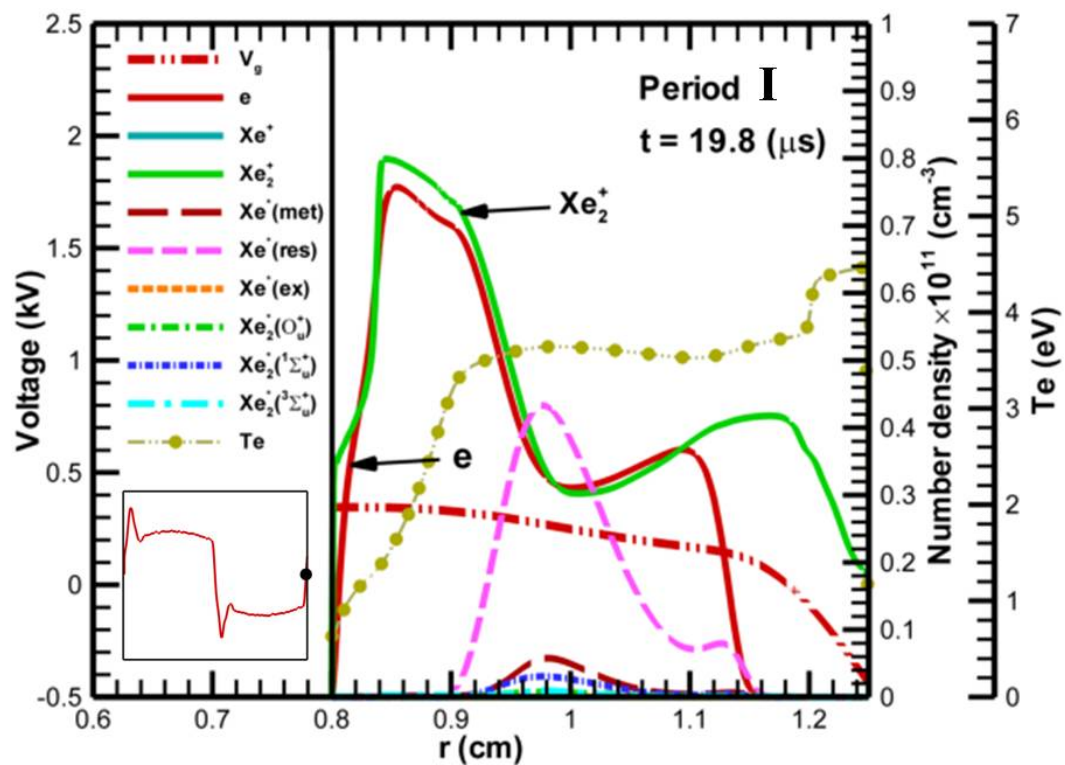
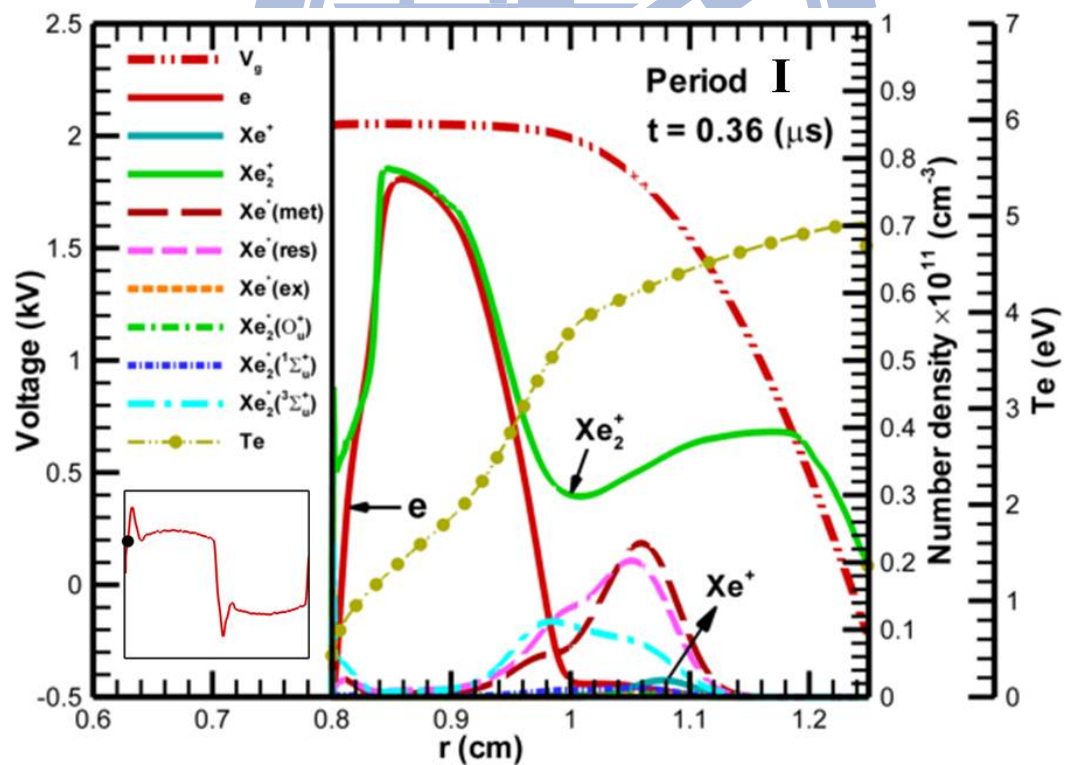


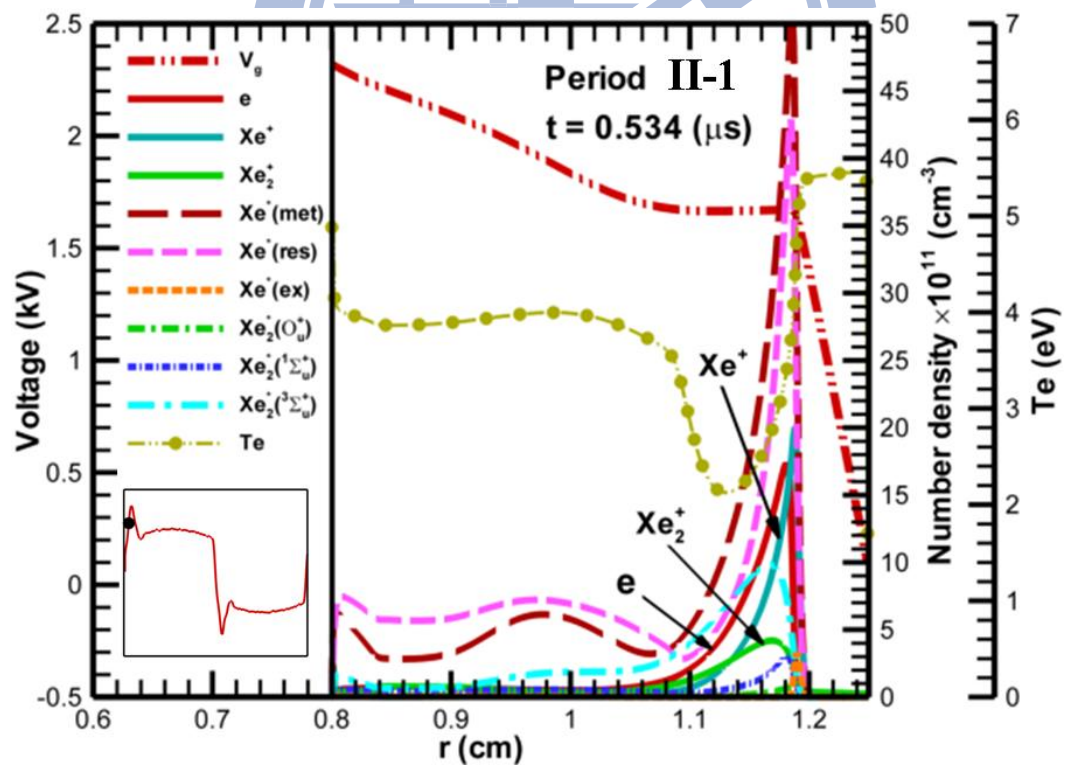
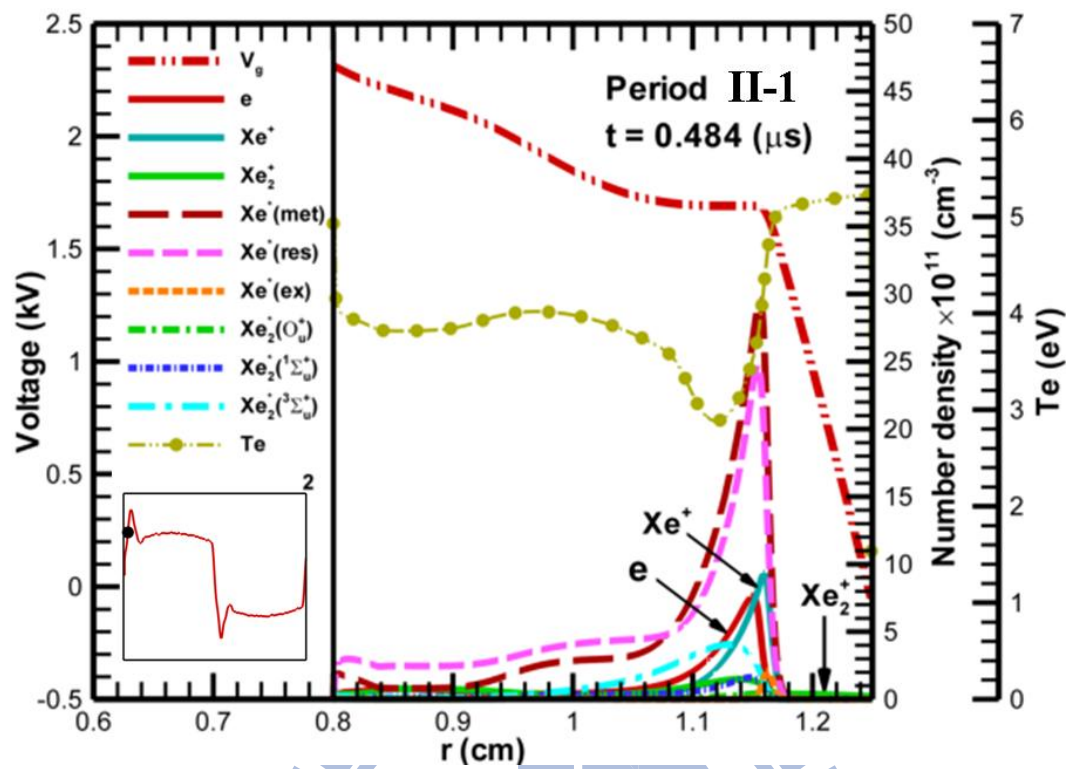
Figure 4-5 Spatiotemporal diagram of number densities of excited species: Xe^* (met) (upper), $\text{Xe}_2^*(^3\Sigma_u^+)$ (middle) and electron temperature (bottom).



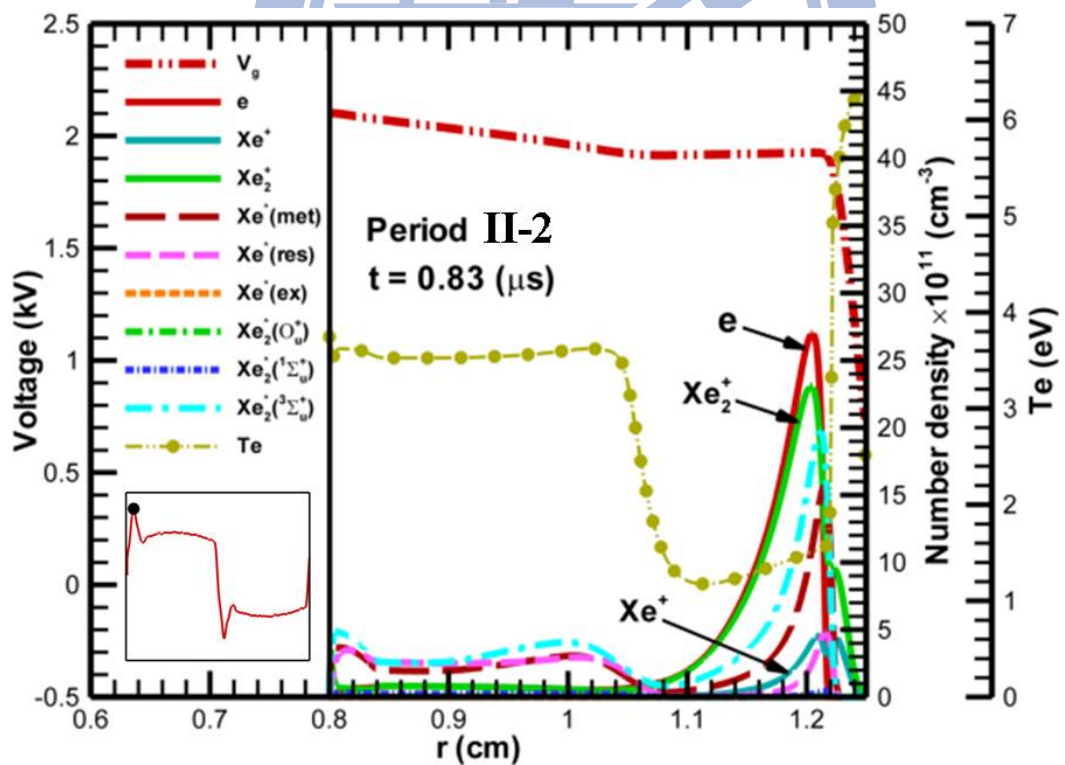
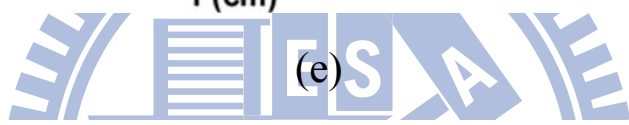
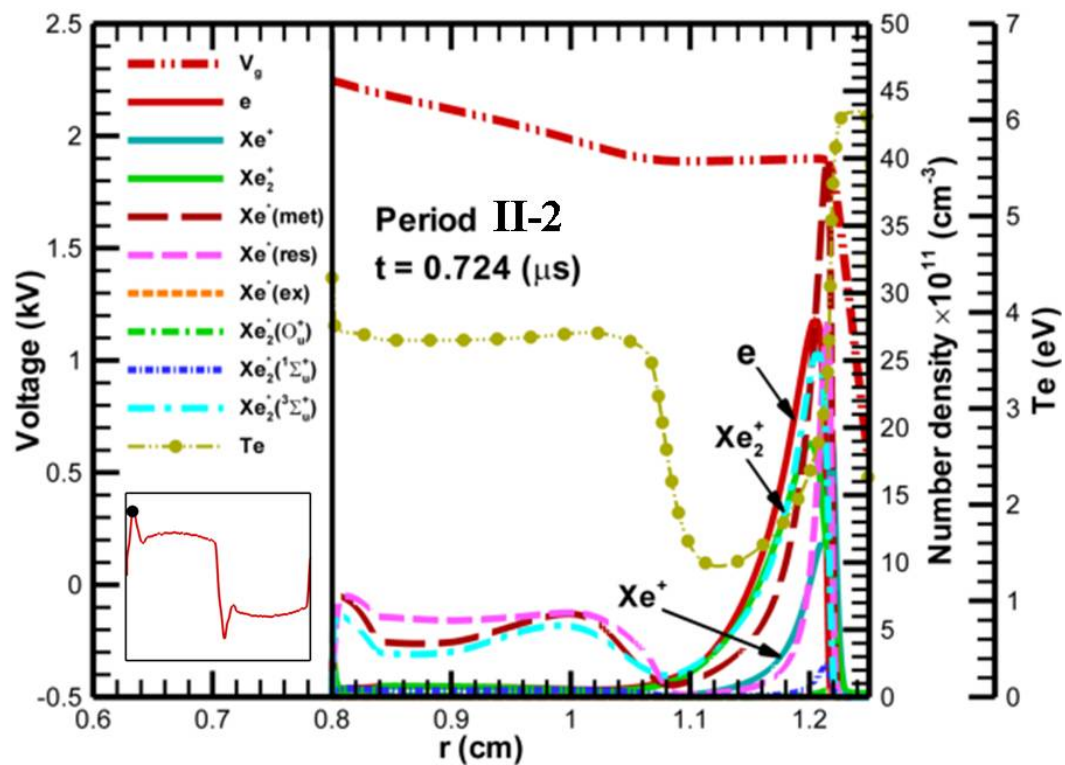
(a)



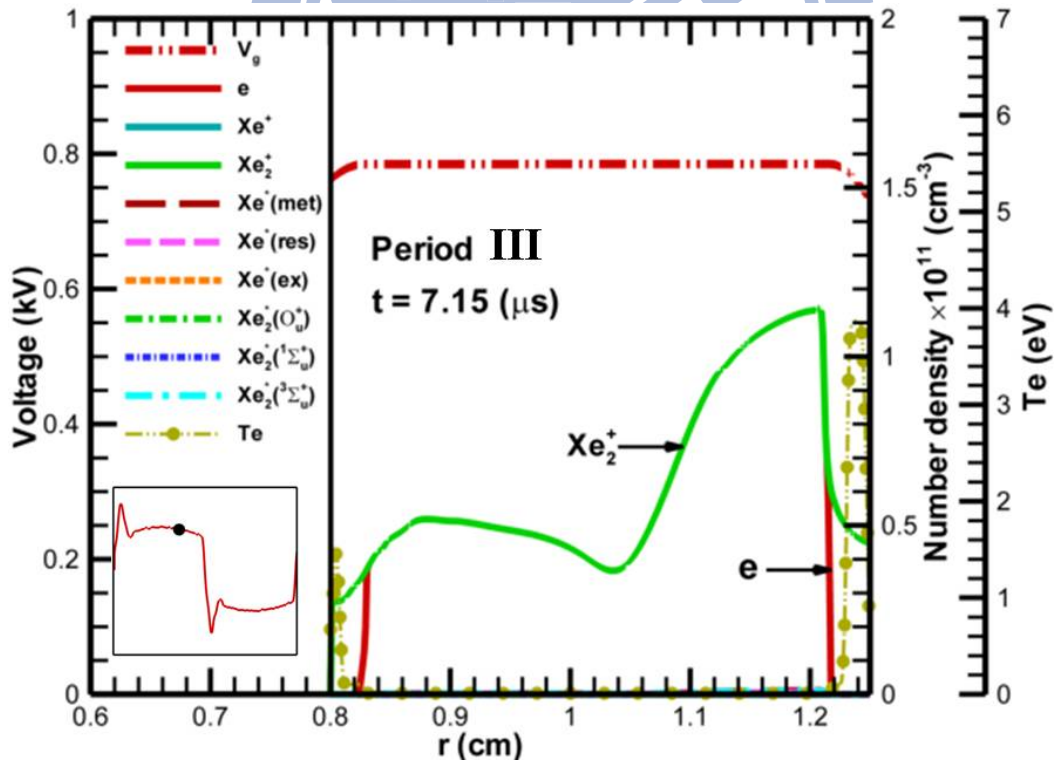
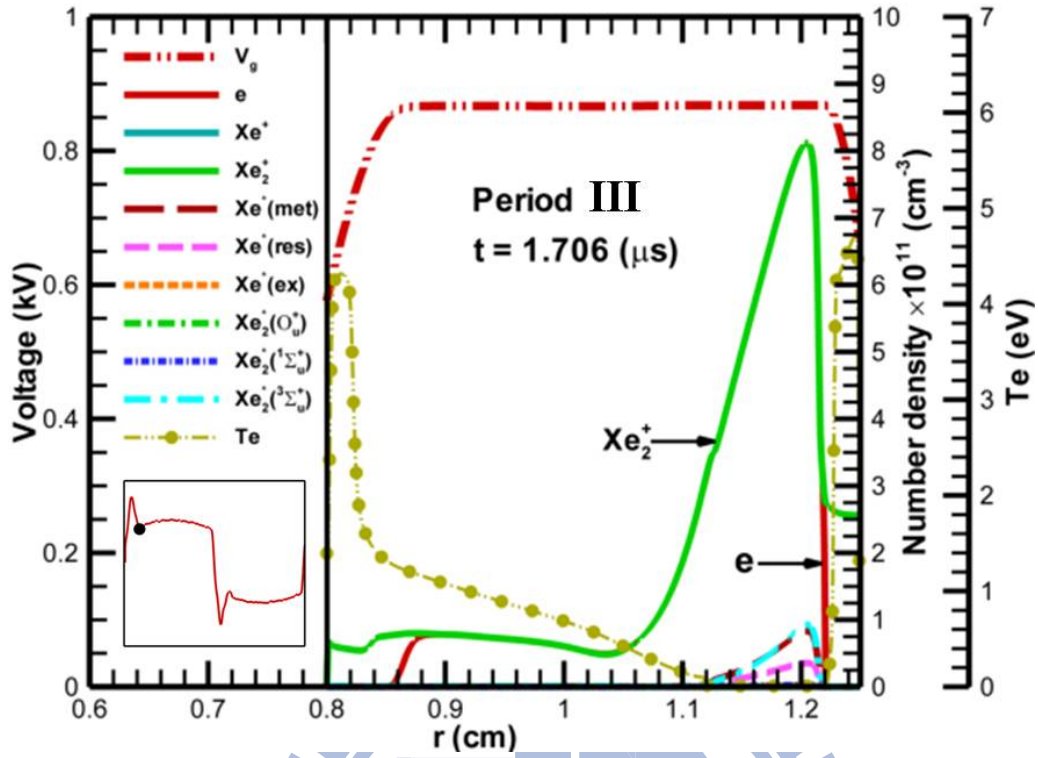
(b)



(d)



(f)



(h)

Figure 4-6 Two snapshots of total species of (a) and (b) in the period I, (c) and (d) in the period II-1, (e) and (f) in the period II-2, (g) and (h) in the period III.

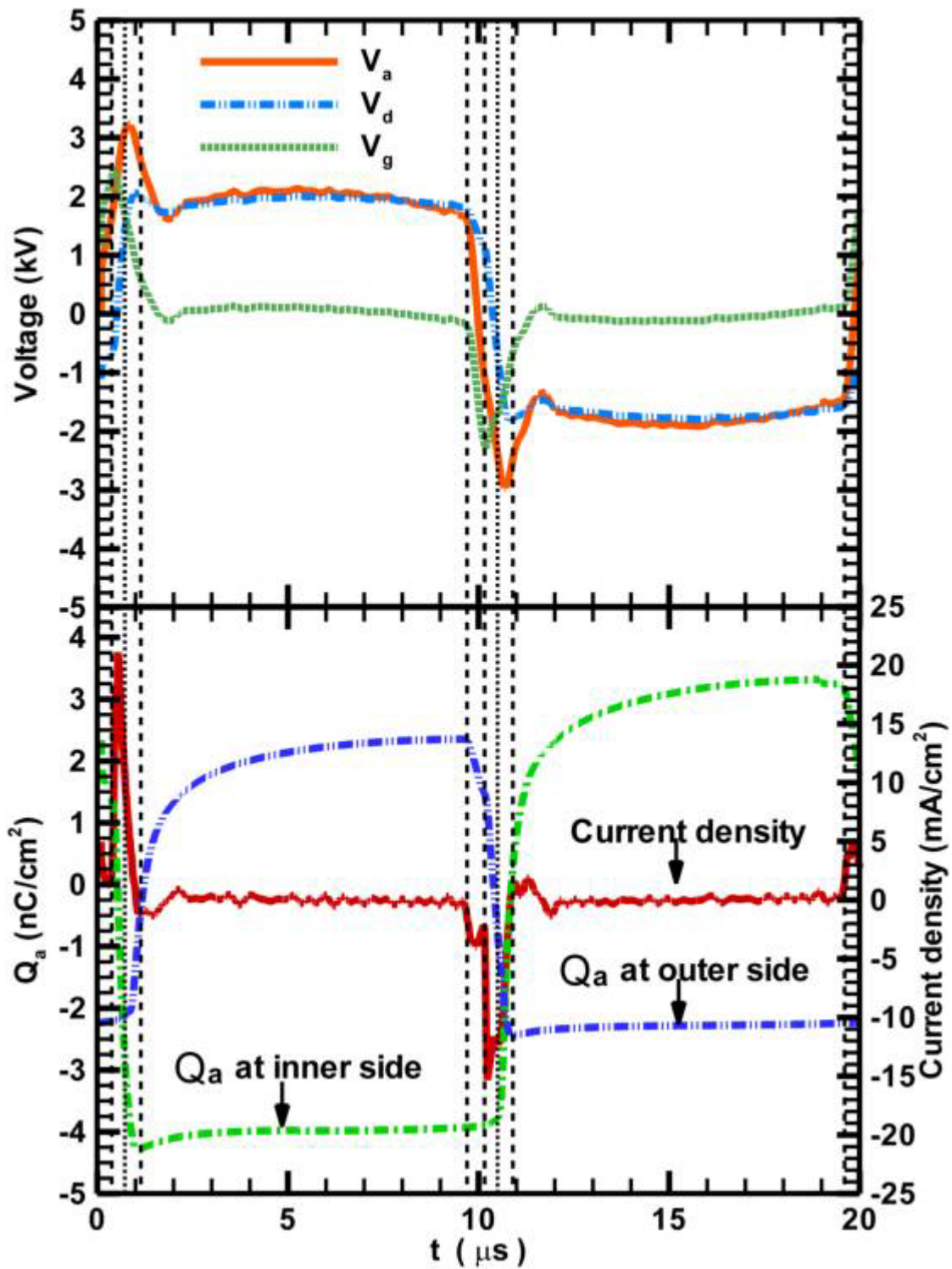


Figure 4-7 The temporal variations of (a) applied voltage (V_a), dielectric voltage (V_d) and gap voltage (V_g) in upper figure (b) discharge current density at inner side ($r=0.8$ cm) and accumulated charge (Q_a) in bottom figure utilizing distorted square voltages over a cycle.

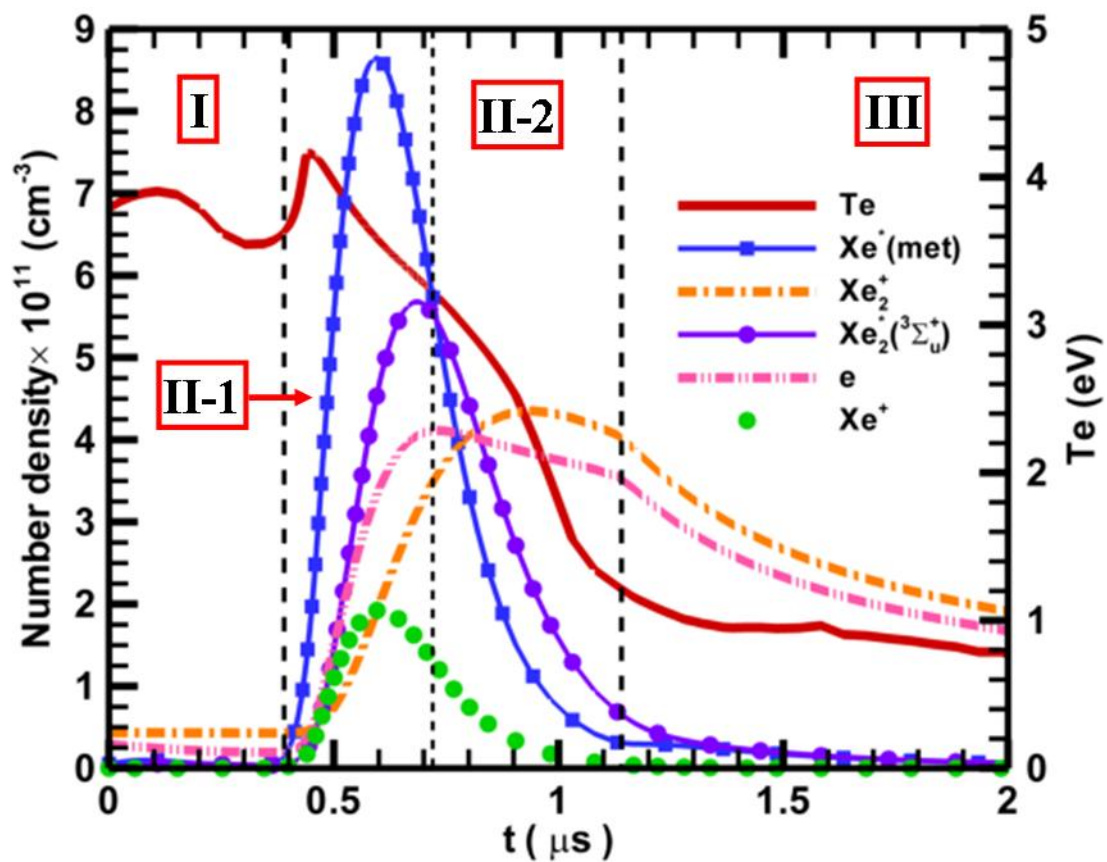


Figure 4-8 The temporal variations of number density of electron, the ion species Xe^+ and Xe_2^+ , the main excited species $\text{Xe}^*(\text{met})$, the main excimer species $\text{Xe}_2^*(^3\Sigma_u^+)$ and Te during the period $t=0 \sim 2$ (μs).

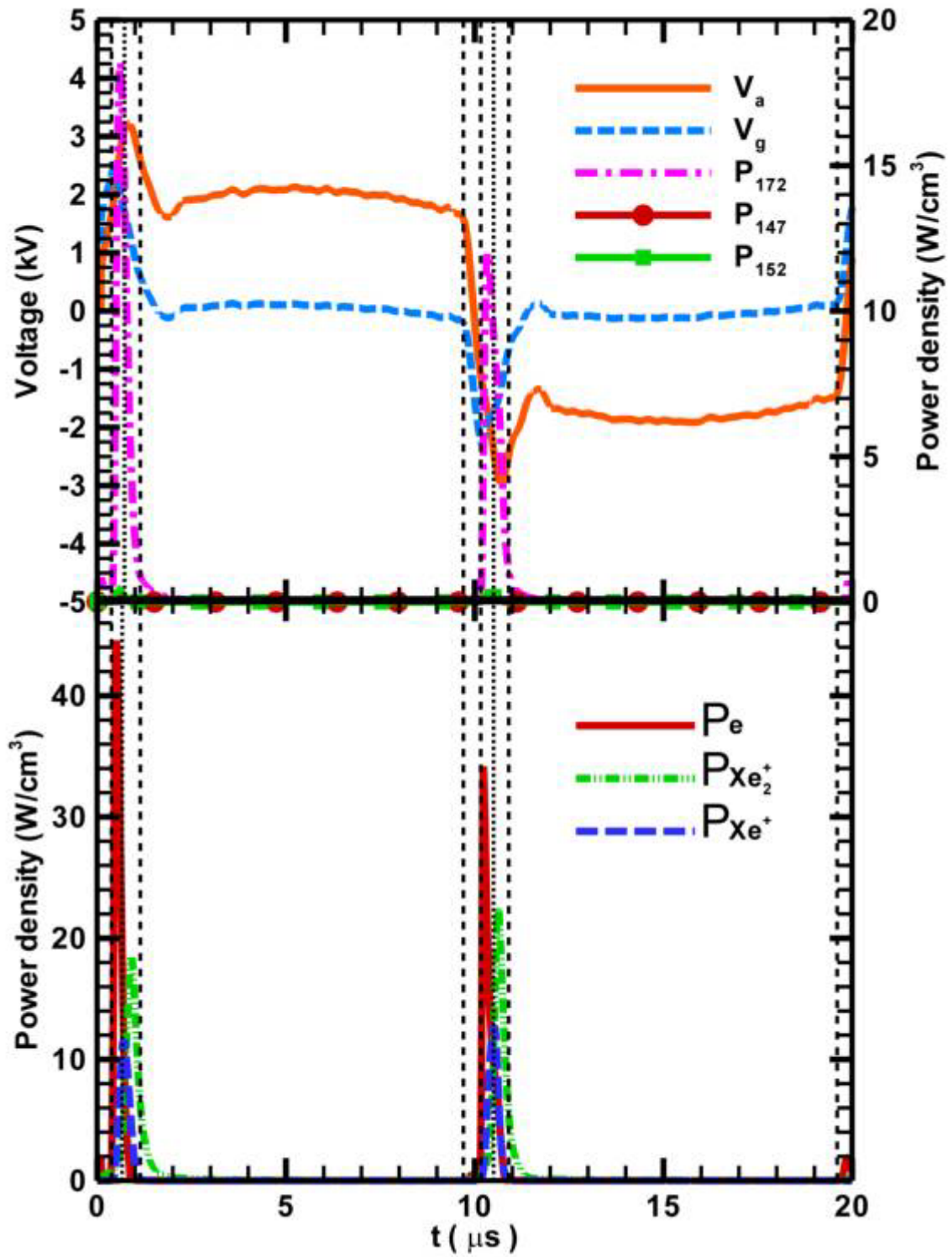
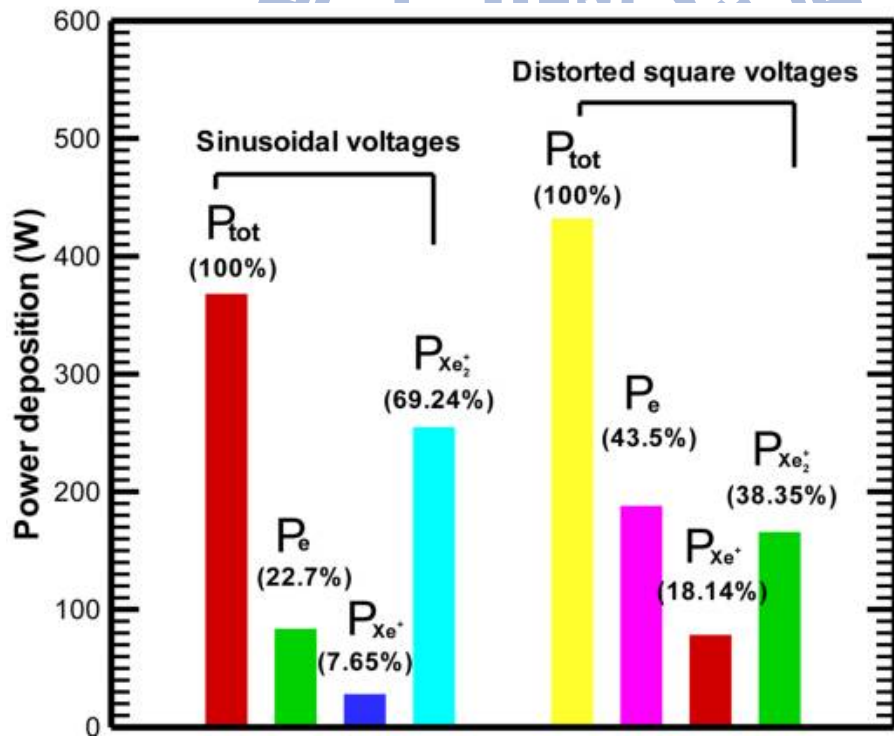
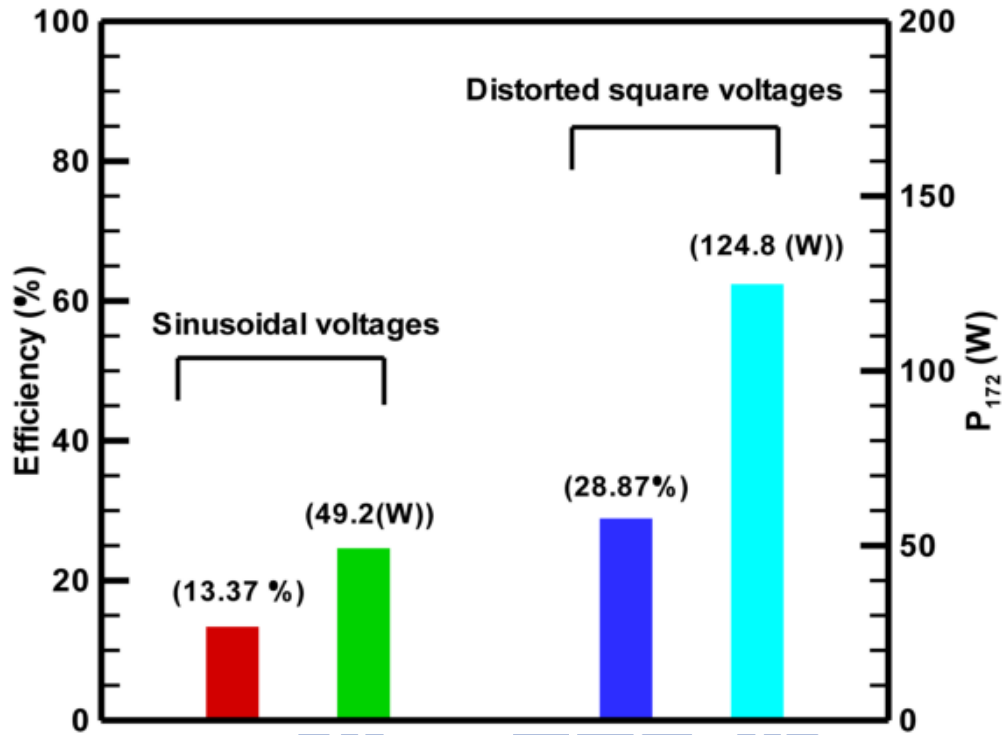


Figure 4-9 The power emission in the upper figure and power deposition utilizing distorted square voltages over a cycle.



(b)

Figure 4-10(a) The efficiency and P_{172} under different power source. (b) The deposition power and power partition under different power source.

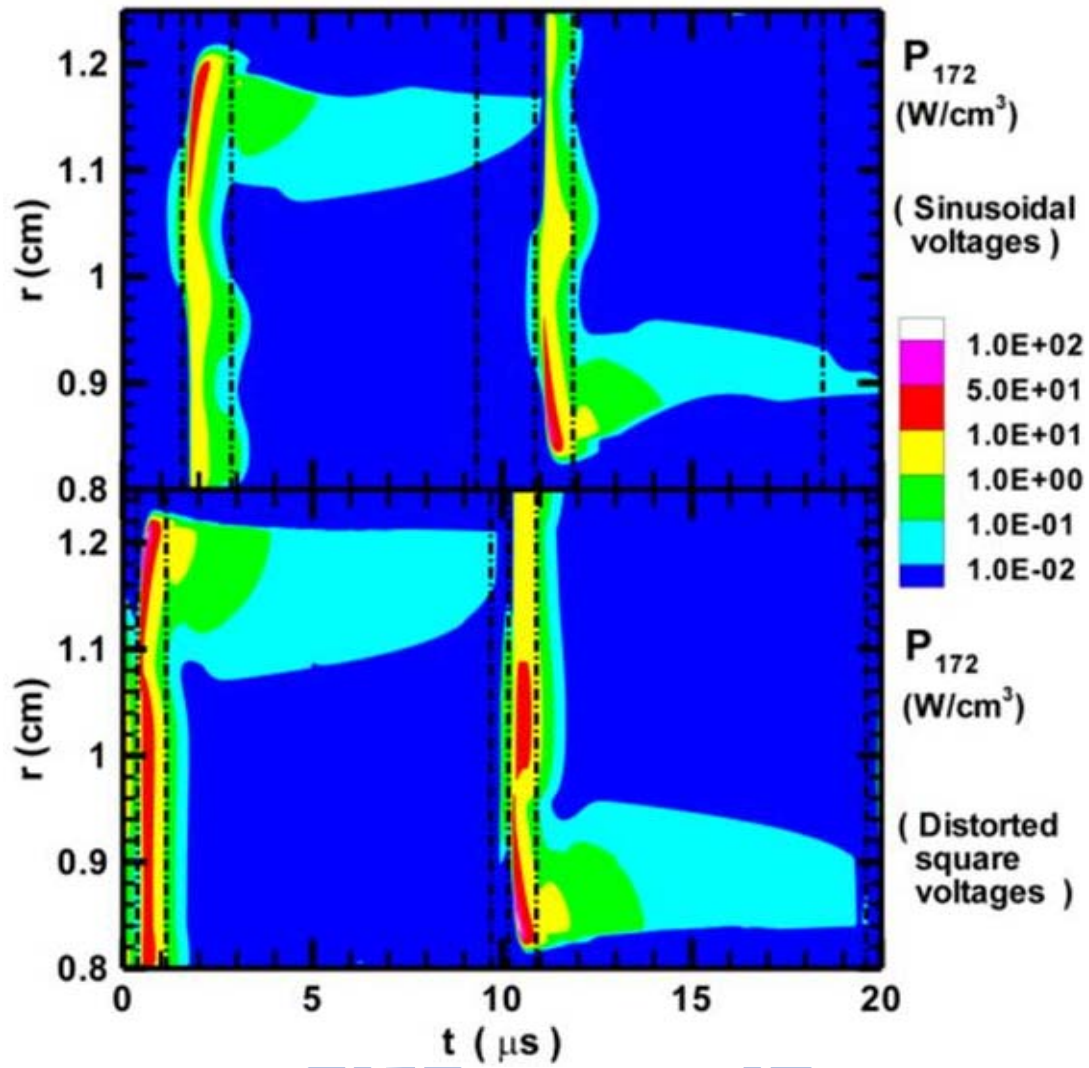


Figure 4-11 The comparison of light power emission (P_{172}) between sinusoidal voltages (the upper figure) and distorted square voltages (the bottom figure).

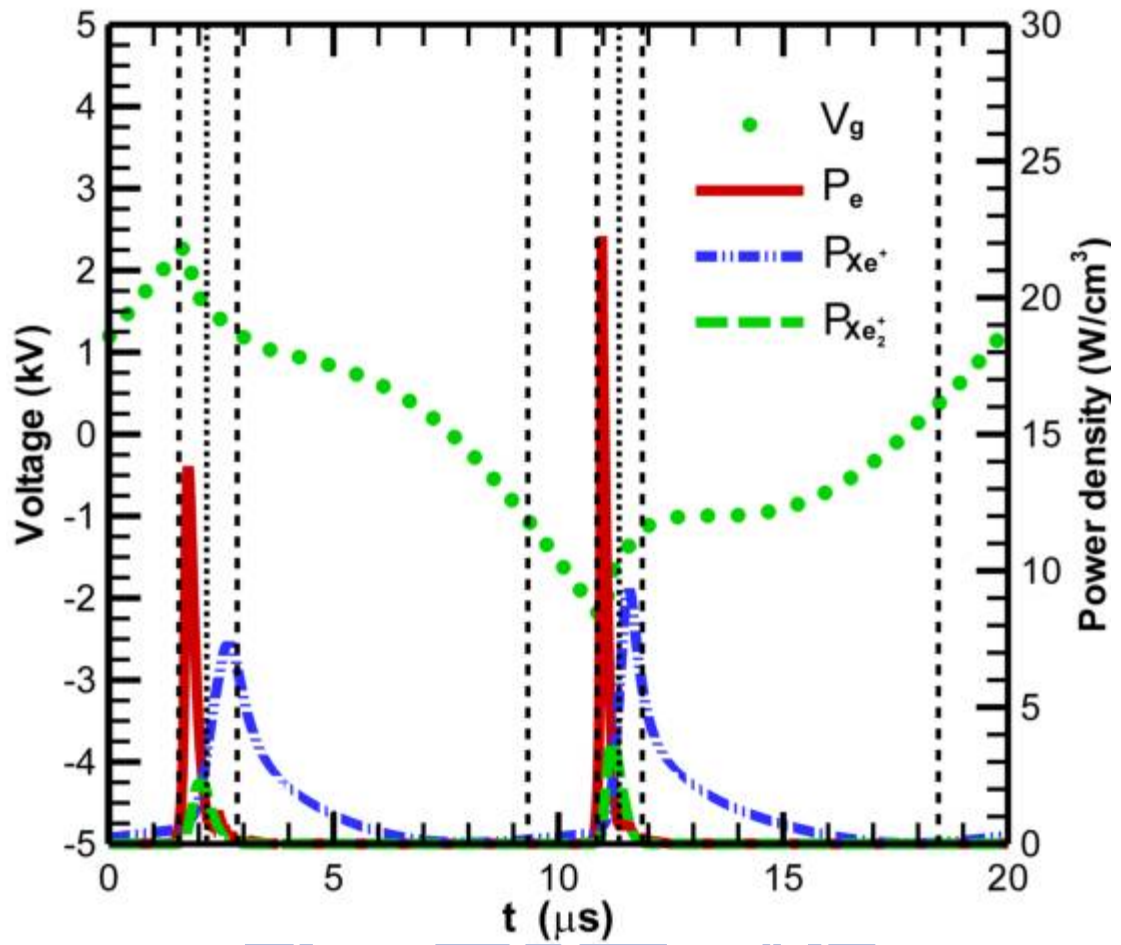


Figure 4-12 The comparison of power deposition between sinusoidal voltages (the upper figure) and distorted square voltages (the bottom figure).

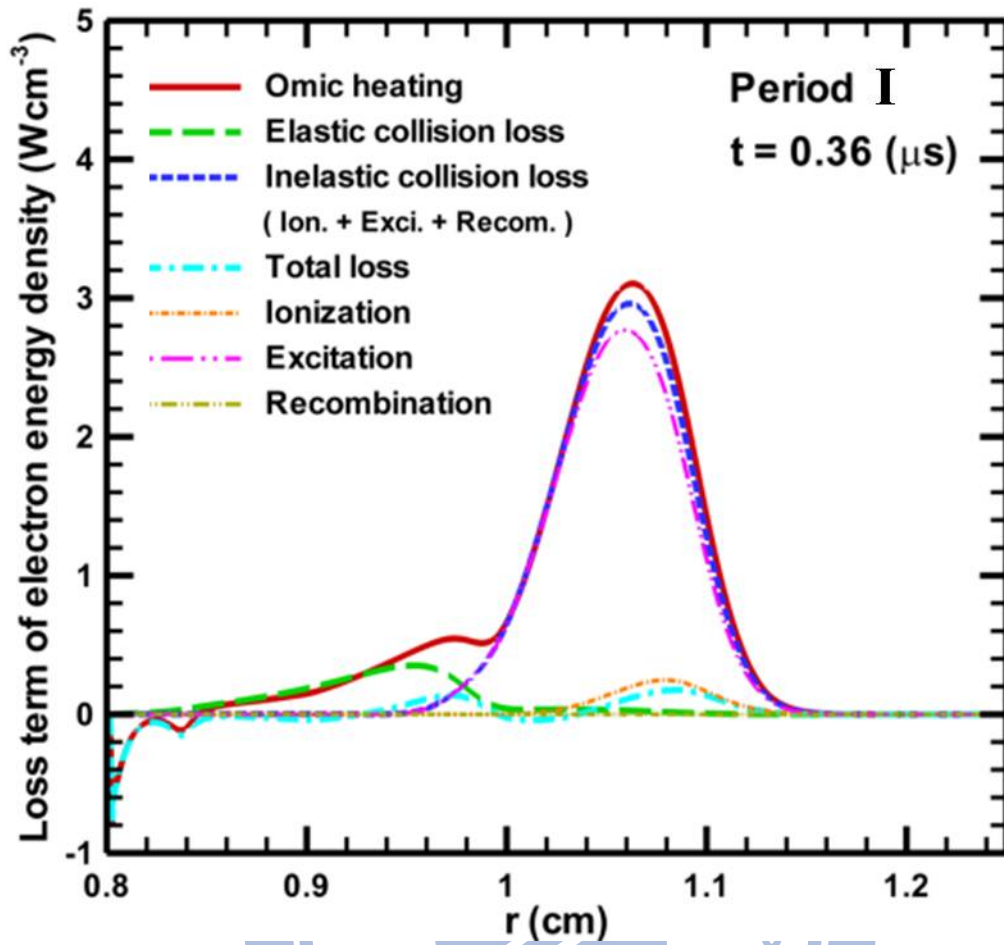


Figure 4-13 A snapshot of distributions of electron energy consumption components using distorted square voltages.

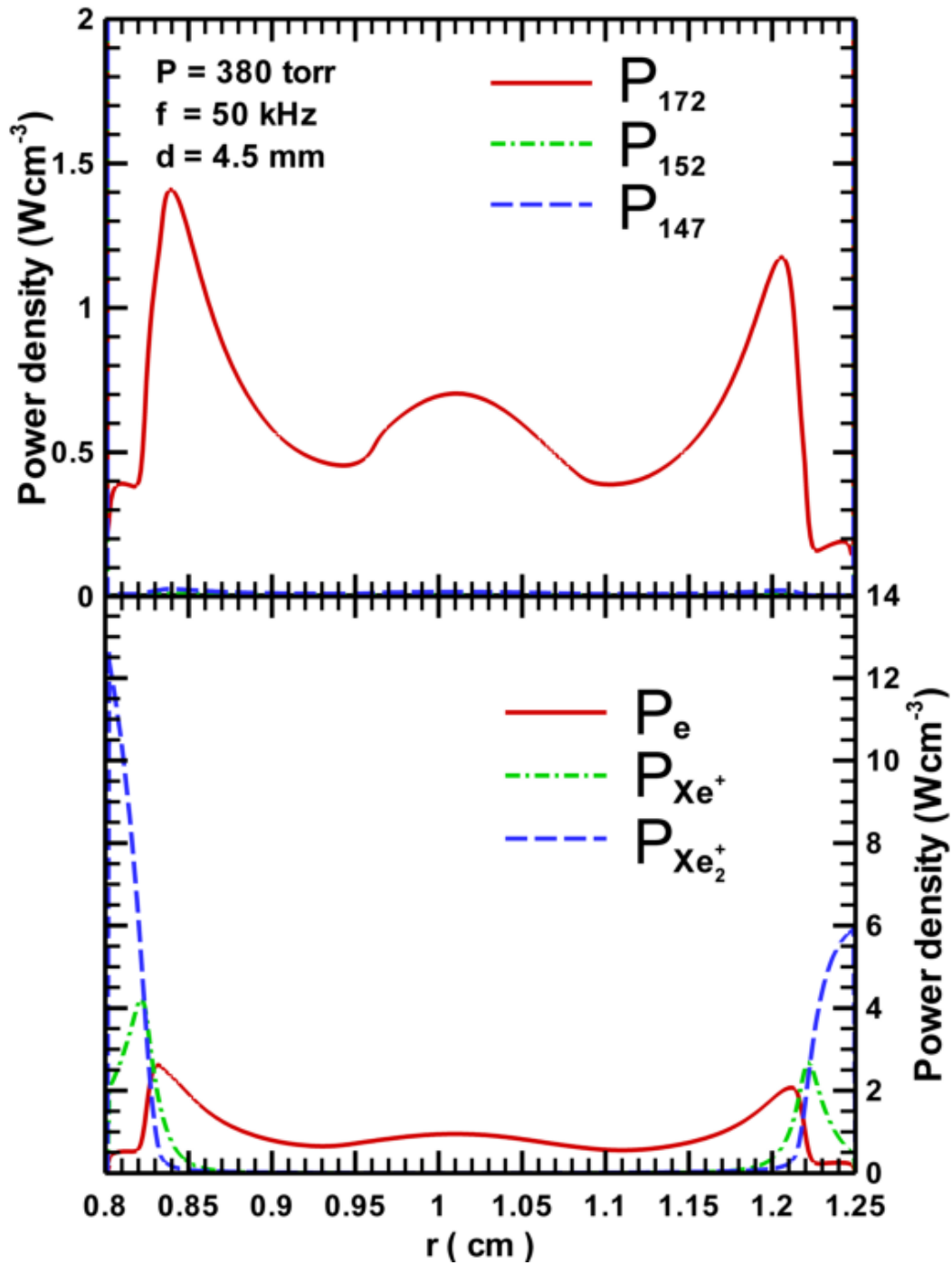


Figure 5-1 Spatial distribution of cycle averaged discharge properties: a) VUV light emissions across the gap b) power depositions of charged species across the gap.

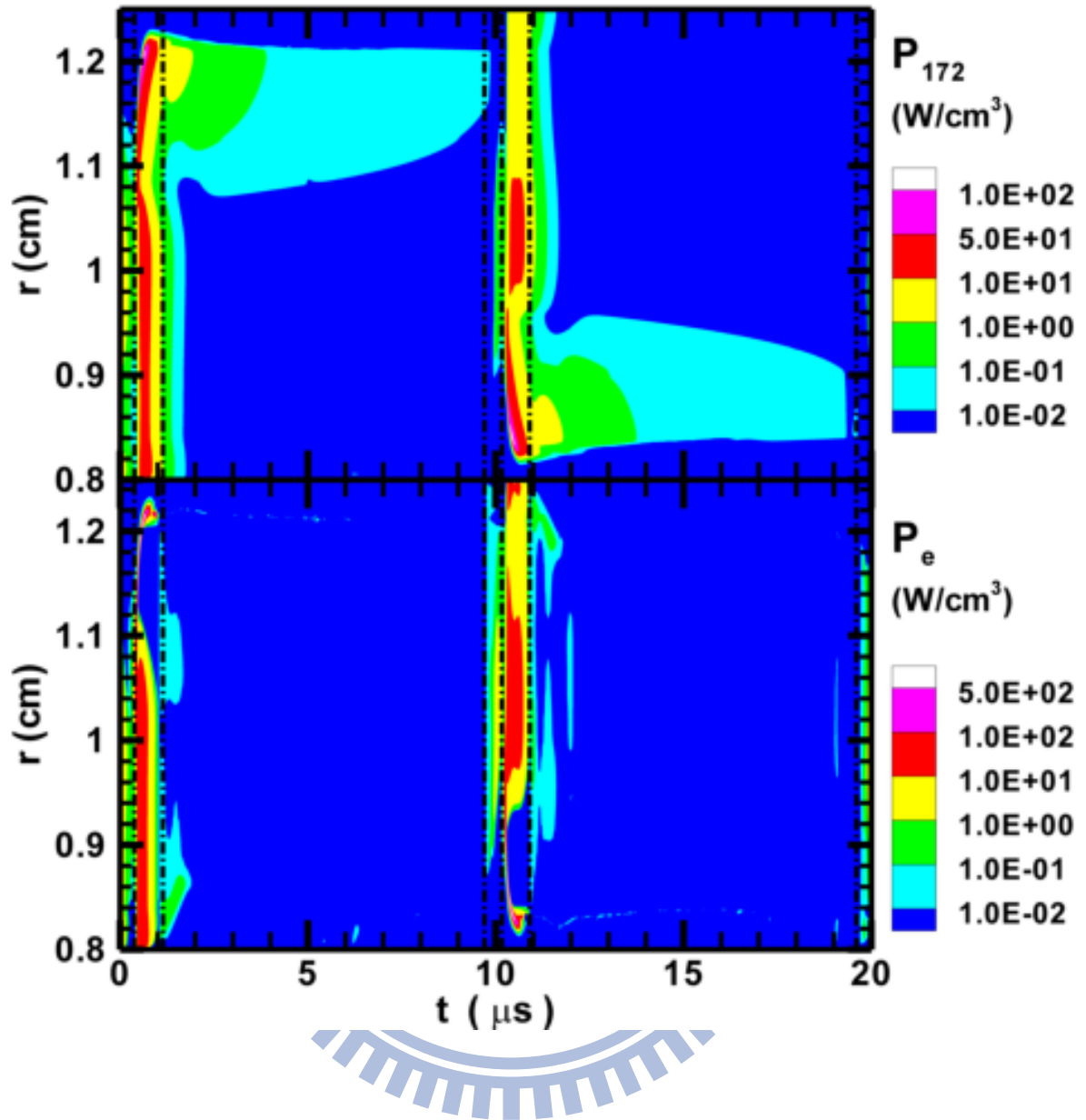


Figure 5-2 Spatiotemporal diagram of: a) 172 nm line UVU light emission and b) electron power deposition.

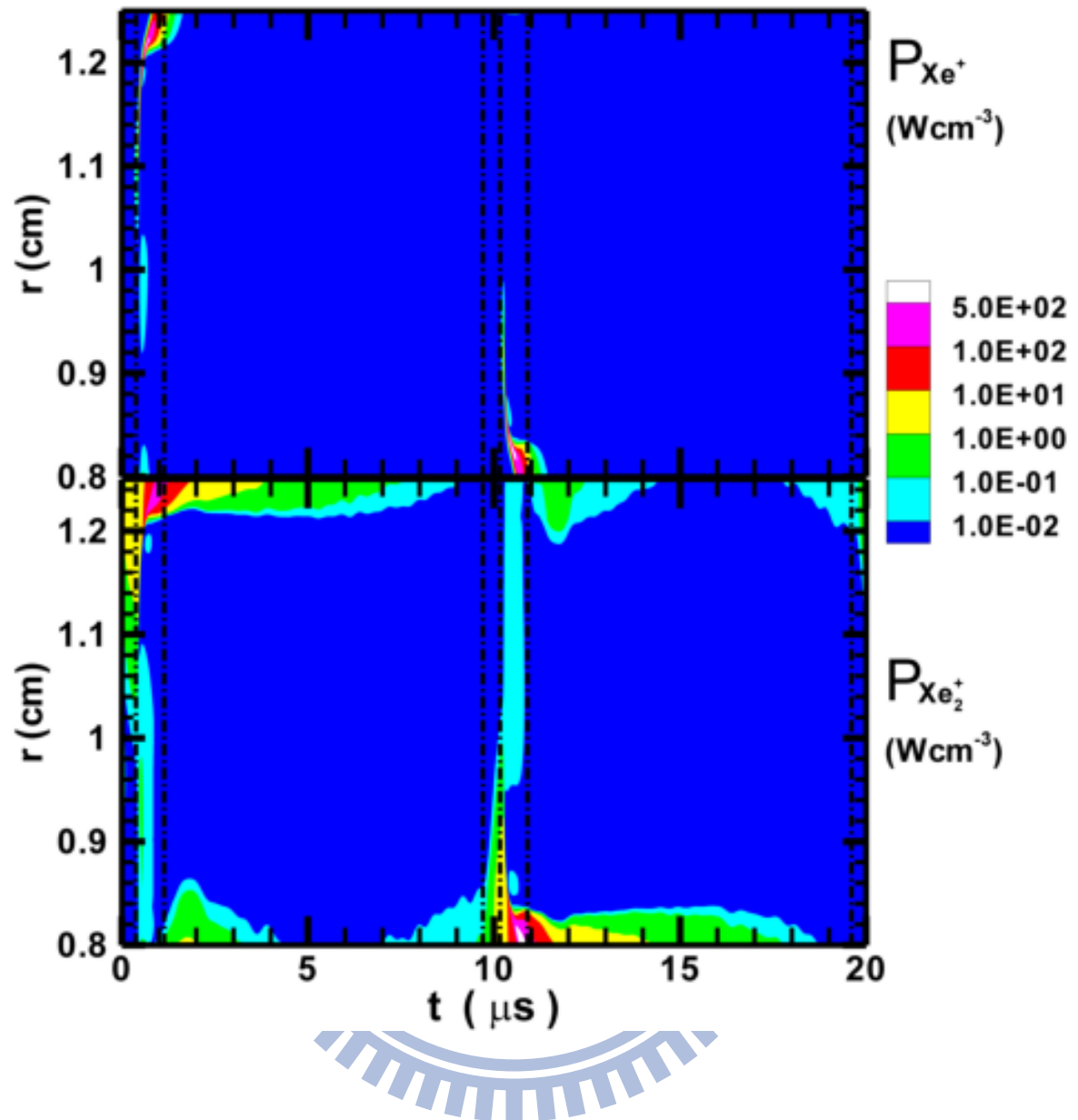
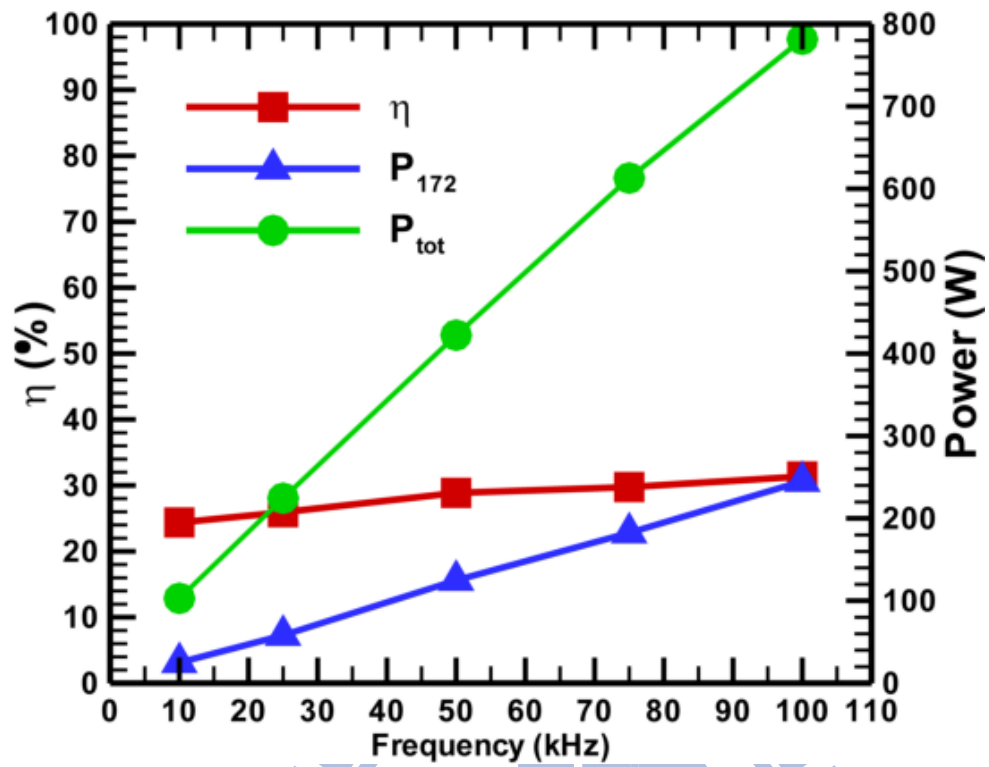
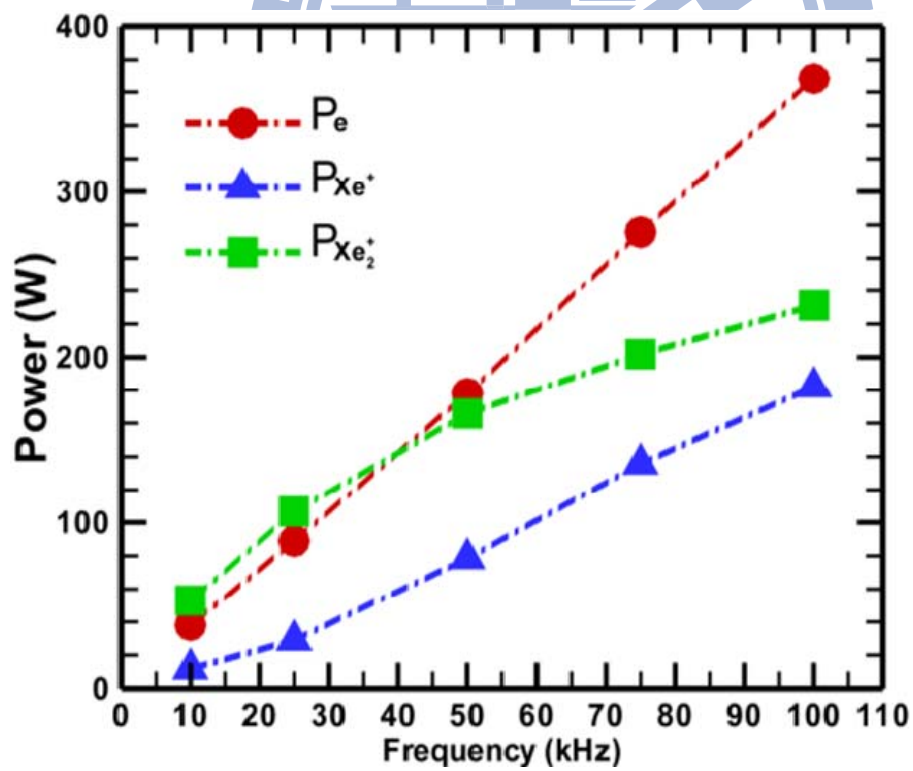


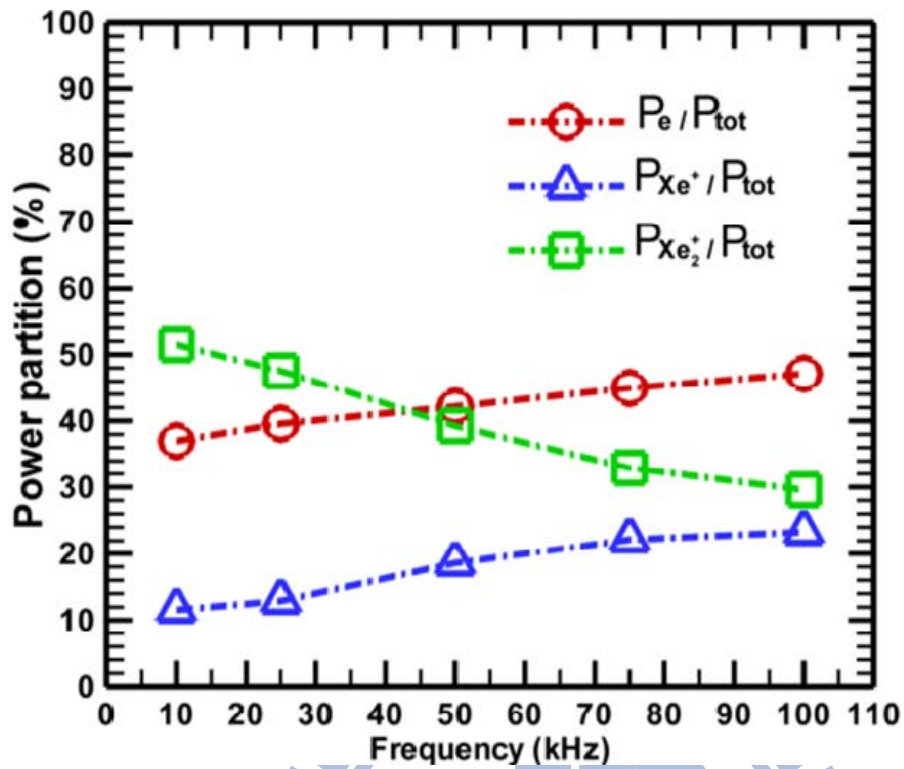
Figure 5-3 Spatiotemporal diagram of power depositions: a) atomic xenon ion and b) molecular xenon ion.



(a)

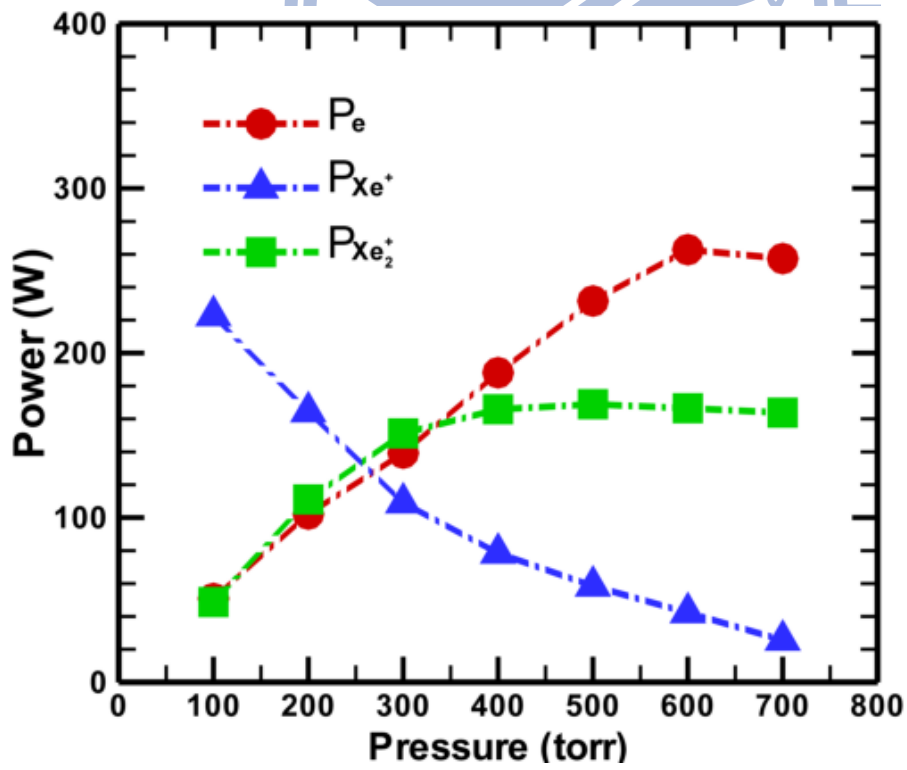
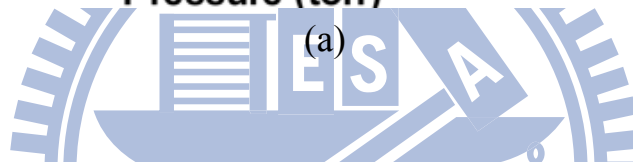
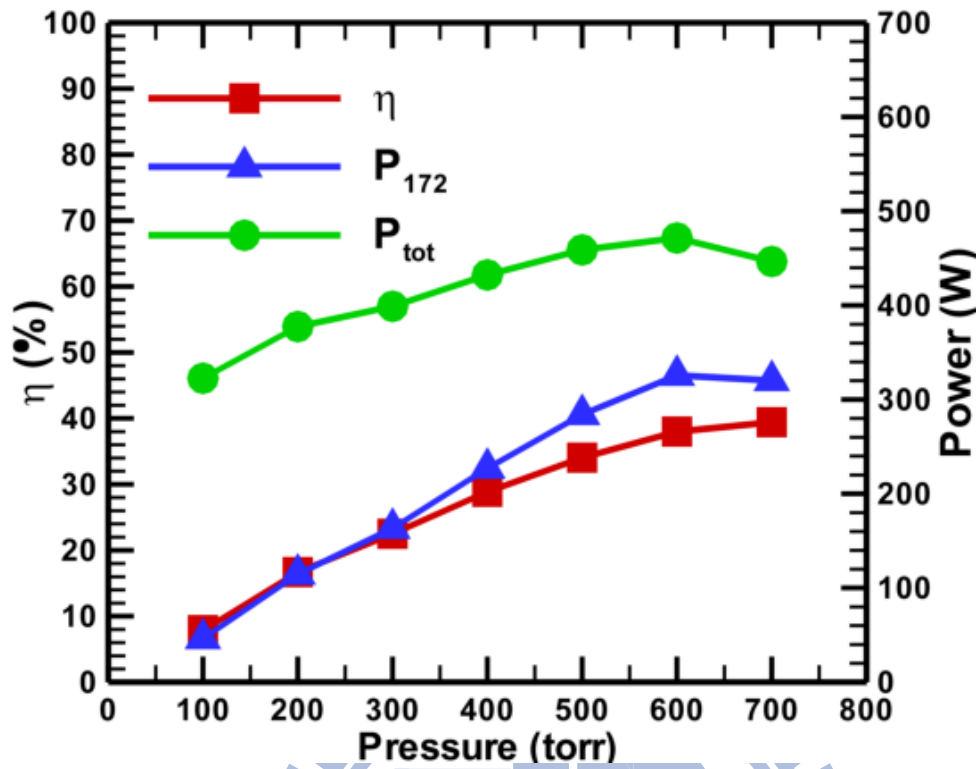


(b)

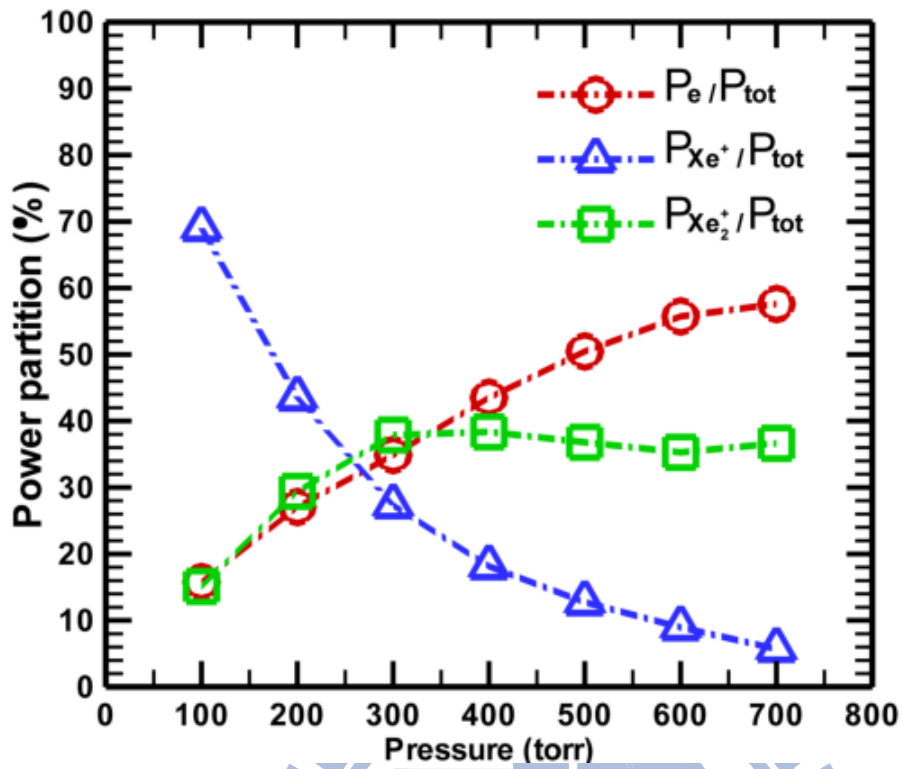


(c)

Figure 5-4 Effect of frequency on: a) η_{172} , P_{tot} and P_{172} , b) power deposition of various charged species, and c) fraction of power deposition for different charged species at 400 torr of gas pressure, 4.5 mm of gap distance and 2 dielectric layers.

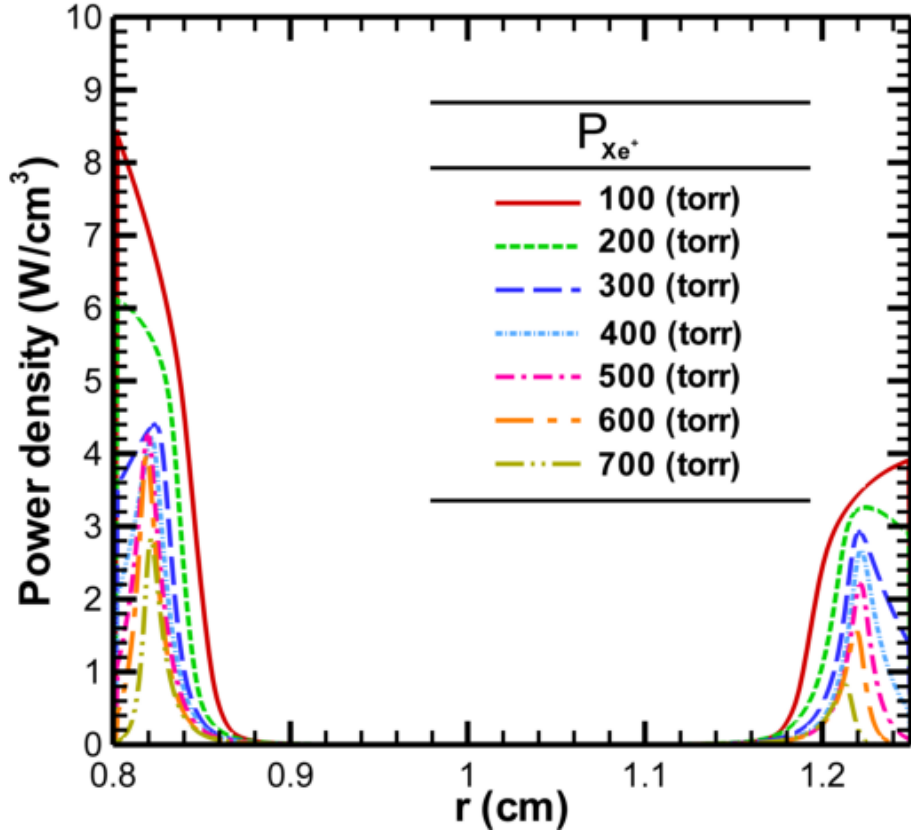
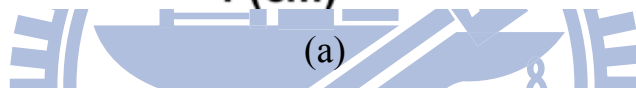
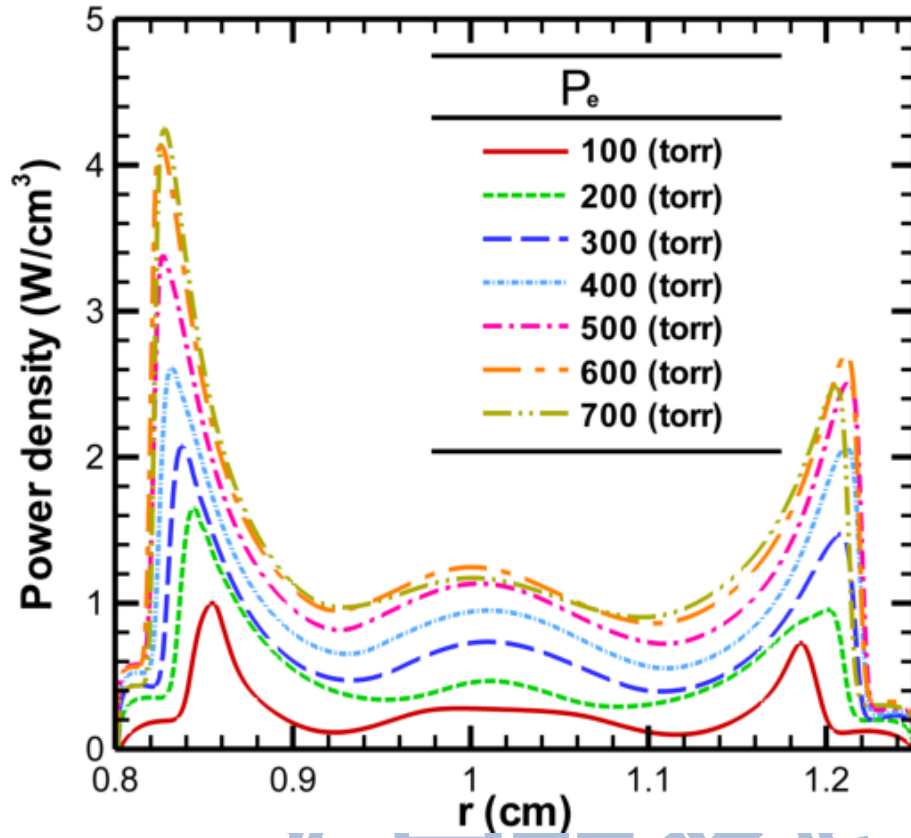


(b)

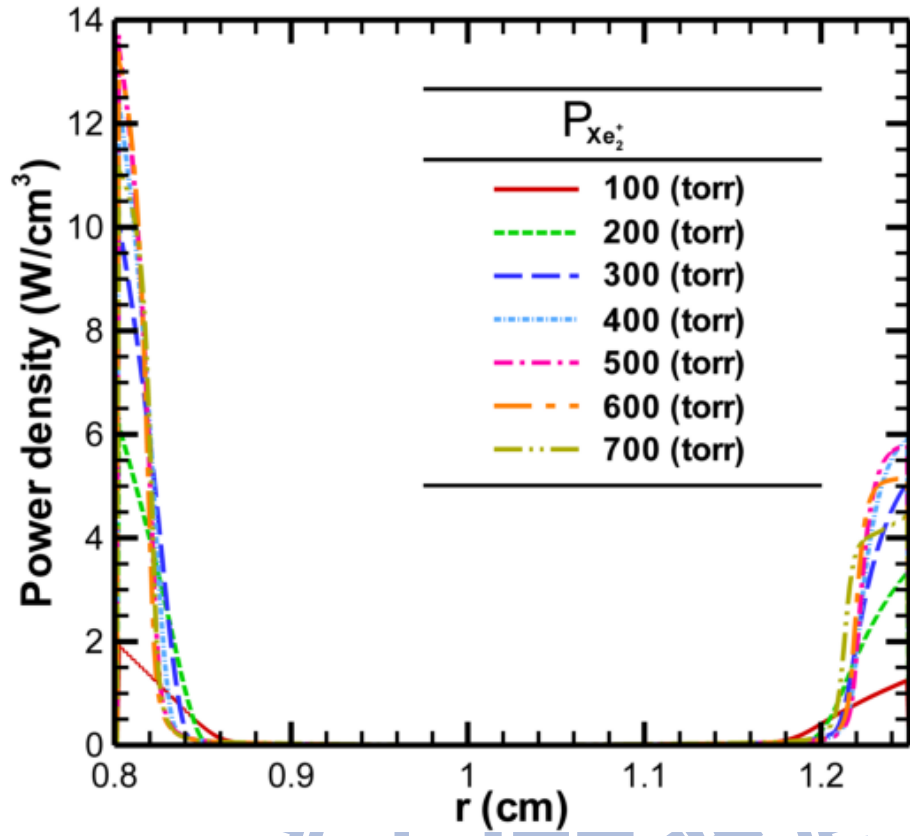


(c)

Figure 5-5 Effect of gas pressure on: a) η_{172} , P_{tot} and P_{172} , b) power deposition of various charged species, and c) fraction of power deposition for different charged species at 50 kHz of power source, 4.5 mm of gap distance and 2 dielectric layers.

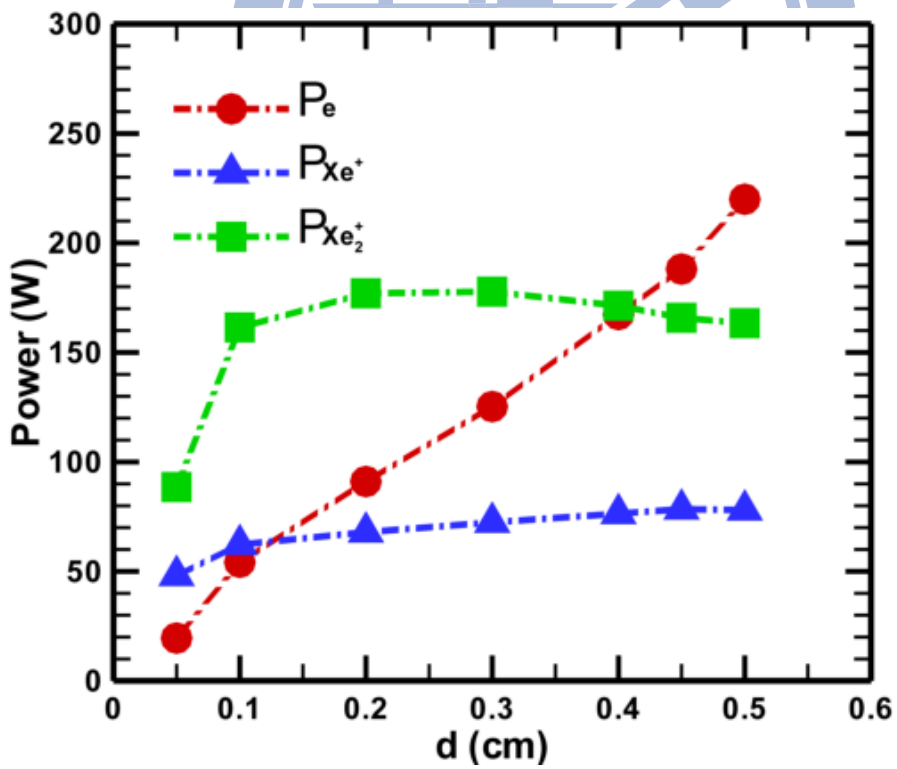
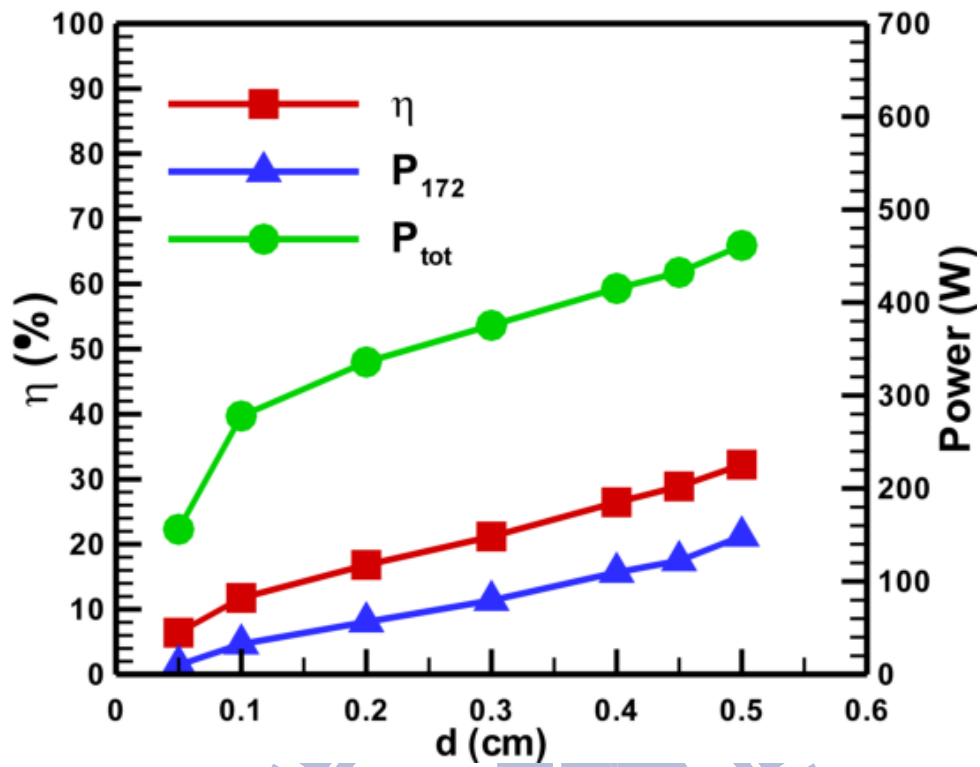


(b)

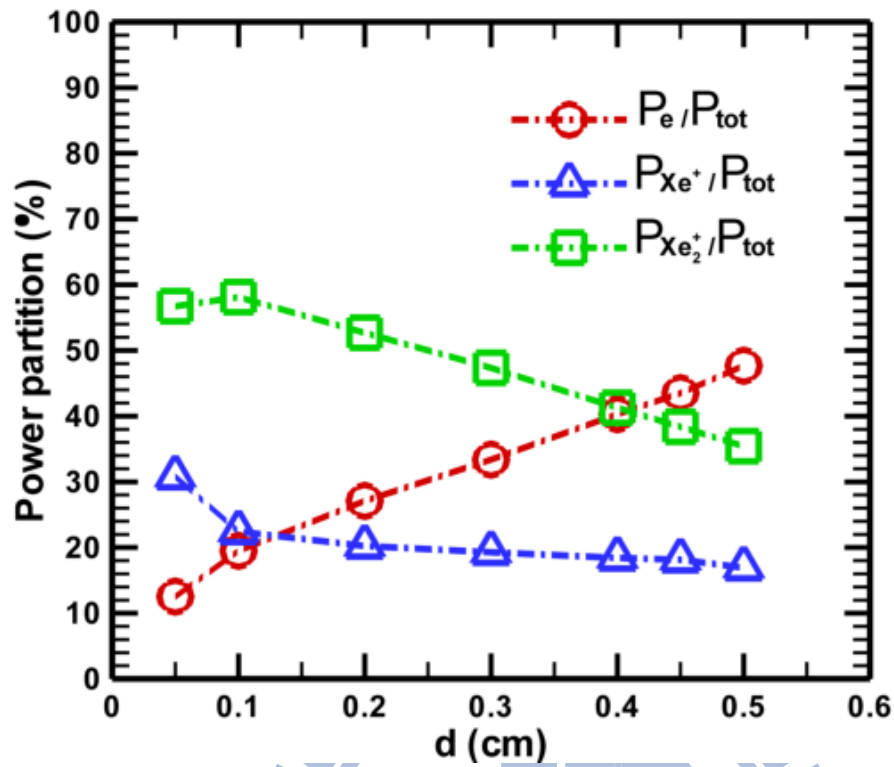


(c)

Figure 5-6 Spatial distribution of cycle-averaged power densities of various charged species at different gas pressures: a) electron, b) atomic xenon ion and c) molecular xenon ion.

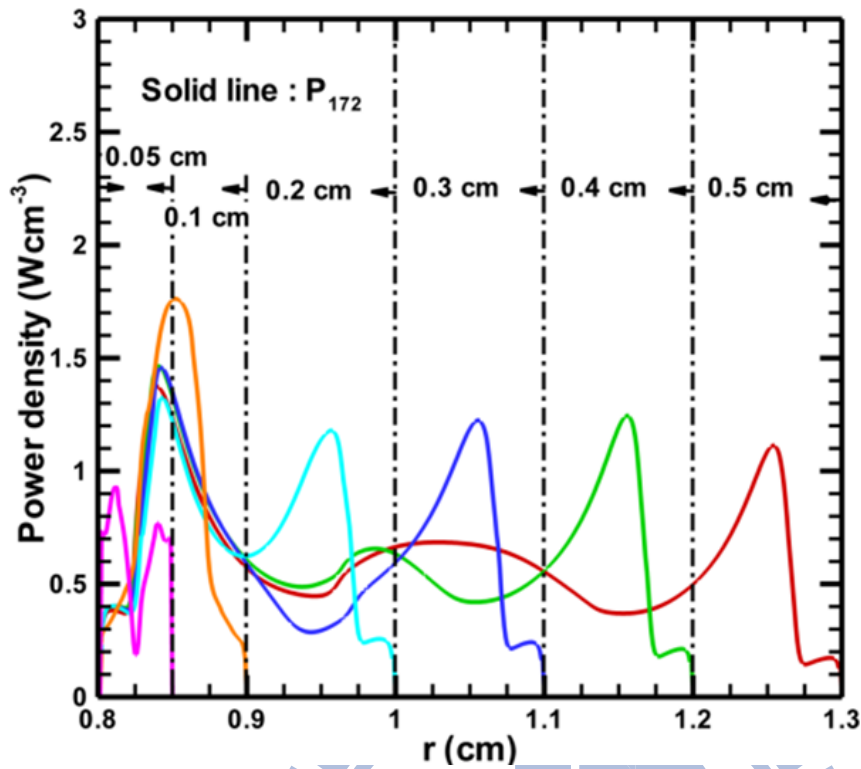


(b)

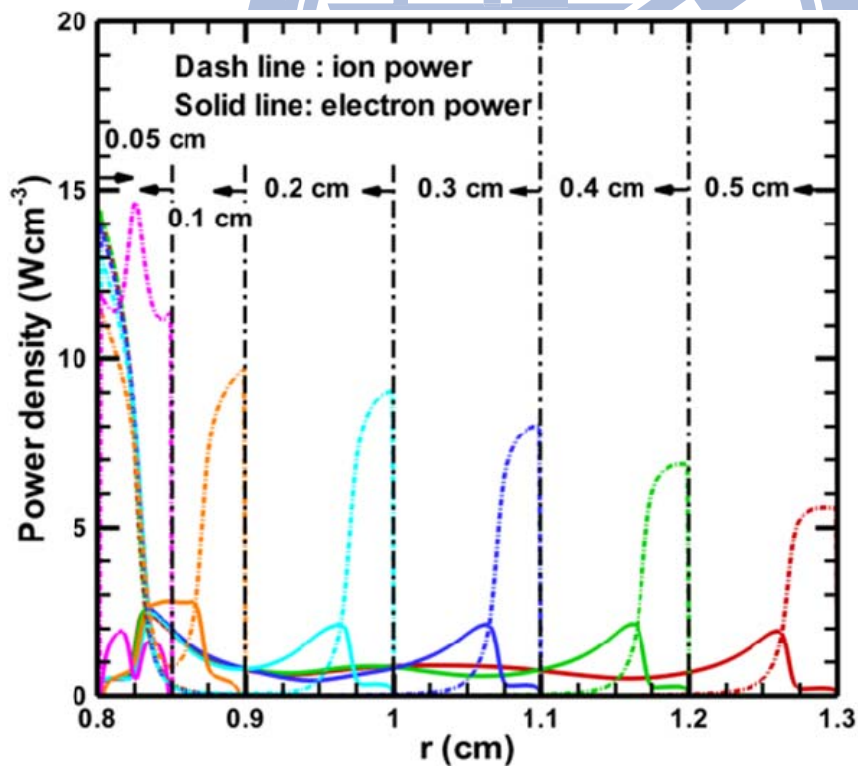


(c)

Figure 5-7 Effect of gap distance on: a) η_{172} , P_{tot} and P_{172} , b) power deposition of various charged species, and c) fraction of power deposition for different charged species at 50 kHz of power source, 400 torr of gas pressure and 2 dielectric layers.

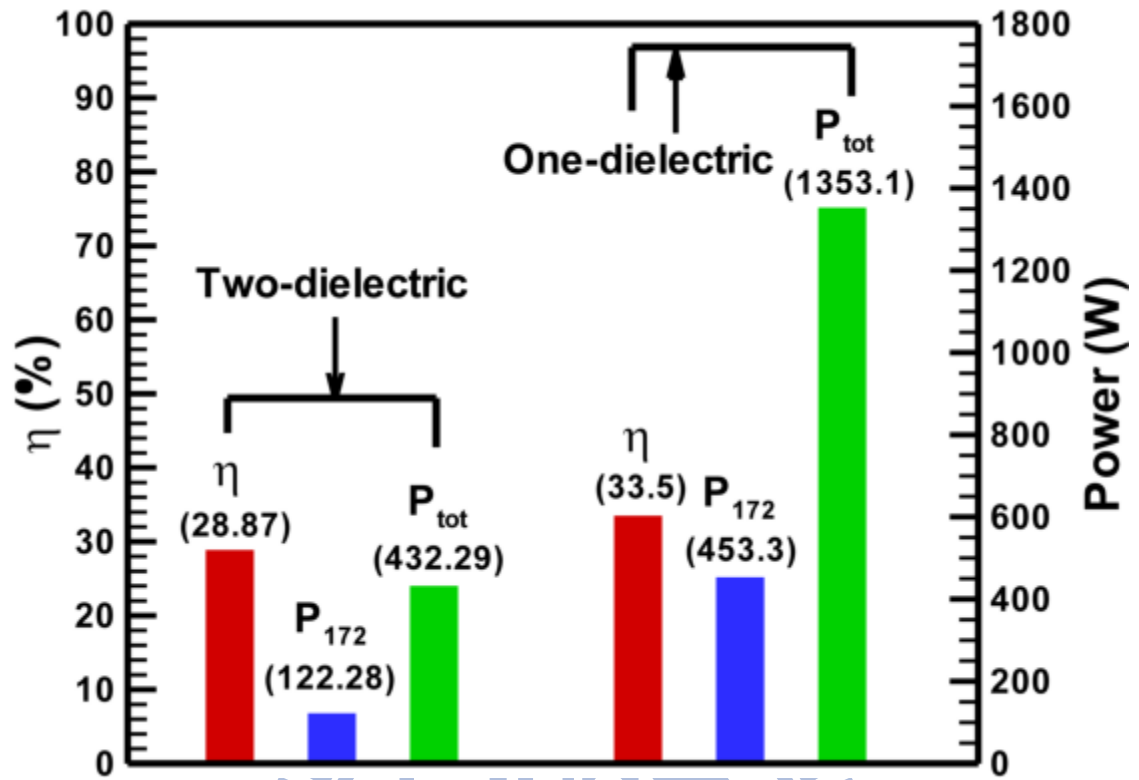


(a)

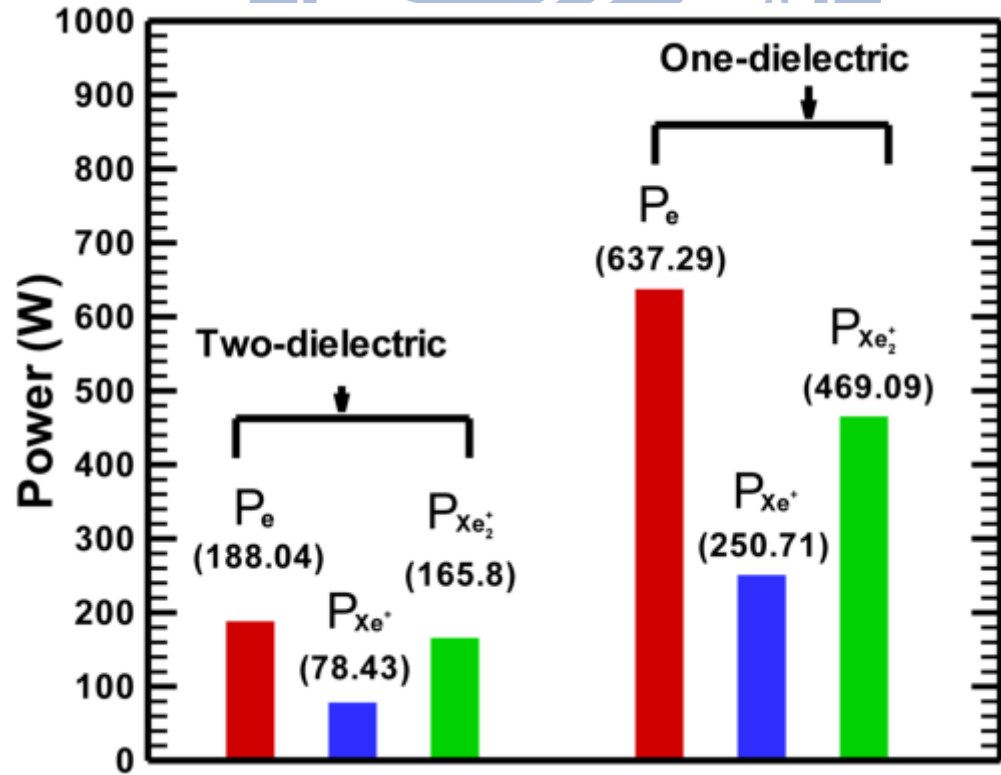


(b)

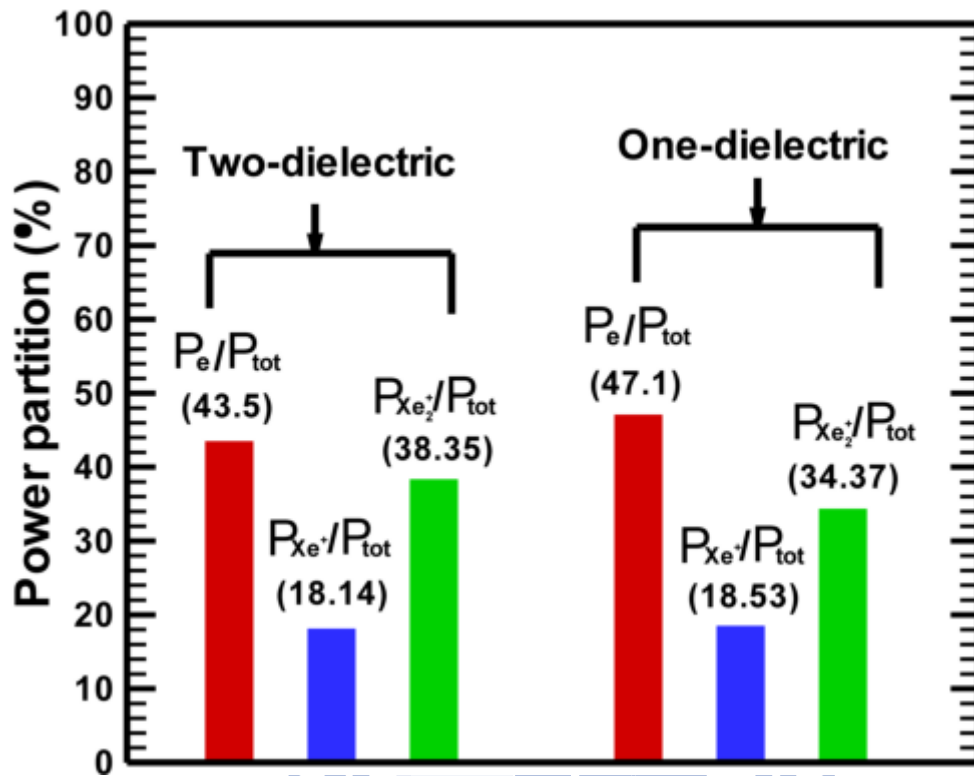
Figure 5-8 Spatial distribution of cycle-averaged power densities at different gap distances: a) VUC emission and b) ions and electron.



(a)

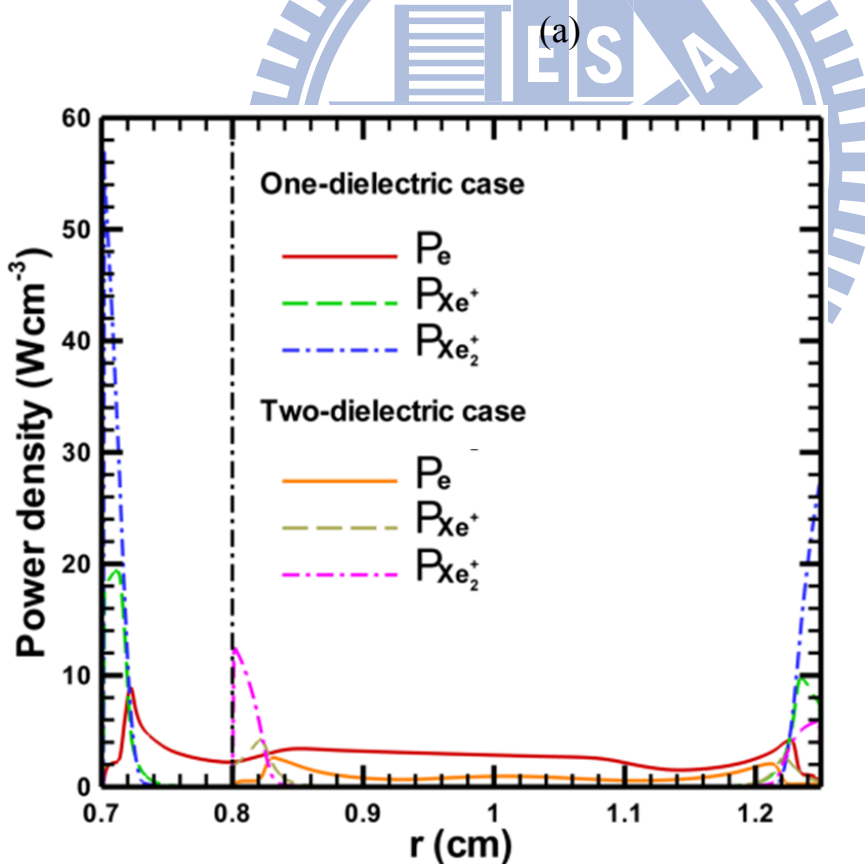
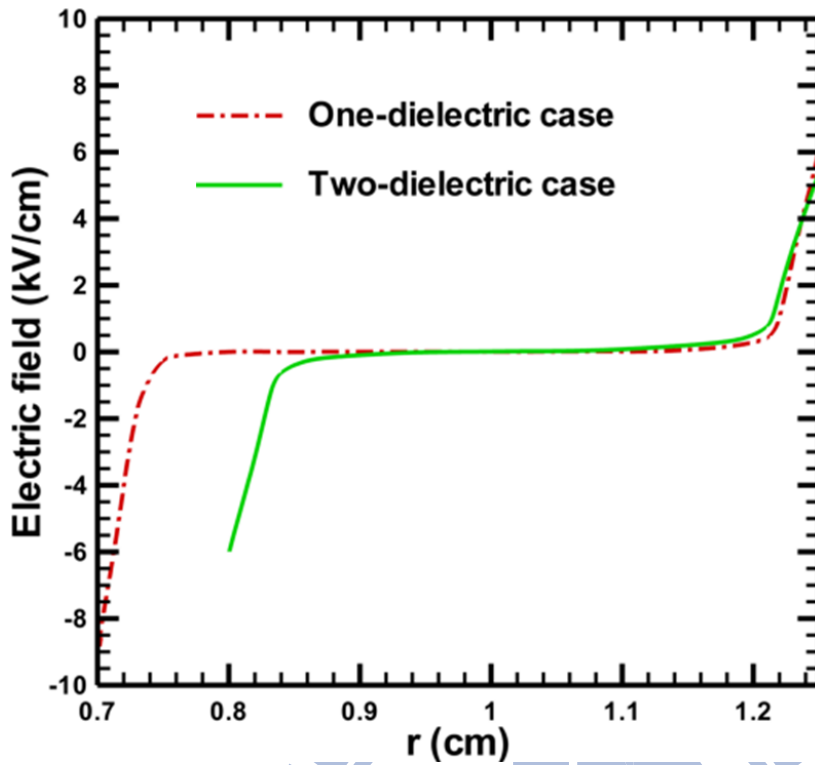


(b)



(c)

Figure 5-9 Effect of number of dielectric materials on: a) η_{172} , P_{tot} and P_{172} , b) power deposition of various charged species, and c) fraction of power deposition for different charged species at 50 kHz of power source, 400 torr of gas pressure and 4.5 mm of gap distance.



(b)

Figure 5-10 Spatial distribution of cycle averaged properties for one and two dielectric cases: a) electric field and b) power densities of charged species at 50 kHz of power source, 400 torr of gas pressure and 4.5 mm of gap distance.

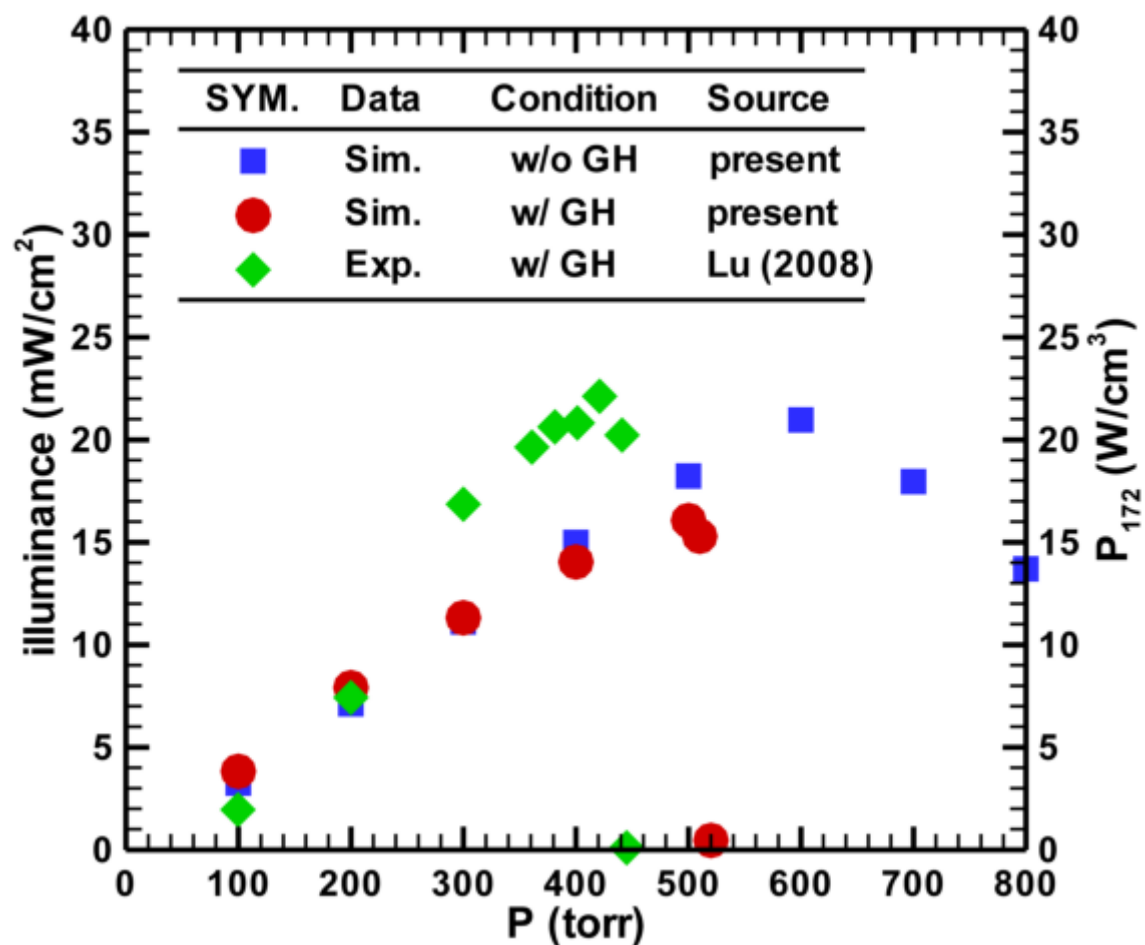


Figure 6-1 Comparison of the experimental and simulated data with and without gas heating.

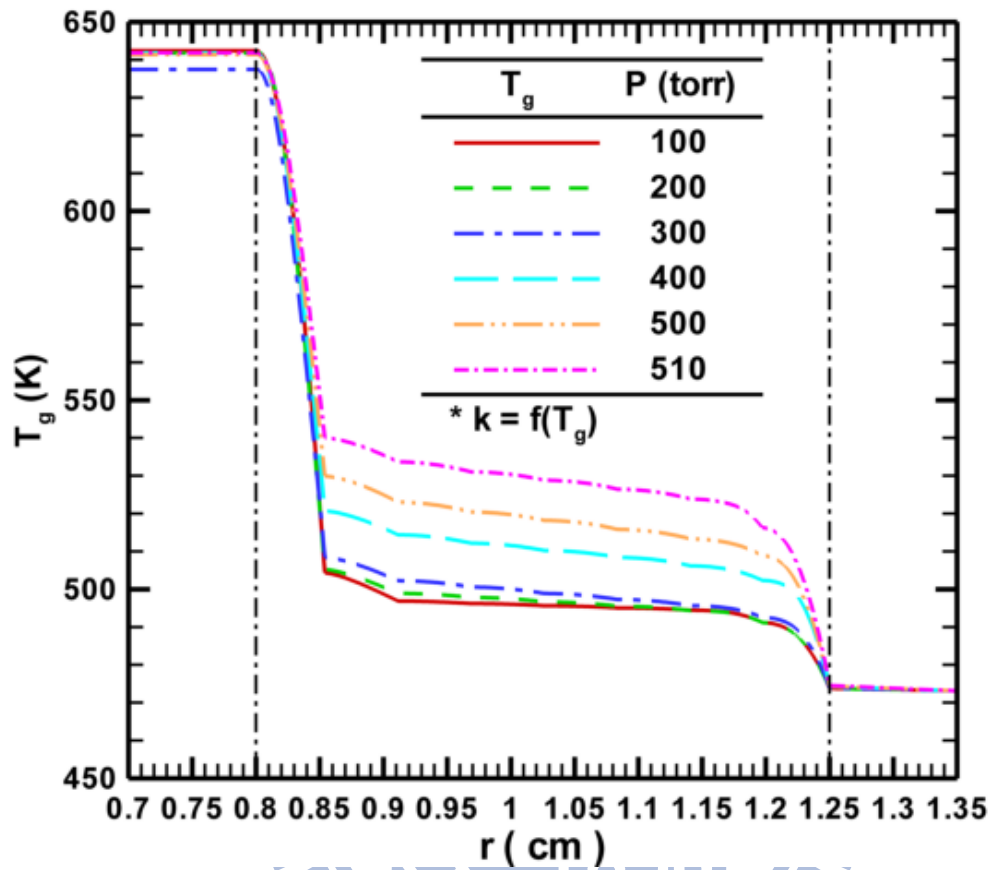


Figure 6-2 The spatial variations of background gas temperature (T_g) at different pressures across the discharge gap.

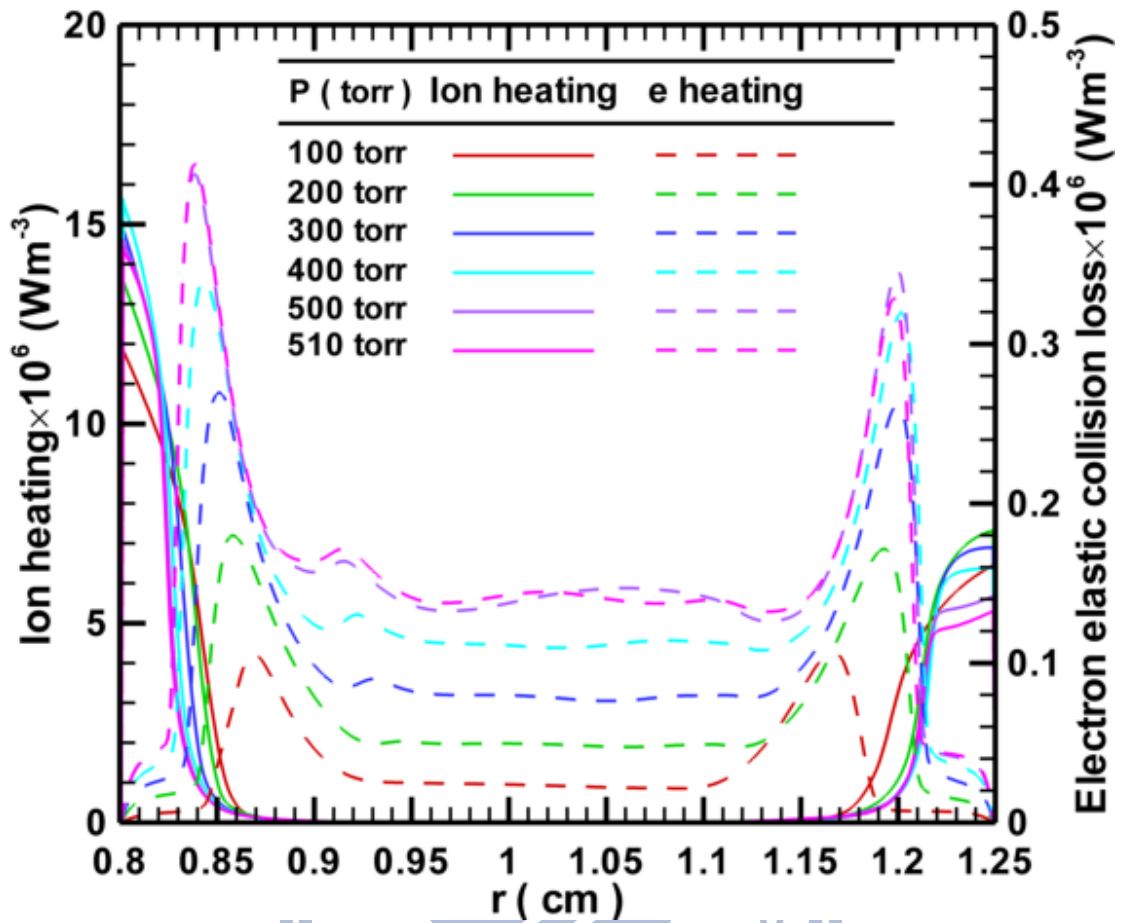
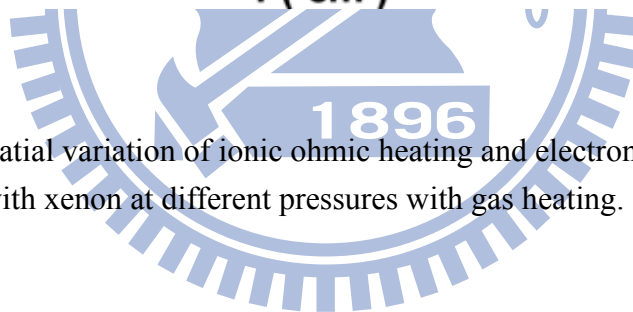


Figure 6-3 The spatial variation of ionic ohmic heating and electron energy loss due to elastic collision with xenon at different pressures with gas heating.



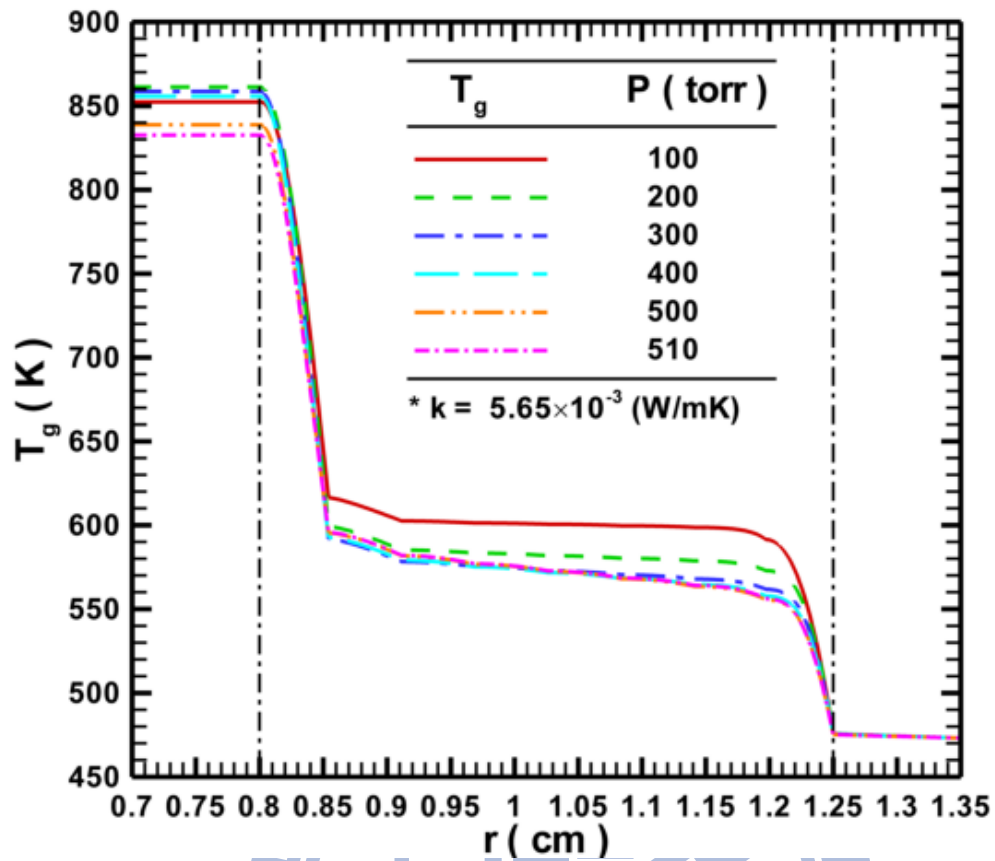
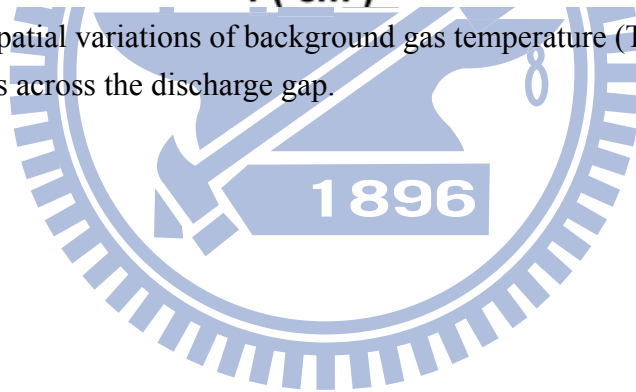


Figure 6-4 The spatial variations of background gas temperature (T_g) w/ $k = \text{const}$ at different pressures across the discharge gap.



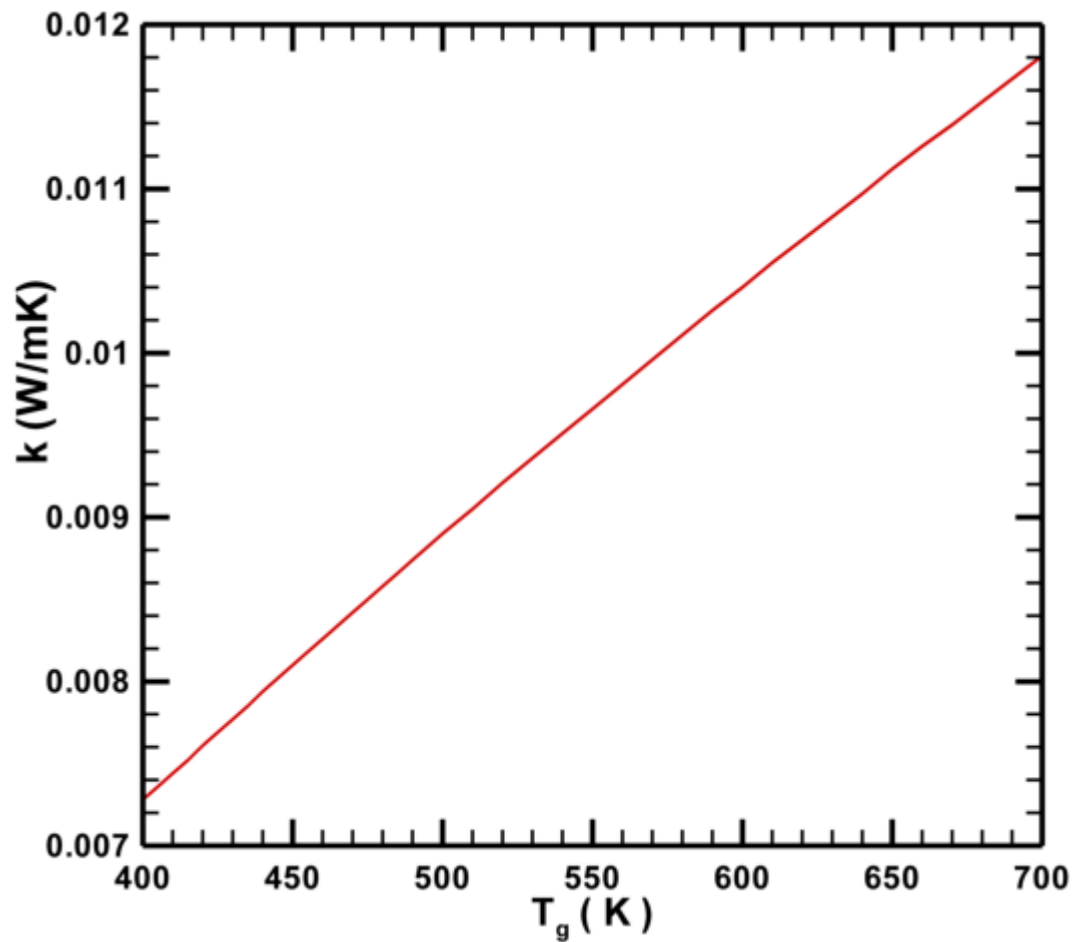


Figure 6-5 The variation of thermal conductivity in the region of $T_g = 400 - 700$.

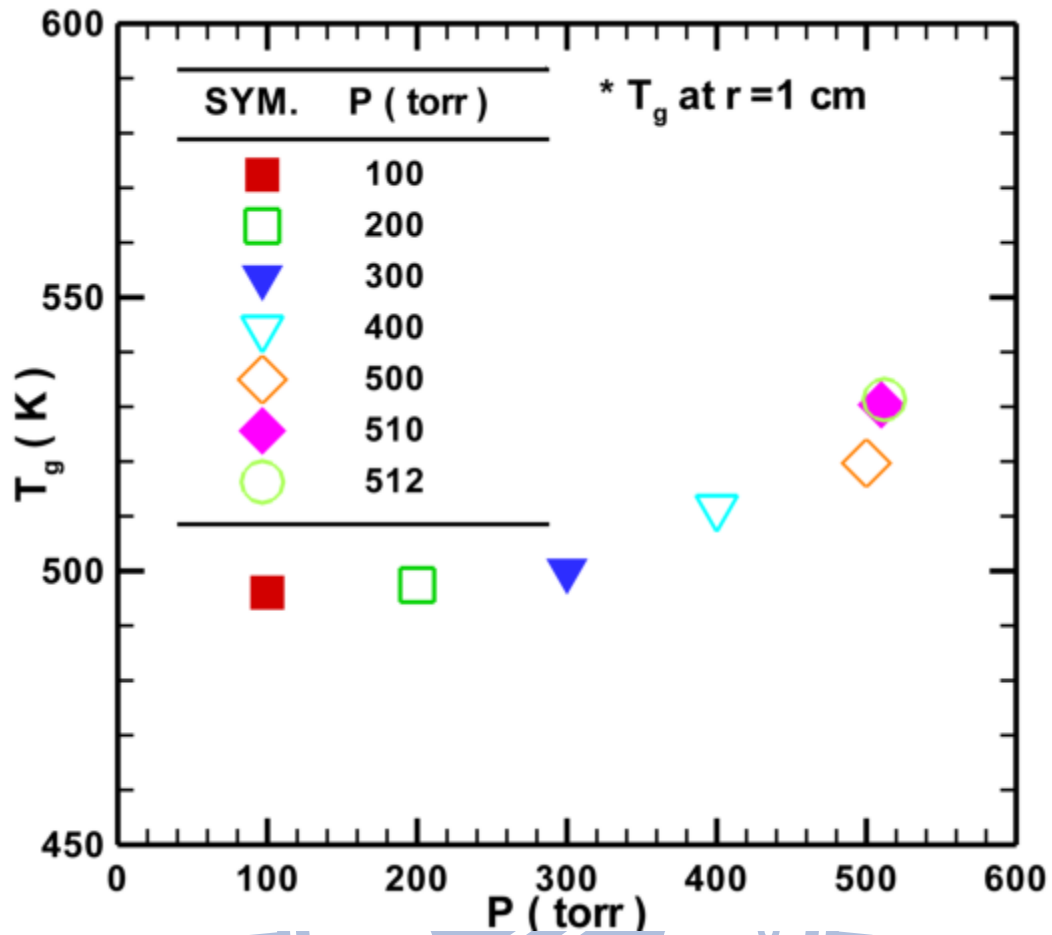


Figure 6-6 The distribution of T_g at $r=1$ cm in the region of 100 – 513 torr.

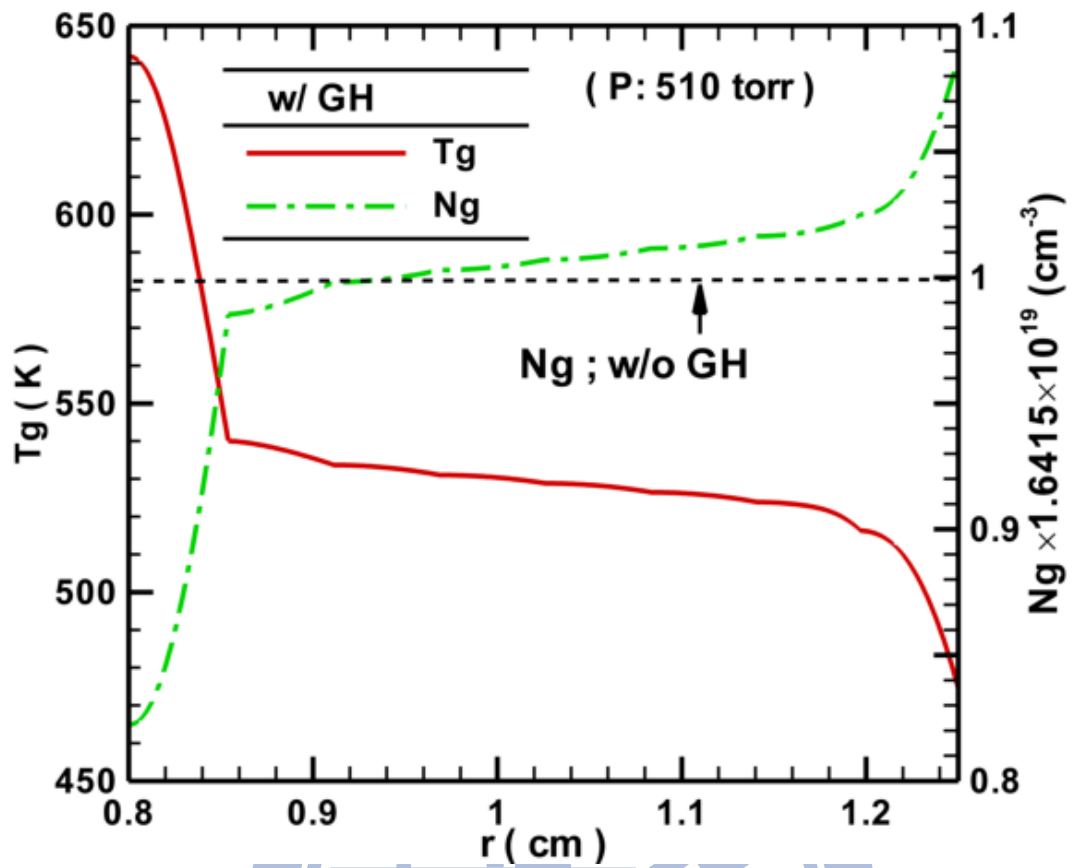


Figure 6-7 The spatial distribution of background gas temperature (T_g) and number density (N_g) at 510 torr across the discharge gap.

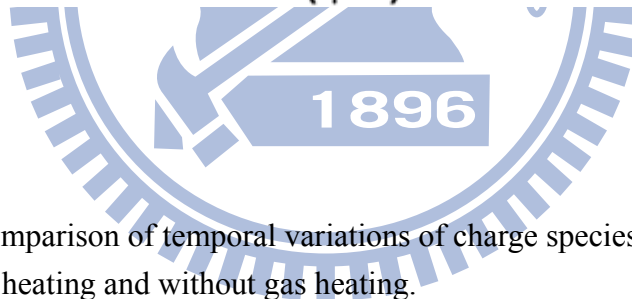
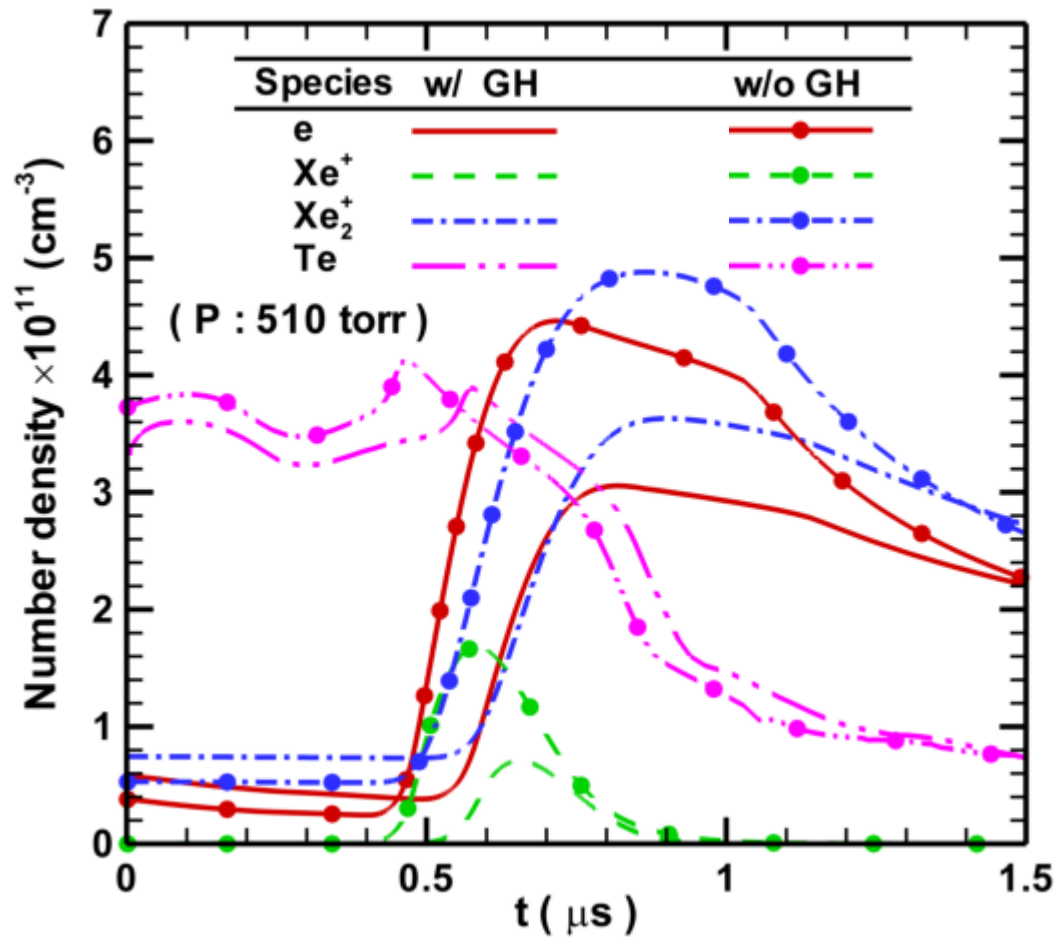


Figure 6-8 The comparison of temporal variations of charge species and T_e at 510 torr between with gas heating and without gas heating.

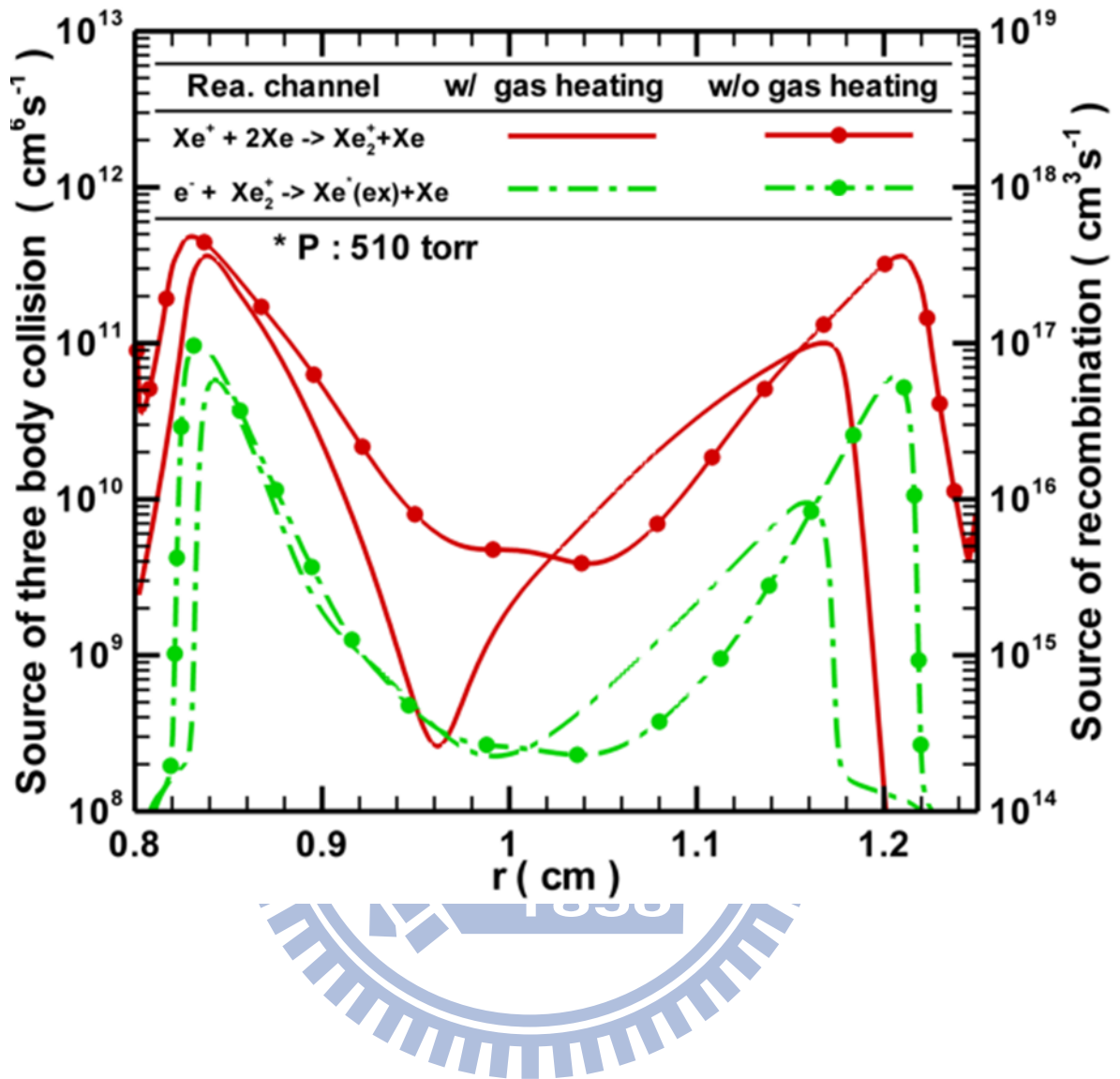


Figure 6-9 The comparison of spatial variations of Xe^+ -to- Xe_2^+ ion conversion and e-Xe_2^+ recombination at 510 torr between with and without gas heating.

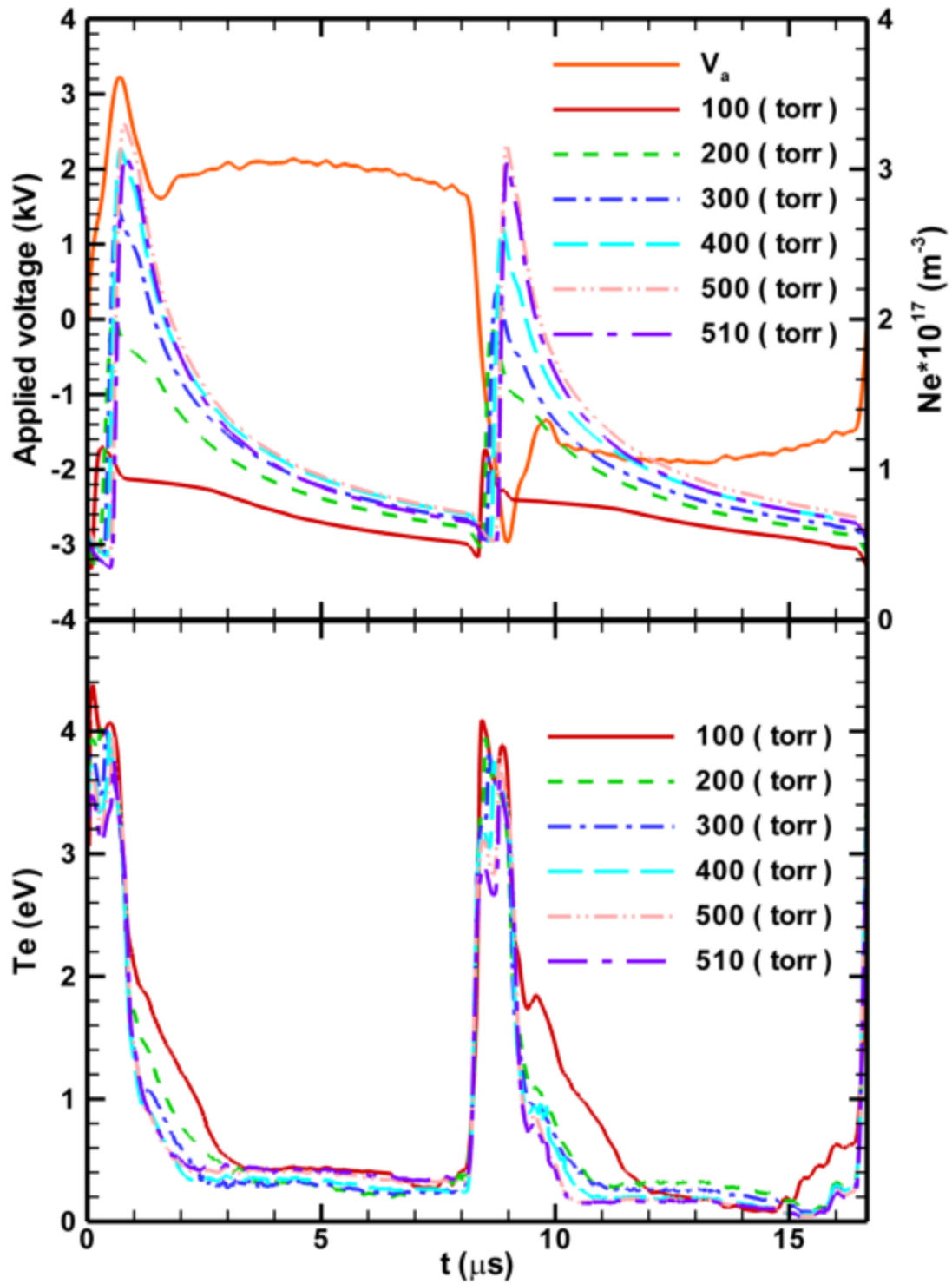


Figure 6-10 The temporal variations of a) applied voltage (V_a) and electron number density (N_e) b) electron temperature (T_e) in the range of $p=100-510$ torr over a cycle.

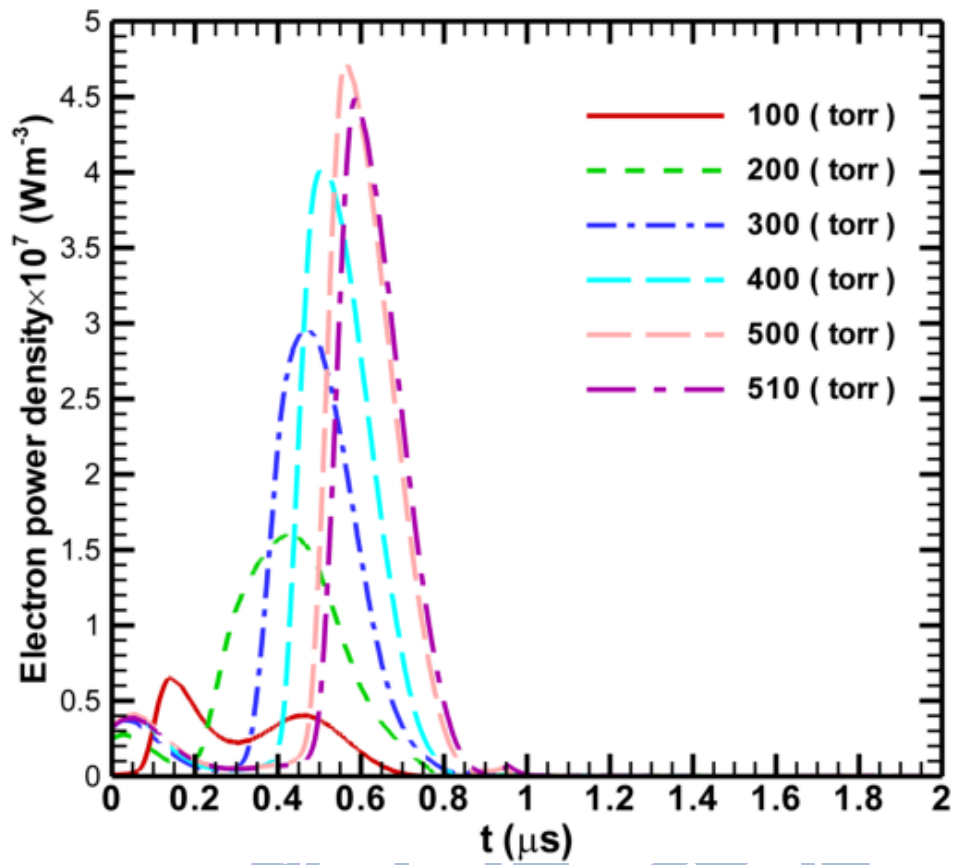
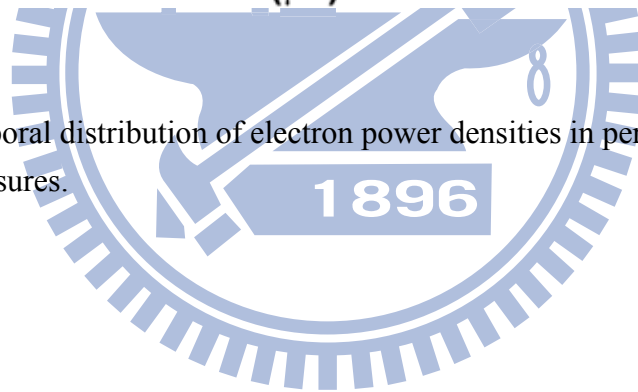


Figure 6-11 Temporal distribution of electron power densities in period 0-2 (μs) at different gas pressures.



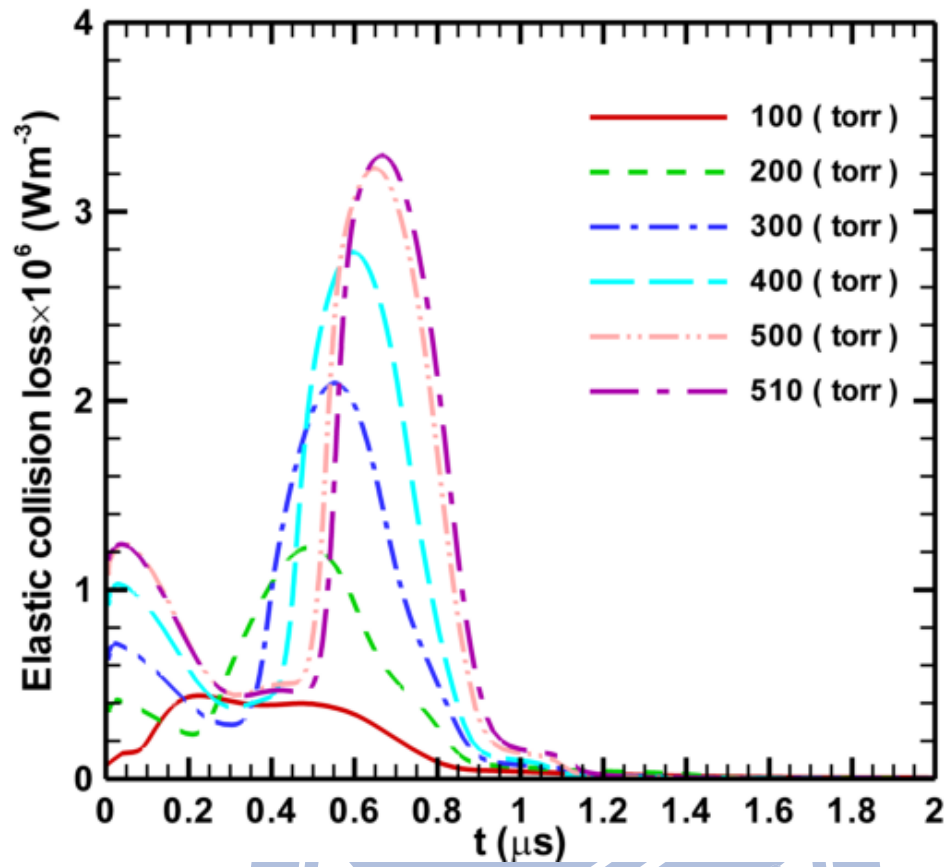
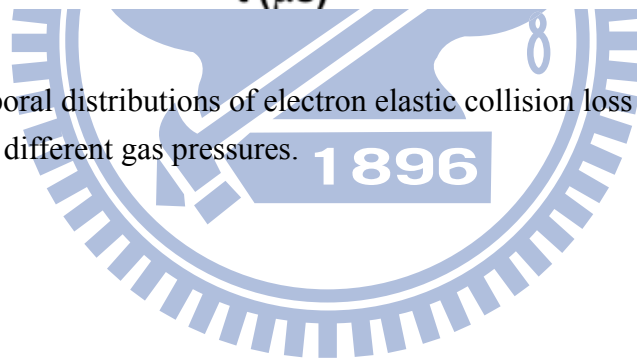


Figure 6-12 Temporal distributions of electron elastic collision loss power densities in period 0-2 (μs) at different gas pressures.



References

- [1] Avtaeva, S. V. and Kulumbaev, E. B., “Effect of the scheme of plasmachemical processes on the calculated characteristics of a barrier discharge in xenon,” Plasma physics reports, vol. 34, pp. 452-470, 2008.
- [2] Balay, S., Gropp, W. D., McInnes, L. C., and Smith, B. F., Petsc home page: <http://www.mcs.anl.gov/petsc/petsc-as/>, 2001
- [3] Beleznai, S., Mihajlik, G., Agod, A., Maros, I., Juhasz, R., Nemeth, Z., Jakab, L. and Richer, P., “High-efficiency dielectric barrier Xe discharge lamp: theoretical and experimental investigations,” J. Phys. D: Appl. Phys., vol. 39, pp. 3777-3787, 2006.
- [4] Belostotskiy, S. G. Donnelly, V. M. and Economou, D. J., “Influence of gas heating on high pressure dc microdischarge I–V characteristics,” Plasma Sources Sci. Technol., vol. 17, pp. 045018, 2008.
- [5] Benmoussa, A., H. Si-Sabeur, Harrache, Z. and Belasri, A., “Study of gas heating in a xenon glow discharge,” Plasma deices and operations, vol. 15 pp. 299-304, 2007.
- [6] Boeuf, J. P. and Pitchford, L. C., “Two-dimensional model of a capacitively coupled rf discharge and comparisons with experiments in the Gaseous

- Electronics Conference reference reactor,” Phys. Ref. E, vol. 51 , pp. 1376-1390, 1995.
- [7] Bogaerts, A., Gijbels, R. and Serikov, V. V., “Calculation of gas heating in direct current argon glow discharges,” J. Appl. Phys., vol. 87, pp. 8334-8344, 2000.
- [8] Bogdanov, E. A., kudryavtsev, A. A., Arslanbekov, R. R. and Kolobov, V. I., “Simulation of pulsed dielectric barrier discharge xenon excimer lamp,” J. Phys. D: Appl. Phys., vol. 37, pp. 2987-2995, 2004.
- [9] Buck, C. K., Pedraza, A. J., Benson, R. S. and Park, J. W., “VUV-light-induced deposited silica films,” Nucl. Instrum. Methods Phys. Res. B, vol. 141, pp. 675-678, 1998.
- [10] Cai, X. C., Casarin, M. A., Elliott, F. W. and Widlund, O.B., *Contemporary Mathematics*, pp. 391–399, American Mathematical Society, 1998.
- [11] Carman, R. J. and Mildren, R. P., “Computer modeling of a short-pulse excited dielectric barrier discharge xenon excimer lamp ($\lambda \sim 172$ nm),” J. Phys. D: Appl. Phys., vol. 36, pp. 19-33, 2003.
- [12] Chirokov, A., Gutsol, A. and Fridman, A., “Atmospheric pressure plasma of dielectric barrier discharges,” Pure Appl. Chem., Vol. 77, pp. 487-495, 2005.
- [13] Echigo S, Yamada H, Matsui, S., Kawanishi, S. and Shishida, K., “Comparison between O₃/VUV, O₃/H₂O₂, VUV and O₃ processes for the decomposition of

- organophosphoric acid trimesters,” *Water Sci. Technol.*, vol. 34 , pp. 81-88, 1996.
- [14] Eliasson, B. and Kogelschatz, U., *Appl. Phys. B*, “UV excimer radiation from dielectric-barrier discharges,” vol. 46, pp. 299-303, 1998.
- [15] Gellert, B. and Kogelschatz, U., “Generation of excimer emission in dielectric barrier discharges,” *Appl. Phys. B*, vol. 52, pp. 14-21, 1991.
- [16] Hagelaar, G., “BOLSIG+ : user-friendly solver for electron Boltzmann equation.”, <http://www.siglo-kinema.com/>.
- [17] Hanley, H. J. M., “The Viscosity and Thermal Conductivity Coefficients of Dilute Argon, Krypton, and Xenon,” *J. Phys. Chem. Ref. Data*, vol. 2, pp. 619-642, 1973.
- [18] Hung, C. T., “Development of a Parallel Fluid Modeling Code and Its Applications in Low-temperature Plasmas,” PhD. Thesis, Department of Mechanical Engineering, National Chiao Tung University, Hsinchu, Taiwan, 2010.
- [19] Ivanov, V. V., Mankelevich, Yu. A., Proshina, O. V., Rakhimov, A. T., and Rakhimova, T. V., “Modeling of a repetitive discharge in the cell of a plasma display panel,” *Plasma Physics Reports*, vol. 25, pp. 591-598, 1999.

- [20] Jou, S. Y., Hung, C. T., Chiu, Y. M., Wu, J. S., Wei, B. Y., "Simulation of Excimer Ultraviolet (EUV) Emission from a Coaxial Xenon Excimer Ultraviolet Lamp Driven by Distorted Bipolar Square Voltages," *Plasma Chem Plasma Process*, vol. 30, pp. 907-931, 2010.
- [21] Kane, D. M., Hirschausen, D., Ward, B. K., Carman, R. J. and Mildren, R. P., "Pulsed VUV sources and their Application to Surface Cleaning of Optical Materials," *Proc. SPIE*, vol. 5399, pp. 100-106, 2004.
- [22] Kogelschatz, U., Eliasson, B. and Egli, W., "From ozone generators to flat television screens: history and future potential of dielectric-barrier discharges*," *Pure Appl. Chem.*, vol. 71, pp. 1819-1828, 1999.
- [23] Kogelschatz, U., Esrom, H., Zhang, J. Y. and Boyd, I. W., "High-intensity sources of incoherent UV and VUV excimer radiation for low-temperature materials processing," *Appl. Surf. Sci.*, vol. 168, pp. 29-36, 2000.
- [24] Loeb, L., *Basic Processes of Gaseous Electronics*, University of California Press, Berkeley, 1960.
- [25] Lu, Z. L., "Parametric study of UV emission of a xenon excimer discharge barrier discharge," MS. Thesis, Department of Mechanical Engineering, National Chiao Tung University, Hsinchu, Taiwan, 2008.
- [26] Meek, J. M. and Craggs J. D., *Electrical Breakdown of Gases*, Wiley, N.Y, 1978.

- [27] Meunier, J., Belenguer, Ph., and Boeuf, J. P., “Numerical Model of an AC Plasma Display Panel Cell in Neon-Xenon Mixtures,” J. Appl. Phys., vol. 78, pp. 731-745, 1995.
- [28] Oda , A., Sakai, Y., Akashi, H. and Sugawara, H., J. Phys. , “One-dimensional modelling of low-frequency and high-pressure Xe barrier discharges for the design of excimer lamps,” D: Appl. Phys., vol. 32, pp. 2726-2736, 1999
- [29] Oda, A., Sugawara,H., Sakai, Y. and Haruaki, A., “Estimation of the light output power and efficiency of Xe barrier discharge excimer lamps using a one-dimensional fluid model for various voltage waveforms,” J. Phys. D: Appl. Phys., vol.33, pp. 1507-1513, 2000.
- [30] Park, J. H., Lee, I. K., Cho, B. H., Lee, J. K. and Whang, K. W., “High Efficiency Inverter Systems for Driving Mercury – Free Flat Fluorescent Lamps,” Power Conversion Conference, Nagoya, pp. 717-720, 2007.
- [31] Punset, C., Boeuf, J. P., and Pitchford, L. C., “Two-dimensional simulation of an alternating current matrix plasma display cell: Cross-talk and other geometric effects,” J. Appl. Phys., vol. 83, pp. 1884-1897, 1998.
- [32] Raether, H., *Electron Avalanches and Breakdown in Gases*, Butterworth, London, 1964.
- [33] Raizer, Y. P., *Gas Discharge Physics*, Springer, Berlin, Heidelberg, N. Y, 1991.

- [34] Revel, I., Pitchford, L. C. and Boeuf, J. P., "Calculated gas temperature profiles in argon glow discharges," J. Appl. Phys. Vol. 88, pp. 2234, 2000.
- [35] Saad, Y. and Schultz, M. H., "GMRES: A generalized minimal residual algorithm for solving nonsymmetric linear systems," SIAM J. Sci. Stat. Comput., vol. 7, pp. 856–869, 1986.
- [36] Safta, E., US Patent 6767458, 2004.
- [37] Serikov, V. V. and Nanbu, K., "The analysis of background gas heating in direct current sputtering discharges via particle simulation," J. Appl. Phys., vol. 82, pp. 5948-5957, 1997.
- [38] Shiga, T., Mikoshiba, S., Shinada, S., "Mercury-Free, High-Luminance and High-Efficacy Flat Discharge Lamp for LCD Backlighting," Elec. and Comm. in Japan, vol. 84 pp. 55-63, 2001.
- [39] Stockwald, S, and Neiger, M., "Some Properties of a Novel Far UV Xenon Excimer Barrier Discharge Light Source," Contrib. Plasma Phys., vol. 35, pp. 15-22, 1995.
- [40] Tanaka, Y. J., "Continuous Emission Spectra of Rare Gases in the Vacuum Ultraviolet Region," Opt. Soc. Am., vol. 45, pp 710-713, 1955.
- [41] Veerasingam, R., Campbell, R. B., and McGrath, R. T., "One-dimensional fluid simulations of a helium-xenon filled ac colour plasma flat panel display pixel,"

Plasma Sources Sci. Technol., vol. 6, pp. 157-169, 1997.

[42] Vollkommer, F. and Hitzschke, L., US Patent 5604410, 1997.

[43] Zang, J. Y. and Boyd, I. W., "Efficient XeI Excimer Ultraviolet Sources from a Dielectric Barrier Discharge," J. Appl. Phys., vol. 84, pp. 1174-1178, 1998.

